Recurrent evacuation of mantle mush by mafic recharge in ocean island basalts, recorded by La Palma clinopyroxene

Alberto Caracciolo[1], Teresa Ubide[2], Mónica Ágreda-López[1], Raquel Herrera[3], Alvaro Marquez[4], Diego González-García[4], Maria Jose Huertas[4], Eumenio Ancochea[4], Nicolás Chicharro[4,5], Juan Jesús Coello-Bravo[6], Maurizio Petrelli[1]

[1] University of Perugia, Department of Physics and Geology, Perugia, Italy

[2]The University of Queensland, School of the Environment, Brisbane, Australia.

[3]Universidad Rey Juan Carlos, ESCET, Área de Geología, Tecvolrisk Research Group; Móstoles, Madrid, Spain.

[4]Universidad Complutense, Área de Petrología y Geoquímica, Madrid, Spain.

[5]Instituto Geográfico Nacional. Centro Geofísico de Canarias, Santa Cruz de Tenerife, Tenerife, Spain

[6]Fundación Telesforo Bravo - Juan Coello; Puerto de la Cruz, Tenerife, Spain.

Corresponding author: Alberto Caracciolo, (alberto@hi.is)

Abstract

Temporal variations in magma plumbing architecture and magmatic processes can modulate eruption priming, with direct consequences for interpreting pre- and syn-eruptive signals. However, how such processes unfold in low-flux volcanoes remains poorly constrained, leaving a gap in our understanding of eruption precursors. Here we examine the temporal evolution of magmatic processes at La Palma, Canary Islands, a low-flux ocean-island basaltic system, by interrogating the clinopyroxene zoning record from three historical eruptions during which lava composition transitioned from tephritic to basanitic: El Charco 1712, Teneguía 1971, and Tajogaite 2021. By combining major and trace element data from clinopyroxene crystals and carrier melts with textural observations, thermobarometry, quantitative trace element mapping, and cluster analysis, we reconstruct the magmatic processes and storage conditions preceding these eruptions. Both tephritic and basanitic magmas were stored in the upper mantle (18–25 km depth) together with an evolved tephritic to phonolitic crystal mush preserved in clinopyroxene antecryst cores. The phonolitic mush was stored at lower temperatures and likely originated by >80% fractionation of a basanitic melt. Repeated injections of basanite recharge melts gradually eroded and remobilized this mush, after which the recharge magma underwent ~10-20% fractional crystallization, producing a tephritic melt. Despite its pivotal role in priming the system, mafic recharge did not act as the immediate trigger for the La Palma historical eruptions. Early-erupted tephrite-hosted clinopyroxenes lack clear recharge-related signatures in their inner rims, suggesting that eruption onset was more likely linked to internal evolution of the reservoir.

1. Introduction

The dynamics of magma plumbing systems regulate not only the timing, composition, and style of volcanic eruptions, but also key subsurface processes such as magma recharge, mixing, and crystal mobilization (e.g. Caricchi et al., 2021; Ubide et al., 2021). Temporal changes in the configuration and behaviour of magma feeding and storage systems can influence eruption priming and the run-up to volcanic activity, with implications for interpreting monitoring signals and improving forecasts. Variations in volcanic plumbing systems over time have recently been explored in high-flux basaltic systems where eruptions are relatively frequent (e.g., Iceland and Hawaii; Caracciolo et al., 2025, 2023; Gao et al., 2022; Pietruszka et al., 2018). Such variations, however, remain largely underexplored in low-flux basaltic systems where the low eruption periodicity and varied eruption location translate into monitoring challenges and increased risk potential.

Magmatic processes occurring within a magma plumbing cannot be directly observed, yet they can be inferred from the chemical zoning and textural features of erupted minerals. This is because growing magmatic crystals can record the thermodynamic and chemical conditions of the magma from which they crystallize, preserving detailed archives of magma evolution and dynamics in their zoning patterns (e.g. Ubide et al., 2021; Ubide and Kamber, 2018). In particular, clinopyroxene crystals are outstanding recorders of magmatic processes, as they crystallize over a wide range of depths (e.g. Putirka, 2008) and preserve trace element zoning due to slow diffusion rates (e.g. Ubide and Kamber, 2018). La Palma, the most volcanically active island of the Canary Islands in historical time (eight eruptions since the 15th century), is a great candidate for studying the temporal evolution of magma plumbing characteristics at relatively low-flux ocean island basalt (OIB) systems via clinopyroxene records, as (1) the eruptive products contain abundant clinopyroxene crystals (2) there is a detailed record of historical eruptions (e.g. Hernandez-Pacheco and Valls, 1984; Longpré and Felpeto, 2021), (3) recent eruptions have shown petrological variations reflecting remobilization of mushes of basanite to phonolite compositions (Barker et al., 2015; Chamberlain et al., 2025; Day et al., 2022; Jegal et al., 2025; Klügel et al., 2022, 2017; Ubide et al., 2023) and (4) recent magmatic reactivation led to the 2021 Tajogaite eruption with major economic and societal consequences (e.g. Fourgassie et al., 2025). A study focusing on the temporal evolution of the magma plumbing system feeding historical magma plumbing at La Palma is urgent and lacking to date. Specifically, magma storage is considered to take place dominantly at upper mantle depths (Chamberlain et al., 2025; Dayton et al., 2023; González-García et al., 2023; Jegal et al., 2025; Klügel et al., 2022; Ubide et al., 2023) but the relevance of shallow crustal storage and the links between erupted lithologies and storage depths, essential for monitoring efforts, remains unclear.

In this work, we interrogate the zoning records preserved in clinopyroxene crystals from three historical eruptions at La Palma: El Charco 1712, Teneguía 1971 and Tajogaite 2021 (Fig. 1). All three eruptions erupted early tephrite followed by later basanite lavas (e.g. Chicharro, 2024; Ibarrola, 1974; Ubide et al., 2023) and some lavas hold evidence of phonolitic mush at depth, despite not erupted (Jegal et al., 2025; Klügel et al., 2000). Specifically, we integrate new major and trace element data across clinopyroxene textures with quantitative trace element mapping, pressure–temperature constraints, and cluster analysis. We combine the mineral dataset with major and trace element geochemistry of the associated carrier melts. By merging these new results with previous work on the 2021 Tajogaite eruption and earlier historical eruptions, we find a striking consistency in the magma chemistry and plumbing system anatomy during historical time, highlighting the key role of mafic recharge in priming plumbing systems at low-flux OIB volcanoes.

2. Methods

2.1 Sampling and electron microprobe (EMPA)

Samples from the 1712 El Charco, 1971 Teneguía and 2021 Tajogaite eruptions consist of fresh lavas that transition from tephrites to basanites throughout the eruption (Fig. 1 and Supplementary Material). Samples from Tajogaite 2021 correspond to the same sample set published in Ubide et al. (2023) (Supplementary Data Table 1, SDT1).

Clinopyroxene crystals were analysed using three different electron microprobe analysers (EMPA) (SDT2). In all EMPA instruments, measurements were conducted using a beam current of 10-20 nA, an accelerating voltage of 15 kV and a beam diameter of 5 μm or focused beam (see Supplementary Material for detailed information of each EMPA). To assess data consistency across instruments, we re-analyzed a selection of clinopyroxene crystals using the JEOL JXA iHP200F electron microprobe at the Centro Nacional de Microscopía Electrónica (Madrid). Repeat analyses (n=68) were conducted at the same locations as the original analyses and confirmed reproducibility across instruments within analytical uncertainty (Fig. S1-S2). Data quality was monitored by analysing standards from the Smithsonian Institution of Washington. Accuracy and precision were better than 1-6% and 1-3%, respectively (SDT3).

2.2 Laser Ablation-Inductively Coupled Plasma Mass Spectrometry (LA-ICP-MS)

LA-ICP-MS was used to determine trace element compositions of clinopyroxene crystals via single-spot analyses (following Petrelli et al. 2016), to acquire quantitative trace element maps of clinopyroxene (following Ágreda-López et al. 2025) and to measure major and trace element compositions of the microcrystalline matrix (following Ubide et al. 2023). LA-ICP-MS analyses were done at the Dipartimento di Fisica e Geologia, University of Perugia, using a 193 nm Analyte G2 laser ablation system coupled to a quadrupole iCAP-Q ICP-MS (Thermo Fisher Scientific). Overall, accuracy is better than 10% (typically within 5%) for trace elements and within 5% for major elements; precision for most major and trace elements is within 3-5% (SDT4, SDT5, SDT6, SDT7 and SDT8). Detailed information on LA-ICP-MS methods can be found in the Supplementary Material.

2.3 Clustering

Clustering is an unsupervised machine-learning technique used to partition complex, high-dimensional datasets into groups ("clusters") based on similarity in their multivariate features (e.g. Ágreda-López et al., 2025; Costa et al., 2023; Musu et al., 2023). This approach can identify similar chemical features by grouping together data that exhibit comparable elemental compositions. This can reveal patterns in large geochemical datasets that may correspond to distinct crystal zones, growth stages, or textural domains, without prior labels, and then facilitating the subsequent petrologic interpretation (Petrelli, 2024). Here, we applied clustering to the trace element clinopyroxene dataset (Sc, Ti, V, Cr, Mn, Ni, Sr, and Zr) from the three studied eruptions, which included both single-spot analyses (n=318) and quantified pixels from compositional maps (n=398776), using the k-means algorithm implemented in Python 3.

2.4 Thermobarometry

Magma storage pressures were estimated using clinopyroxene-melt barometers following guidelines for clinopyroxene-melt equilibrium and selection of calibrations provided by MacDonald et al. (2023). We applied thermobarometers calibrated on isothermal–isobaric datasets (Putirka, 2008; Putirka et al., 2003; SEE_P = ± 1.7 kbar, 5.6 km; SEE_T = ±45 °C), which perform best at low undercooling, to clinopyroxene cores and sector-zoned inner rims. In contrast, we used calibrations including decompression experiments (Mollo et al., 2018; SEE_P = ± 1.5 kbar, 4.9 km; SEE_T = ± 28 °C), more precise at high undercooling, for outer rims and microlites. For evolved core compositions (Mg# < 67), we used the thermobarometer of Masotta et al. (2013), calibrated for differentiated alkaline magmas (SEE_P = ± 1.15 kbar, ± 3.8 km; SEE_T = ± 18.2 ºC). An eruption-specific clinopyroxene–melt pairing was implemented in Thermobar (Wieser et al., 2022) using clinopyroxene and melt compositions from this study and from the literature (SDT9-SDT10) Further details on the selected thermobarometers, equilibrium criteria and comparison with other thermobarometers approaches (Fig. S4-S5) are provided in the Supplementary Material.

3 Results

3.1 Petrography and clinopyroxene textures

Lava samples in this study classify as tephrites and basanites based on petrographic observations. Both rock types are porphyritic and contain large crystals of clinopyroxene and Fe-Ti oxides. Tephrites are distinguished by the presence of amphibole (kaersutite), while basanites have olivine (Fig. 2).

Clinopyroxene crystals from the three eruptions range up to 5000 µm in size and are referred to with the general term crystals, while those smaller than 100 µm are termed microlites. Clinopyroxene can be found as standalone crystals surrounded by the groundmass or as mineral inclusion in rare plagioclase crystals (e.g. Jegal et al., 2025). Across all eruptions, clinopyroxene can host inclusions of apatite, Fe-Ti oxides, and glassy to microcrystalline melt inclusions (Fig. 2). The groundmass is microcrystalline and predominantly composed of plagioclase, clinopyroxene, and Fe–Ti oxides, as well as olivine in the basanites and amphibole in the tephrites

(Fig. 2). Clinopyroxene crystals can be broadly divided into three main textural zones across the three eruptions: core, inner rim, and outer rim. The cores represent the innermost parts of the crystals and are texturally complex, characterized by patchy or sector zoning in back-scattered electron (BSE) images (Fig. 2G-I). Under the petrographic microscope, clinopyroxene cores are green or light brown in plane polarised light, surrounded by brown rims that are often sector zoned. In BSE, the inner rims appear as darker zones than the cores, suggesting an increase in Mg (reverse zoning; Fig. 2G-I). The outermost zone, in contact with the groundmass, is the outer rim, usually forming a relatively thin (5-30 μm) layer that returns lighter BSE contrast (Fig. 2G-I).

3.2 Clinopyroxene major elements

Clinopyroxene crystals from all eruptions are diopside in composition and do not display geochemical differences in terms of En $[Mg / (Ca + Mg + Fe) \times 100]_{mol}$, Fs $[Fe / (Ca + Mg + Fe) \times 100]_{mol}$, Wo $[Ca / (Ca + Mg + Fe) \times 100]_{mol}$ components (Fig. S6) and Mg# values ([Mg / (Mg + Fe)] × 100, molar basis), which range from 52 to 86 (El Charco 1712, Mg#52-84, n=213; Teneguía 1971, Mg#56-86, n=164; Tajogaite 2021, Mg#56-86, n=786). However, there are consistent Mg# variations from cores to inner and outer rims. Cores show the broadest range of Mg# values within each eruption (El Charco 1712, Mg#52-83; Teneguía 1971, Mg#60-84; Tajogaite 2021, Mg#56-86), with compositions Mg#<67 consistent with green cores. Inner rims consistently have higher Mg# values defining reverse zoning (El Charco 1712, Mg#74-84; Teneguía 1971, Mg#74-83; Tajogaite 2021, Mg#69-84) and outer rims have lower Mg# 68–78 across the eruptions. Microlites span a range that overlaps both inner and outer rims, encompassing the full range defined by these two textural zones (El Charco 1712, Mg#70-80; Teneguía 1971, Mg#69-80; Tajogaite 2021, Mg#69-82) (Fig. 3 and S7).

Bivariate plots of Mg# versus major and minor elements show that clinopyroxene inner rims, outer rims, and microlites generally align along a coherent negative trend in diagrams such as Mg# vs TiO_2, Al_2O_3, and Na_2O, or a subtle positive trend with CaO or Cr_2O_3 (Fig. 3 and S8). Inner rims define the primitive end of the trend, showing higher Mg#-Cr_2O_3 and lower TiO_2-Al_2O_3 contents compared to outer rims (Fig. 3 and S8). Microlites span the full compositional range defined by inner and outer rims. In contrast, clinopyroxene cores are scattered over a broad compositional range, including along the main trend but mostly outside of it (Fig. 3 and S8). Core compositions span from primitive, Mg#-rich and TiO_2-poor types, to more evolved, visually green, Mg#-poor and Na_2O-rich compositions, which in Tajogaite 2021 are occasionally found with samples containing rare large crystals of plagioclase (Jegal et al., 2025; Ubide et al., 2023).

Overall, clinopyroxene compositions do not systematically vary with host rock type. Crystals from both tephrites and basanites span the full compositional range, though the most evolved cores, with the lowest Mg#, occur mainly in basanites (Fig. S9).

3.3 Clinopyroxene trace elements

Compatible elements in clinopyroxene such as Cr, Sc, and Ni, exhibit high concentrations and broad variability at low Zr contents (<200 ppm), reflecting more primitive compositions. In contrast, high-Zr (>400 ppm), evolved compositions, are characterized by consistently low concentrations of these elements (Fig. 4A-C and S10). Within each eruption, Cr concentration in clinopyroxene inner rims and microlites increases from early-erupted tephrite-hosted to late-erupted basanite-hosted clinopyroxene (Fig. 4G-I).

Incompatible trace elements correlate positively with Zr, with data from all eruptions aligning along a common trend (Fig. 4D-F and S11-S12). At Zr ~400 ppm, some clinopyroxene compositions diverge from this main trend, especially for elements like Y and middle and heavy rare earth elements (MREE-HREE) like Sm, Nd, Eu, Gd, Dy (Fig. 4D-F and S11-S12). High-Zr compositions (>400 ppm) are mostly observed in evolved clinopyroxene cores, which are slightly enriched in HREE (Tm, Yb, Lu) compared to other core compositions (Fig. S15). Normalized clinopyroxene trace element are broadly similar across eruptions, without notable differences between tephrite and basanite samples (Fig. S13-S14). Clinopyroxene cores display both enriched and depleted compositions, while inner rims are generally more depleted than outer rims and microlites (Fig. S13). Overall, trace element patterns are parallel, with consistent trace element abundances across the eruptions (Fig. S13-S14).

Clinopyroxene trace-element maps reveal chemical complexities not visible in BSE images (Fig. 5 and Fig. S23). The cores often exhibit extreme heterogeneity with patchy domains, subgrains and/or sector zoning (Fig. 5). Core compositions span from primitive (high Cr, Ni, Sc; low Zr, Mn) to evolved (low Cr, Ni, Sc; high Zr, Mn), mirroring single-spot analyses. Contacts between cores and surrounding portions of the crystal are usually rounded, particularly around evolved cores (low Cr, Sc, Ni; high Zr, Mn). A key feature is the high Cr, Ni and Sc concentration of clinopyroxene inner rims, consistently present across all mapped clinopyroxene crystals, reaching up to 3500 ppm of Cr (Fig. 5 and S23) and increasing from tephrite to basanite as observed for individual eruptions (Fig. 4G-I). The inner rims are either in contact with the groundmass directly or, more frequently, are surrounded by thin outer rims characterized by a drop in Cr, Sc, and Ni and higher Zr, Ti, and Mn relative to inner rims (Fig. 5 and S23). Multiple high-Cr zones are observed in the zoning record of tephrite- and basanite-hosted clinopyroxenes from Teneguía 1971 and Tajogaite 2021, whereas in El Charco 1712 they are restricted only to single inner rims (Fig. S16).

3.4 Major and trace element composition of the matrix

The matrix from the Teneguía 1971 and El Charco 1712 eruptions ranges in composition from basanite to tephrite, overlapping matrix results from the Tajogaite 2021 eruption (Fig. S17)

(Ubide et al., 2023). The mean MgO content of the matrix is 4.9 ± 0.7 wt% and 4.8 ± 0.9 wt% in El Charco 1712 and Teneguía 1971, respectively, similar to the matrix from the 2021 Tajogaite eruption of 4.7 ± 0.7 wt% (Fig. 6A) (Ubide et al., 2023).

Tephrite matrices display slightly higher Zr and incompatible trace element concentrations than basanites, indicating a more evolved character (Fig. 6B-C). Basanite compositions from the Tajogaite 2021 and Teneguía 1971 eruptions are similar and define overlapping fields (Fig. 6B-C). In contrast, basanites from El Charco 1712 are more evolved, plotting close to the tephrite fields of the other eruptions. The El Charco 1712 tephrite matrix is the most evolved, reaching the highest Zr and incompatible element concentrations (Fig. 6B–C), consistent with its most enriched trace-element patterns (Fig. 6D-F).

3.5 Pressure and temperature of clinopyroxene crystallization

Primitive clinopyroxene cores exhibit the greatest pressure variability within individual eruptions, extending down to 9.4 kbar (32 km) (Fig. 7A-C). Most primitive core pressures, hereafter defined as within the 10th–90th percentile, range from 6.4–7.7 kbar (22.2–26.5 km) for El Charco 1712, 6.2–6.9 kbar (21.5–23.9 km) for Teneguía 1971, and 6.6–8.6 kbar (22.9–29.4 km) for Tajogaite 2021. Evolved cores (Mg# < 67) record lower pressures, mostly 4.3–6.1 kbar (15.3–21.2 km), than primitive cores, with no systematic differences across eruptions (Fig. 7A-C). Inner rims, outer rims, and microlites show broadly similar pressure distributions across all eruptions (Fig. 7A-C). Inner rim pressures cluster within 5.4–7.0 kbar (19.7–24.2 km), outer rims within 5.0–7.0 kbar (17.6–24.2 km), and microlites between 5.2–7 kbar (18.3–24.2 km). Overall, clinopyroxene barometry indicates upper mantle storage (below the local Moho at 10-14 km; D’Auria et al., 2022; Ranero et al., 1995). We do not observe pressure differences across eruptions and textures beyond calibration uncertainties, except for some primitive cores likely crystallizing deeper (>7 kbar) than other textural categories (Fig. 7A-C).

Regarding temperatures, primitive clinopyroxene cores (1107-1145 °C), inner rims (1129-1155 °C), outer rims (1114 – 1147 °C) and microlites (1118 – 1153 °C) exhibit comparable temperature ranges across eruptions. The evolved cores record the lowest temperatures (1001 – 1025 °C), with no significant differences across the three eruptions (Fig. 7D-F).

4. Discussion

4.1 Limited temporal variation of tephrite-basanite carrier melts

The microcrystalline matrix represents a crystal-free proxy for carrier melts, unlike whole-rock compositions, which are often influenced by recycled crystals (Ubide et al., 2023, 2022). Major element homogeneity over time (~5 wt% MgO, in agreement with the filtering of OIB melts to eruptible liquids; Ubide et al., 2022) is mirrored in the trace elements, as matrix compositions from all three eruptions define a single array in incompatible trace element space (Fig. 6). The only notable difference is the more evolved trace element character of tephrite melts from the El Charco 1712 eruption. REE patterns are parallel across all eruptions, indicating compositions controlled by fractional crystallization. Trace element modelling shows that within each eruption, the transition from basanite to tephrite requires only ~10-20% fractionation (Fig. 6B-D). However, the more evolved El Charco 1712 matrices require ~20-30% fractionation (Fig. 6B-D). This higher degree of fractionation does not appear to correlate with pre-eruption repose time, as only 35 years separated El Charco 1712 from the previous eruption (San Antonio 1677). This timescale is shorter than the 50-year break preceding Tajogaite 2021 and longer than the 22 years preceding Teneguía 1971. Instead, the more evolved character of El Charco 1712 carrier melts may reflect limited mafic recharge into the system, allowing greater crystal fractionation and melt differentiation. This is supported by the lack of evidence for multiple high-Cr recharge events in mapped clinopyroxenes from El Charco 1712, in contrast to the periodic high-Cr recharge signatures identified in clinopyroxenes from Teneguía 1971 and Tajogaite 2021 (Fig. S16).

4.2 Upper mantle magma storage

Based on our clinopyroxene-melt themobarometric calculations performed on new data and published compositions, clinopyroxene crystallization depths and temperatures appear consistent both within individual eruptions and across historical time, within uncertainties of the applied thermobarometers (Fig. 7). The only exceptions are a subset of primitive cores, which likely suggest deeper crystallization relative to other textural groups, and the evolved cores, which crystallised at lower temperatures. Regardless of the calibration used, clinopyroxene crystals consistently record crystallization within the upper mantle beneath La Palma (Fig. 7 and S4-S5), at depths of approximately 18–25 km, with some primitive cores likely crystallizing below 25 km. These depths are consistent with the location of seismicity recorded before and during the 2021 Tajogaite eruption at 20-25 km depth (D’Auria et al., 2022).

Our results align with previous barometry studies on the 2021 Tajogaite eruption. González-García et al. (2023) applied the thermobarometer of Mollo et al. (2018) to clinopyroxene cores and rims, reporting pressures (10th–90th percentile) within the range of 6.0–7.9 kbar (21–27 km depth). Similarly, pressures derived from amphibole crystals span 5.4–7.8 kbar (19–27 km), suggesting similar storage depths for both tephrite and basanite magmas (Chamberlain et al., 2025; González-García et al., 2023). Ubide et al. (2023) applied the Putirka et al. (2003) barometer to inner rims and microlites, obtaining pressures in the range of 2.8–6.9 kbar (10–24 km). Our Tajogaite 2021 inner rims and microlites (5.5–7.0 kbar; 19–24 km) fall within the lower part of that depth range. This difference may reflect different equilibrium criteria and thermobarometers, though results agree within uncertainties. Romero et al. (2022) report higher clinopyroxene crystallization pressures between 7.6 – 11.7 kbar (26-40 km), similar to those calculated by Castro and Feisel (2022), in the range 7-10 kbar (24-34 km) and to those obtained by Chamberlain et al. (2025), where mean pressures for clinopyroxene cores, rims and microlites are between 7.3-8.6 kbar (25-29 km). These studies used the calibration of Neave and Putirka (2017), which is not specifically designed for mafic alkaline magmas and is noted here to yield higher pressure estimates for Tajogaite 2021 compared to barometers calibrated for such compositions (Fig. S4). An upper mantle extraction depth is also corroborated by melt and fluid inclusion studies during the 2021 Tajogaite eruption, which point out magma storage depth between 15-30 km (Dayton et al., 2024, 2023). Similarly, microthermometry on fluid inclusions from Tajogaite 2021 indicates magma storage at depths of 22 to 27 km, in addition to a shallower zone at 4 to 16 km depth (Zanon et al., 2024). The existence of this shallow zone, likely containing early-erupted tephrite magma, is also supported by experimental studies (Andújar et al., 2025; Fabbrizio et al., 2023) and shallow seismicity at 10-12 km during the 2021 Tajogaite eruption (D'Auria et al., 2022; del Fresno et al., 2023). Interestingly, we do not observe evidence for this shallow zone in the petrological record, nor in the storage depths of tephrite magmas derived from amphibole-based barometry (González-García et al., 2023), nor in the depth of phonolite.like magmas derived from inclusions of clinopyroxene in plagioclase crystals (Jegal et al., 2025). This suggests that this shallow zone is somewhat cryptic and may represent a transient storage level rather than a mature reservoir, where early-erupted tephrite magmas temporarily stagnate with insufficient time for clinopyroxene to re-equilibrate (Klügel et al., 2005).

Our results also agree with findings from previous literature concerning other historical eruptions at La Palma. Previous studies on the Teneguía 1971 eruption applied the barometer of Putirka et al. (2003) to clinopyroxene crystals and reported storage depths of 20–45 km (Barker et al., 2015; Weis et al., 2015). These estimates are deeper than those obtained in our study, likely because they used whole-rock compositions instead of matrix or glass, which typically results in overestimated pressures and temperatures (e.g. Wieser et al., 2024). Additionally, we note that the clinopyroxene compositions for Teneguía 1971 reported by Barker et al. (2015) and Weis et al. (2015), acquired using the same EMPA instrument, show systematically lower CaO and slightly higher Na_2O contents compared to our data (Fig. S8). These differences may reflect a calibration issue affecting CaO and Na_2O measurements (Fig. S8), with lower CaO and higher Na_2O in those datasets potentially explaining the higher-pressure estimates. The 1949 San Juan eruption was also fed by magma reservoir located at 21- 27 km or deeper, according to clinopyroxene-melt barometry (Klügel et al., 2000). Fluid inclusions in olivine and clinopyroxene crystals from the 1949 San Juan eruption record entrapment pressures of 6.0-6.8 kbar (21-24 km) and 2-3.4 kbar (8-12 km) (Hansteen et al., 1998). Overall, published thermobarometry on historical eruptions is consistent with findings from the 2021 Tajogaite eruption and our work, revealing temporally consistent magma storage of eruption-feeding reservoirs under Cumbre Vieja.

4.3 Clinopyroxene records of magma history: Coupling clustering texture, chemistry, and thermobarometry

4.3.1 Evolved melts related to cold phonolitic mushes in the upper mantle: Clusters 0 and 1:

Clusters 0 and 1 are characterized by the highest Zr and Mn contents and the lowest Cr, Sc, and Ni concentrations (Fig. 8). Cluster 1 differs from Cluster 0 by slightly higher Cr, Sc, and Ni. Both clusters show the most enriched REE patterns (Fig. S18-S19). They occur exclusively in clinopyroxene cores and often form patchy domains (Fig. 9). When present in other textural positions, they are restricted to microlite cores, as shown by cluster-colored microlite maps (Fig. 9A–B), likely representing core remnants of larger crystals. The exclusive occurrence of Clusters 0 and 1 in mineral cores and their resorbed textures suggest crystallization at depth, from melts no longer present at the time of eruption. We interpret these clusters as representing evolved and fractionated melt compositions growing patchy cores with relatively low Mg# values (Fig. S7 and S20A), compositions in major- and trace element disequilibrium with the tephrite-basanite carrier melts (Fig. S7 and S21). Clusters 0 and 1 clinopyroxenes also define a separate evolutionary trend in the Mg – Na – Fe2+(+Mn) diagram (Larsen, 1976) compared to tephrite and basanite related compositions (see 4.3.3), suggesting a different origin (Fig. S22). We therefore infer that Clusters 0 and 1 represent clinopyroxene antecrysts that did not crystallize from carrier liquids but instead formed in evolved melt pockets within a crystal mush (Fig. 10).

To investigate the nature of these evolved melt pockets, we calculated the trace element composition of melts in equilibrium with clinopyroxene, using partition coefficients (Kd) derived from multiple parameterizations by Bédard (2014) (see Supplement). The reconstructed melt compositions define a trend broadly consistent with fractional crystallization, with Clusters 0 and 1 representing the most differentiated compositions (Fig. S21D-F). Despite uncertainties from using fixed Kd values, our fractional crystallization modelling, starting from a primitive basanite matrix composition from 2021, indicates that up to 80–90% crystallization is required to produce the most evolved reconstructed melt compositions represented by Clusters 0 and 1 (Fig. S21). This aligns with the ~80-85% crystallization estimated to generate phonolitic magmas from basanitic magmas beneath La Palma (Johansen et al., 2005; Turner et al., 2015) and OIB settings in general (Berthod et al., 2021). We also observe fractionation of Y, MREE, and, to a lesser extent, HREE at fixed Zr in Clusters 0 and 1, with these elements showing lower concentrations in reconstructed melt compositions relative to LREE (Fig. 22). This likely reflects increased partitioning of MREE and HREE into amphibole and clinopyroxene during fractionation of evolved alkali melts, depleting the residual melts in these elements (Ubide et al., 2014). Additionally, most of the REE patterns of clinopyroxene from Clusters 0 and 1 show an upward inflection of HREE (Tm, Yb, Lu) compared to light REE. This is a typical behaviour of high-Na clinopyroxene crystallizing from phonolite melts, where HREE preferentially partition into the M1 site, whereas other REE remain mostly distributed in the M2 site (e.g. Baudouin et al., 2020; Jegal et al., 2025). All together, these observations support the occurrence and recycling of a phonolite-like mush under La Palma, as also supported by other studies focused on plagioclase antecrysts (Jegal et al., 2025). The occurrence of grey phonolitic xenopumice fragments in the Tajogaite 2021 products (Day et al., 2022) and the presence of minor phonolitic outcrops across Cumbre Vieja (Klügel et al., 2022, 2017) further indicates that magma storage at multiple levels beneath La Palma commonly results in the formation of phonolites.

Understanding the depth of crystallization of phonolite-derived Clusters 0 and 1 clinopyroxene cores is challenging, as the exact composition of the melts from which crystallized is unknown. There is evidence that evolved tephriphonolite and phonolite rocks form within the lowermost crust under La Palma (Klügel et al., 2022). However, as also suggested by Klugel et al. (2022), formation of phonolites cannot be solely related to the lower crust. Our evolved clinopyroxene cores represented by Clusters 0 and 1 are surrounded by tephritic to basanitic inner rims (Fig. 9) formed at upper mantle depths and at 1129-1155 °C (see 5.2), in line with literature findings (González-García et al., 2023; Ubide et al., 2023). Considering that basanite-tephrite inner rims crystallized in the mantle during historical time, evolved clinopyroxene cores must also have formed in the mantle. Jegal et al. (2025) estimated pressures of 5.4 ± 0.8 kbar and temperatures of 1021 ± 6 °C for a green evolved clinopyroxene included in a plagioclase antecryst, by pairing them with a titanite-hosted tephriphonolitic melt inclusion. Building on this approach, we used a Monte Carlo simulation starting from that melt inclusion composition as putative liquid for our evolved clinopyroxene cargo, finding mean crystallization depths for evolved clinopyroxene from El Charco 1712, Teneguía 1971 and Tajogaite 2021 of 4.8 ± 0.8 kbar (17 ± 2.9 km), 5.1 ± 0.4 kbar (18 ± 1.5 km) and 5.0 ± 0.8 kbar (18 ± 2.9 km). Mean temperatures of evolved clinopyroxene for the same eruptions are 1021 ± 13 °C, 1018 ± 8 °C and 1019 ± 12 °C, respectively. Our results agree with Jegal et al. (2025), placing evolved clinopyroxene crystallization in a cold upper mantle storage region (Fig. 10), as also observed at other OIB volcanoes (Beloša et al., 2024).

4.3.2 Magma recharge and subsequent differentiation: Clusters 5 and 3

Cluster 5 displays the highest Cr, Ni, and Sc and lowest Zr and Mn concentrations (Fig. 8). It is the most depleted in REE and the least fractionated, with Mg#>67 (Fig. S18 and S20A). Cluster 3 is similar to Cluster 5 but is distinguished by lower Cr, Sc, and Ni concentrations (Fig. 8) and a slightly more fractionated character (Fig. S18). In general, Clusters 3 and 5 are found in primitive cores, inner rims, and microlites, all with Mg# >67 (Fig. S20A). Their major and trace element compositions are in chemical equilibrium with carrier melts, suggesting that they are true phenocrysts (Fig. S7 and S21). In basanite-hosted clinopyroxenes, Cluster 5 consistently characterizes the inner rims across all eruptions, typically forming a homogeneous euhedral zone (Fig. 9). In contrast, in tephrite-hosted clinopyroxenes, inner rims are characterized by the more fractionated Cluster 3, preceded by Cluster 5 compositions (Fig. 9). Importantly, the pattern that emerges from these observations is that inner rims are commonly associated to clusters 3 and 5, which define reverse zoning relative to cores.

The dominance of primitive inner rims suggests mafic magma recharge prior to eruptions, similar to other low-flux basaltic volcanoes (e.g., Etna; MacDonald et al., 2024; Ubide and Kamber, 2018). We interpret Cluster 5 as representing pre-eruptive basanite recharge that disrupts the resident crystal mush (Fig. 10). As for Cluster 3, its trace element composition suggests crystallization from a magma that underwent fractionation following mafic recharge, sufficient to deplete the melt in compatible elements. Cluster 3 therefore represents a slightly more fractionated flavour of Cluster 5, likely linked to the tephrite magma (Fig. 10). However, the significance of Cluster 3 is complex, as it occurs in different textural positions. When present in clinopyroxene cores, Cluster 3 either forms homogeneous cores (Teneguía 1971, Tajogaite 2021), or patchy domains (El Charco 1712) or is linked to Cluster 5 through sector zoning (Fig. 9B). The occurrence of Cluster 3 in mineral cores suggests that the remobilized mush was liked zoned, i.e., not composed exclusively of phonolitic antecrysts (Clusters 0 and 1), but also contained tephritic crystals (Cluster 3). Importantly, in tephrite-hosted clinopyroxene, Cluster 3 dominates inner rims, which consistently overgrows Cluster 5 compositions, suggesting fractionation following mafic recharge. In contrast, in basanite-hosted clinopyroxene, Cluster 3, when present, generally precedes the final mafic recharge event in the zoning record (Fig. 9). Although we lack temporal constraints for the El Charco 1712 samples, tephrite samples erupted earlier than the basanites (Chicharro, 2024), similar to the 1971 Teneguía (Ibarrola, 1974) and 2021 Tajogaite eruptions (e.g. Ubide et al. 2023). To explore the temporal variation of mafic recharge in the three eruptions, we examined Cr concentrations in inner rims and microlites (Fig. 4G-I). Cr concentrations are significantly lower in the early-erupted tephrite-hosted clinopyroxene inner rims and microlites compared to those in basanite-hosted clinopyroxene. This pattern is consistent with observations from the 2021 Tajogaite eruption, where there is evidence for a progressive and gradual increase in Cr concentration of recharge melts over the course of the eruption (Fig. 4I; Ubide et al., 2023), similar to recent basaltic eruptions where similar datasets are available (e.g., Mt Etna 2021 paroxysms; MacDonald et al., 2024). Cluster-coloured maps also show Cr-poor, Cluster 3 inner rims in tephrite-hosted clinopyroxene and Cr-rich, Cluster 5 inner rims in basanite-hosted clinopyroxene (Fig. 9). Hence, considering similarities with the 2021 Tajogaite eruption, we argue that also during El Charco 1712 and Teneguía 1971, there was a progressive input of a mafic magma that gradually evacuated and remobilized a tephritic to phonolitic crystal mush in the upper mantle (Fig. 10).

4.3.3 Cryptic primitive seed for the phonolite lineage?: Cluster 4

Cluster 4 is characterized by the lowest Ti, V and Al_2O_3 concentrations, coupled with relatively high Cr and Ni contents, although lower than those of Cluster 5 (Fig. 8 and S20). It is extremely rare, occurring as single-spot data in two cores from Teneguía 1971 and Tajogaite 2021. In mapped clinopyroxenes, it appears as a large, resorbed core in one crystal from Tajogaite 2021 and as patches within a Cluster 1 core in one crystal from El Charco 1712. Despite its sporadic occurrence and geochemical characteristics, Cluster 4 likely represents a melt composition that crystallized at depth, as it is confined to mineral cores. The lower Cr concentrations and the highly resorbed clinopyroxene core mapped in Tajogaite 2021 (Fig. 9C) suggest crystallization from a less mafic melt than the recharge magma, followed by partial dissolution during interaction with the recharging melt. The low Ti, V and Al_2O_3 contents of Cluster 4 suggest crystallization at low degrees of undercooling, possibly in a quiet magmatic environment, during which Al, Ti and V remain in the residual melt due to crystallization kinetics (MacDonald et al., 2022; Mollo et al., 2010).

The major element composition of Cluster 4 clinopyroxenes defines an evolutionary trend in the Mg–Na–Fe^{2+}(+Mn) diagram (Larsen, 1976) that highlights its transitional nature between basanite (Cluster 3 and 5) and phonolite (Cluster 0) (Fig. S22). Cluster 4 cores fall at the start of the phonolitic trend, suggesting it records a primitive composition, capable of evolving into phonolitic melts.

4.3.4 Magma ascent in the plumbing system: Cluster 2

Cluster 2 is marked by the highest Ti, V and Al_2O_3 concentrations, along with elevated Sc levels, while Cr remains similar to Cluster 1 (Fig. 8 and S20). Cluster 2 is predominantly found in outer rims, together with a minor proportion of Cluster 1 in El Charco 1712 and Teneguía 1971 samples. Microlites also show Cluster 2, but only in their outermost portions (Fig. 9). Therefore, Cluster 2 is related to the very final crystallization process following mafic recharge, and its increased uptake of Al-Ti is consistent with crystallisation at high degrees of undercooling during magma ascent (Mollo et al., 2010; Ubide and Kamber, 2018). The Cr-poor, Ti- and Al-rich character of Cluster 2, and its textural dominance in outer rims, are consistent with crystallization during magma ascent and surface crystallization upon lava emplacement (Fig. 10), as also suggested at Etna volcano (MacDonald et al., 2024; Ubide and Kamber, 2018).

4.4 Mafic recharge priming OIB through time

Our findings from historical eruptions at La Palma underscore two key aspects with broader implications for low-flux OIB volcanoes globally: (1) the temporal consistency of geochemical characteristics and magma storage depths across different eruptions, and (2) the pivotal role of mafic recharge in eroding and remobilizing crystal mushes.

Cluster analysis reveals six common geochemical groups preserved across all three eruptions, indicating a consistent evolution of magmatic processes over time. This is supported by dominant crystallization trends, formed during recharge, fractionation and ascent, which show remarkably uniform major and trace element systematics. Likewise, magma storage pressures and temperatures remain largely invariant across eruptions (Fig. 10) (Barker et al., 2015; Klügel et al., 2022). Overall, these findings align with observations from other low-flux OIB volcanoes, where magma accumulation and differentiation occur predominantly in the upper mantle (Barker et al., 2021; Beloša et al., 2024; Longpré et al., 2014, 2008), underscoring the central role of mantle-seated processes in modulating volcanic activity at OIB.

Regarding the role of mafic recharge, we acknowledge its importance in remobilizing deep-seated crystal mushes. Nonetheless, we find little evidence in the tephrite-hosted clinopyroxene cargo that mafic recharge, as represented by Cluster 5, acted as the immediate eruption-driving mechanism during eruptions studied in this work, as these crystals lack Cluster

5 signatures in their inner rims, raising questions about the immediate eruption triggering. Volcanic eruptions can be triggered by reservoir failure, which may result from magma pressure build-up (e.g., magma recharge, volatile exsolution) or external factors (e.g., earthquakes, loading or unloading) (Caricchi et al., 2021). For the La Palma eruptions studied here, the recharge magma in early-erupted tephrite-hosted clinopyroxenes is always confined to earlier growth zones (Fig. 9), likely reflecting earlier episodes of recharge that did not immediately trigger the eruptions. Hence, we suggest that these mafic recharge events preserved in the inner portions of the zoning record represent repeated injections of mafic magma in the time preceding the eruptions (Fig. 10A). These repeated mafic inputs played a key role in gradually unlocking and remobilizing the relatively cold, evolved tephritic to phonolitic mush. This is consistent with observations from the 2021 Tajogaite eruption, for which seismicity suggests magma recharge since 2017 (del Fresno et al., 2023; Torres-González et al., 2020), while phase equilibrium experiments and olivine zoning records indicate cooling of the tephrite magma prior to the 2021 Tajogaite eruption (Andújar et al., 2025; Chamberlain et al., 2025). Thus, while mafic recharge was not the immediate eruption trigger, it played a key role in gradually priming the system, by recycling the resident tephritic to phonolitic crystal mush. Reservoir failure was probably reached because volatile exsolution following magma differentiation led to overpressure (Caricchi et al., 2021; Ubide et al., 2022). Once the eruptions initiated, the tephrite magmas were drained first, which in turn activated the recharge basanite reservoir, supplying fresher mafic basanite magma that dominated the late-erupted products (Fig. 10B). These findings highlight that, in low-flux OIB settings such as La Palma, mafic recharge is a key process in priming the plumbing system, even if it is not the immediate eruption trigger. This slightly deviates from observations at other basaltic volcanoes worldwide, where mafic recharge is often identified as the immediate eruption-triggering mechanism (e.g. Beloša et al., 2024; MacDonald et al., 2024; Manrique et al., 2020; Petrone et al., 2022; Ubide and Kamber, 2018). From a monitoring perspective, this underscores the importance of recognizing geophysical and geochemical signals of deep recharge (e.g.,

seismicity, deformation, changes in gas flux) as potential indicators of an eruption priming. Such signals may reflect the progressive destabilization of crystal-rich reservoirs and could provide critical windows for hazard assessment and early warning in similar intraplate volcanic systems.

5. Conclusions

We have explored the temporal evolution of magmatic processes under La Palma by targeting the zoning record of clinopyroxene crystals from the 1712 El Charco, 1971 Teneguía and 2021 Tajogaite eruptions, together with their carrier melts. By combining textural, geochemical, barometric and clustering constraints, we propose that the magma dynamics and storage conditions beneath La Palma have remained broadly consistent through historical time. Tephrite-basanite magmas are predominantly stored in deep, likely vertically extended, upper mantle reservoirs between ~18–25 km depth, with primitive clinopyroxene cores possibly crystallizing deeper and evolved phonolite mushes crystallising in cooled reservoirs after >80% fractional crystallization of basanite melts (Fig. 10). Mafic basanite melts, preserved in Cr-rich clinopyroxene inner rims, repeatedly recharged the La Palma plumbing system, eroding and disaggregating resident tephritic to phonolitic mushes. Following recharge, the basanite magma undergoes ~10-20% fractional crystallization, producing eruptible tephritic magmas. Hence, mafic recharge is a vital mechanism to unlock and remobilize mush systems and therefore represents a key eruption primer. In terms of the immediate eruption trigger, La Palma historical eruptions suggest initiation by the internal evolution of the tephrite reservoir (e.g. volatile exsolution), as early-erupted clinopyroxene inner rims shows no clear evidence of mafic recharge, as represented by Cluster 5, immediately preceding the eruptions.

Figure Captions

Fig. 1 Geological map of La Palma and sample localities of studied eruptions. (A) simplified geological map of La Palma island, with inset showing the location of the island in the Canaries. The Cumbre Vieja edifice shows historical eruptions occurred since the 15th century. (B-D) Zoom of historical eruptions studied in this work and sample localities of (B) El Charco 1712, (C) Teneguía 1971 (D) Tajogaite 2021 eruptions. Sample location is indicated by coloured diamonds, distinguishing between amphibole-bearing tephrite and olivine-bearing basanite samples. The duration of each eruption is shown in the bottom right corner. Geological data are from the Cartográfica de Canarias (https://www.grafcan.es/).

Fig. 2. Petrographic features of tephrite and basanite samples from the three eruptions studied in this work in backscattered electron images (BSE). (A-C) Representative BSE images of tephrite samples, showing a mineral assemblage characterized by crystals of clinopyroxene and amphibole. (D-F) Representative BSE images of basanite samples, showing a mineral assemblage dominated by crystals of clinopyroxene and olivine. (G-I) BSE images of clinopyroxene crystals, highlighting mineral zoning and different textural positions studied in this work. cpx: clinopyroxene; ol: olivine; amp: amphibole; ox: oxide; ap: apatite.

Fig. 3. Major element compositions of clinopyroxene crystals showing variation in Mg# as a function of TiO_2 for samples from (A) El Charco 1712 (B) Teneguía 1971, and (C) Tajogaite 2021. Data are categorized by textural position: core, inner rim, outer rim, microlite, and clinopyroxene inclusions. Literature data for Teneguía 1971 from Barker et al. (2015) and Weis et al. (2015) are not grouped into textures and are plotted as faded filled grey circles. For Tajogaite 2021, literature

data are from González-García et al. (2023), shown with faded colours according to textural positions. Inner rim and microlite compositions from the 2021 Tajogaite eruption are from Ubide et al. (2023) and are here plotted using the same colour scheme as our dataset, as they were collected from the same crystals and complement our study. Error bars indicate 1σ uncertainties derived from EMPA counting statistics.

Fig. 4. Trace element characteristics of different clinopyroxene textural positions, showing the LA-ICP-MS concentration of (A–C) Cr and (D-F) Sm in the different eruptions. Symbols and colours represent different textural positions. (G-I) Temporal variation of Cr concentration in inner rim and microlite compositions measured using both EMPA and LA-ICP-MS. For El Charco 1712, samples are ordered from early-erupted tephrite to late-erupted basanite to provide temporal context. For Teneguía 1971 and Tajogaite 2021, samples are plotted according to eruption age. LA-ICP-MS error bars indicate the internal 2SE analytical uncertainty, whereas EMPA error bars reflect 1σ analytical uncertainty based on counting statistics.

Fig. 5. Trace element maps of representative basanite-hosted clinopyroxene crystals from each eruption, El Charco 1712, Teneguía 1971, and Tajogaite 2021, showing the spatial distribution of Cr (A–C), Sc (D–F), and Zr (G–I) concentrations. Maps are visualized using a logarithmic scale and scaled to the maximum common range of Cr (0.1–6000 ppm; $\log_{10}$ = -1–3.3), Sc (20–140 ppm; $\log_{10}$ = 1.3–2.15) and Zr (80–700 ppm; $\log_{10}$ = 1.9–2.85) observed across the three maps to allow direct comparison of variations among samples and eruptions. Colour bars specify the element and the corresponding concentration range in ppm for each sample.

Fig. 6. Major and trace element composition of the microcrystalline matrix. (A) Variation of MgO vs Al_2O_3. (B) Variation of Zr vs La and (C) Zr vs Yb concentrations. Our data are compared to recent whole-rock (WR) major and trace element data from the literature published after 2000 for El Charco 1712 (Carracedo et al., 2001; Turner et al., 2015), Teneguía 1971 (Barker et al., 2015; Carracedo et al., 2001; Turner et al., 2015; Weis et al., 2015) and Tajogaite 2021 (Day et al., 2022; Pankhurst et al., 2022; Ubide et al., 2023). The black line in B and C shows a fractional crystallization model at 10% increments, starting from a primitive matrix composition (white star). See Supplementary Material for modelling details. (D-F) REE patterns of matrix composition, normalized to the composition of primitive mantle (Palme and O'Neill, 2014). Symbols are color-coded according to tephrite and basanite samples. For major elements, error bars represent 2σ accuracy estimated from BHVO-2G replicate analyses; for trace elements, error bars denote the internal 2SE analytical uncertainty.

Fig. 7. (A-C) Barometry and (D-F) thermometry results for the different eruptions illustrated as box plots. Data are grouped in boxplots and color-coded according to individual textural positions. The box represents the interquartile range (25th to 75th percentile), the horizontal line indicates the median, and the whiskers extend to the most extreme data points within 1.5 times the interquartile range from the lower and upper quartiles. Individual estimates are shown as circles, with error bars representing the standard deviation of the estimate at the 1σ level. The number of estimates that pass the equilibrium criteria (see Supplementary Materials) is indicated for each textural category. Calculations include clinopyroxene and melt compositions from this study and from the literature (Day et al., 2022; González-García et al., 2023; Jegal et al., 2025; Klügel et al., 2005; Longpré et al., 2025; Pankhurst et al., 2022; Ubide et al., 2023). Gray fields in A-C panels indicate the location of seismicity during the 2021 Tajogaite eruption (D'Auria et al., 2022). White rectangles indicate literature pressure ranges based on cpx (P_{Cpx}), amphibole (P_{Amp}) and fluid

inclusions (P_{FI}). Pressures were converted into depths using a crustal density of 2800 kg/m^3 and 3100 kg/m^3 above and below the Moho, respectively (Ranero et al., 1995; Tenzer et al., 2013).

Fig. 8. Boxplots showing the clustering results for Cr, Sc, Zr, Mn, Ni, Sr, V and Ti. The boxes represent the interquartile range (25th–75th percentile), the horizontal line indicates the median, and the whiskers extend to the most extreme data points within 1.5 times the interquartile range from the lower and upper quartiles. For clustering, we merged pixel-level concentrations (in ppm) from the chemical maps with single-spot data and considered data between 0.1st and 99.9th percentiles to avoid outliers. We tested 2 to 10 cluster grouping and selected six, as this configuration best captured the main textural and chemical features without unnecessary complexity (Fig. S3).

Fig. 9. Summary and visualization of the clustering results for A) El Charco 1712, B) Teneguía 1971, and C) Tajogaite 2021. Each panel includes: (1) cluster-coloured maps of clinopyroxenes, indicating whether they are hosted in tephrite or basanite samples and, where applicable, the eruption date. The black bar in each map indicates a scale bar of 100 µm; (2) stacked bar displaying, for each textural position, the proportions of the different clusters.

Fig. 10. Conceptual cartoon summarizing the main findings of this study. (A) Schematic illustration of the magmatic plumbing system beneath La Palma prior to El Charco 1712, Teneguía 1971 and Tajogaite 2021 eruptions. Basanite melts periodically recharge a tephritic to phonolitic (Cluster 0 and 1) crystal mush reservoir in the upper mantle, leading to partial remobilization and disaggregation of the resident antecrystic mush. Fractionation of the basanite melt following recharge produces eruptible tephrite magma. This recharge–disaggregation–fractionation process creates specific zoning patterns reflected in the early-erupted clinopyroxene record, characterized by tephritic inner rims (Cluster 3) preceded by

basanite compositions (Cluster 5) (B) Eruptions are likely triggered by internal evolution of the tephrite reservoir following fractionation of the basanite magma. Once the tephrite magma is exhausted, more primitive basanite magma is drained, carrying a crystal cargo dominated by clinopyroxene crystals with basanite recharge (Cluster 5) inner rims and antecrystic cores. During ascent and/or surface cooling, outer rims (Cluster 2) crystallize. Evidence for lower crustal stalling, as proposed by geophysical (D'Auria et al., 2022), melt and fluid inclusions (Hansteen et al., 1998; Zanon et al., 2024) and experimental studies (Andújar et al., 2025; Fabbrizio et al., 2023), is not recorded in our petrological record, implying it may represent a transient storage level.

Acknowledgements

AC, MP and MAL acknowledge the cascading fund titled "Exploring uncharted realms of volcanic eruptions using experimental petrology and ground deformation data – VOLC-LAPSE", within the Project "Multi-Risk sciEnce for resilienT commUnities undeR a changiNg climate (RETURN)", Project Code PE00000005, CUP H93C22000610002, funded by the European Union – NextGenerationEU under the National Recovery and Resilience Plan (NRRP), Mission 4 "Education and Research" – Component 2 "From Research to Business" – Investment 1.3 "Extended partnerships among universities, research centres, and companies for the funding of basic research projects. TU acknowledges support from the Australian Research Council (Future Fellowship FT230100230). RH, AM, DGG, MJH, EAS thanks the Spanish Science Ministry Project PID2022-141259NB-I00. Field work was funded by the Universidad Complutense (Acción Especial AENC1/21-29277) and the Universidad Rey Juan Carlos Research Groups Grant (to Tecvolrisk Research Group). We thank colleagues and volunteers who helped with field campaigns during and after the 2021 Tajogaite eruption, as well as the historical rock collection archive from the Universidad Complutense de Madrid hosting the samples from the 1971

Teneguía and 1712 El Charco eruptions. We thank analytical support from Alfredo Larios and Maider Virumbrales (UCM, Madrid) at Centro Nacional de Microscopía Electrónica at Universidad Complutense de Madrid.

Supplementary Materials

Supplementary material text and figures associated with this article can be found in the online version.

Data Availability

All data included in this article are included in Supplementary Data Tables (SDTs) in the online version of the article. Additionally, data are available in the repository Zenodo at the link: https://doi.org/10.5281/zenodo.17635257. Samples from the 2021 Tajogaite, 1971 Teneguía and 1712 El Charco eruptions are curated at Litoteca de Petrologia at UCM and are available for sharing and collaborations upon request to Dr. A. Márquez

References

Ágreda-López, M., Musu, A., Jorgenson, C., Šala, M., Giordano, G., Caricchi, L., Stremtan, C., Petrelli, M., 2025. The crystal cargo provides a chronicle of pre-caldera dynamics in mafic volcanic systems: insights from Colli Albani. Bull Volcanol 87. https://doi.org/10.1007/s00445-025-01865-6

Andújar, J., Scaillet, B., Frascerra, D., Di Carlo, I., Casillas, R., Suárez, E.D., Domínguez-Cerdeña, I., Meletlidis, S., López, C., Slodczyk, A., Martí, J., Núñez-Guerrero, E., 2025. Evolution of the crustal reservoir feeding La Palma 2021 eruption. Insights from phase equilibrium experiments and petrologically derived time scales. Journal of

Volcanology and Geothermal Research 463. https://doi.org/10.1016/j.jvolgeores.2025.108327

Barker, A.K., Rydeblad, E.M., Silva, S.M.D.M., 2021. Magma Storage at Ocean Islands: Insights From Cape Verde, in: Crustal Magmatic System Evolution: Anatomy, Architecture, and Physico-Chemical Processes. wiley, pp. 45–78. https://doi.org/10.1002/9781119564485.ch3

Barker, A.K., Troll, V.R., Carracedo, J.C., Nicholls, P.A., 2015. The magma plumbing system for the 1971 Teneguía eruption on La Palma, Canary Islands. Contributions to Mineralogy and Petrology 170, 1–21. https://doi.org/10.1007/s00410-015-1207-7

Baudouin, C., France, L., Boulanger, M., Dalou, C., Devidal, J.L., 2020. Trace element partitioning between clinopyroxene and alkaline magmas: parametrization and role of M1 site on HREE enrichment in clinopyroxenes. Contributions to Mineralogy and Petrology 175. https://doi.org/10.1007/s00410-020-01680-6

Bédard, J.H., 2014. Parameterizations of calcic clinopyroxene - Melt trace element partition coefficients. Geochemistry, Geophysics, Geosystems 15, 303–336. https://doi.org/10.1002/2013GC005112

Beloša, L., Murphy, D.T., Ubide, T., Callegaro, S., Meyzen, C.M., Bizimis, M., Mazzini, A., 2024. Magmatic evolution and architecture of an oceanic intraplate volcano: Vesteris Seamount, Atlantic Ocean. Front Earth Sci (Lausanne) 12. https://doi.org/10.3389/feart.2024.1501694

Berthod, C., Médard, E., Di Muro, A., Hassen Ali, T., Gurioli, L., Chauvel, C., Komorowski, J.C., Bachèlery, P., Peltier, A., Benbakkar, M., Devidal, J.L., Besson, P., Le Friant, A., Deplus, C., Nowak, S., Thinon, I., Burckel, P., Hidalgo, S., Feuillet, N., Jorry, S., Fouquet, Y., 2021. Mantle xenolith-bearing phonolites and basanites feed the active volcanic ridge of Mayotte (Comoros archipelago, SW Indian Ocean). Contributions to Mineralogy and Petrology 176. https://doi.org/10.1007/s00410-021-01833-1

Caracciolo, A., Bali, E., Halldórsson, S.A., Guðfinnsson, G.H., Kahl, M., Þórðardóttir, I., Pálmadóttir, G.L., Silvestri, V., 2023. Magma plumbing systems and timescale of magmatic processes during historical magmatism on Reykjanes Peninsula. Earth Planet Sci Lett 621, 118378. https://doi.org/10.1016/j.epsl.2023.118378

Caracciolo, A., Marshall, E.W., Mutch, E.J.F., Bali, E., Halldórsson, S.A., Matthews, S., Sigmarsson, O., Maclennan, J., Merrill, H., Gisladóttir, B.Ý., Johnson, S., Kahl, M., Guðfinnsson, G.H., Robin, J.G., Rúnarsdóttir, R.H., 2025. Mush disaggregation and dike propagation timescales at active volcanoes – Evidence from the 2022-2023 Fagradalsfjall eruptions. Journal of Petrology. https://doi.org/10.1093/petrology/egaf054

Caricchi, L., Townsend, M., Rivalta, E., Namiki, A., 2021. The build-up and triggers of volcanic eruptions. Nat Rev Earth Environ 2, 458–476. https://doi.org/10.1038/s43017-021-00174-8

Carracedo, J.C., Badiola, E.R., Guillou3, H., De La Nuez, J., Torrados, F.J.P., 2001. Geology and volcanology of La Palma and El Hierro, Western Canaries, Estudios GeoJ.

Castro, J.M., Feisel, Y., 2022. Eruption of ultralow-viscosity basanite magma at Cumbre Vieja, La Palma, Canary Islands. Nat Commun 13. https://doi.org/10.1038/s41467-022-30905-4

Chamberlain, K.J., Pankhurst, M., Neave, D., Morgan, D., Barbee, O., Scarrow, J., Hickey, J., Broom-Fendley, S., Gardner, J., Rollinson, G., Walshaw, R., Stewart, A., Wieser, P., Coldwell, B., Martín-Lorenzo, A., Rodríguez, F., 2025. Crystal cargo perspectives on magma assembly and dynamics during the 2021 Tajogaite eruption, La Palma, Canary Islands. Volcanica 8, 399–425. https://doi.org/10.30909/vol/vujv5852

Chicharro, N., 2024. La erupción de El Charco de 1712, La Palma. Características petrológicas e implicaciones en la peligrosidad volcánica. Universidad Complutense de Madrid. https://doi.org/https://docta.ucm.es/entities/publication/b8280

Costa, S., Caricchi, L., Pistolesi, M., Gioncada, A., Masotta, M., Bonadonna, C., Rosi, M., 2023. A data driven approach to mineral chemistry unveils magmatic processes associated with long-lasting, low-intensity volcanic activity. Sci Rep 13, 1–15. https://doi.org/10.1038/s41598-023-28370-0

D'Auria, L., Koulakov, I., Prudencio, J., Cabrera-Pérez, I., Ibáñez, J.M., Barrancos, J., García-Hernández, R., Martínez van Dorth, D., Padilla, G.D., Przeor, M., Ortega, V., Hernández, P., Peréz, N.M., 2022. Rapid magma ascent beneath La Palma revealed by seismic tomography. Sci Rep 12. https://doi.org/10.1038/s41598-022-21818-9

Day, James M D, Troll, V.R., Aulinas, M., Deegan, F.M., Geiger, H., Carlos, J., Gisbert, G., Perez-torrado, F.J., 2022. Mantle source characteristics and magmatic processes during the 2021 La Palma eruption. Earth Planet Sci Lett 597, 117793. https://doi.org/10.1016/j.epsl.2022.117793

Day, James M. D., Troll, V.R., Aulinas, M., Deegan, F.M., Geiger, H., Carracedo, J.C., Pinto, G.G., Pérez-Torrado, F.J., 2022. Mantle source characteristics and magmatic processes during the 2021 La Palma eruption. Earth Planet Sci Lett 597. https://doi.org/10.1016/j.epsl.2022.117793

Dayton, K., Gazel, E., Wieser, P., Troll, V.R., Carracedo, J.C., Madrid, H. La, Roman, D.C., Ward, J., Aulinas, M., Geiger, H., Deegan, F.M., Gisbert, G., Pérez-Torrado, F.J., 2023. Deep magma storage during the 2021 La Palma eruption. Sci Adv 9, 1–8. https://doi.org/10.1126/sciadv.ade7641

Dayton, K., Gazel, E., Wieser, P.E., Troll, V.R., Carracedo, J.C., Aulinas, M., Perez-Torrado, F.J., 2024. Magmatic Storage and Volatile Fluxes of the 2021 La Palma Eruption. Geochemistry, Geophysics, Geosystems 25. https://doi.org/10.1029/2024GC011491

del Fresno, C., Cesca, S., Klügel, A., Domínguez Cerdeña, I., Díaz-Suárez, E.A., Dahm, T., García-Cañada, L., Meletlidis, S., Milkereit, C., Valenzuela-Malebrán, C., López-Díaz, R., López, C., 2023. Magmatic plumbing and dynamic evolution of the 2021 La Palma eruption. Nat Commun 14. https://doi.org/10.1038/s41467-023-35953-y

Fabbrizio, A., Bamber, E.C., Michailidou, E., Romero, J.E., Arzilli, F., Bonechi, B., Polacci, M., Burton, M., 2023. Phase equilibrium experiments and thermodynamic simulations to constrain the pre-eruptive conditions of the 2021 Tajogaite eruption (Cumbre Vieja volcano, La Palma, Canary Islands). Journal of Volcanology and Geothermal Research 442. https://doi.org/10.1016/j.jvolgeores.2023.107901

Fourgassie, L., Rodríguez-Pérez, M.C., Fuentes Ferrer, M.E., Zwirner, E., Borbon, A., Colomb, A., Perez Torrado, F.J., Jessop, D., Moune, S., Paris, R., Sauzéat, L., Tomašek, I., Damby, D., Dezecache, G., Eychenne, J., 2025. Post-traumatic stress disorder in adult population of La Palma (Spain) after the 2021 Tajogaite eruption: Environmental and sociodemographic predictors. International Journal of Disaster Risk Reduction 127. https://doi.org/10.1016/j.ijdrr.2025.105680

Gao, R., Lassiter, J.C., Clague, D.A., Bohrson, W.A., 2022. Evolution of Hawaiian Volcano Magmatic Plumbing System and Implications for Melt/Edifice and Melt/Lithosphere Interaction: Constraints from Huallai Xenoliths. Journal of Petrology 63. https://doi.org/10.1093/petrology/egac091

González-García, D., Boulesteix, T., Klügel, A., Holtz, F., 2023. Bubble-enhanced basanite–tephrite mixing in the early stages of the Cumbre Vieja 2021 eruption, La Palma, Canary Islands. Sci Rep 13. https://doi.org/10.1038/s41598-023-41595-3

Hansteen, T.H., Kluè, A., Schmincke, H.-U., 1998. Multi-stage magma ascent beneath the Canary Islands: evidence from fluid inclusions.

Hernandez-Pacheco, A., Valls, M.C., 1984. The historic eruptions of La Palma Island (Canaries). Arquipélago. Série Ciências da Natureza 83–94.

Ibarrola, E., 1974. Temporal modification of the basaltic materials from the 1971 eruption of the Teneguía volcano (La Palma, Canary Islands). Estudios Geológicos 49–58.

Jegal, Y., Ubide, T., Huertas, M.J., Herrera, R., Márquez, Á., Ancochea, E., Coello-Bravo, J.J., 2025. Plagioclase antecrysts record syn-eruptive incorporation of evolved mush during the 2021 Tajogaite eruption (La Palma, Spain). Contributions to Mineralogy and Petrology 180. https://doi.org/10.1007/s00410-025-02241-5

Johansen, T.S., Hauff, F., Hoernle, K., Klügel, A., Kokfelt, T.F., 2005. Basanite to phonolite differentiation within 1550-1750 yr: U-Th-Ra isotopic evidence from the A.D. 1585 eruption on La Palma, Canary Islands. Geology 33, 897–900. https://doi.org/10.1130/G21663.1

Klügel, A., Albers, E., Hansteen, T.H., 2022. Mantle and Crustal Xenoliths in a Tephriphonolite From La Palma (Canary Islands): Implications for Phonolite Formation at Oceanic Island Volcanoes. Front Earth Sci (Lausanne) 10. https://doi.org/10.3389/feart.2022.761902

Klügel, A., Galipp, K., Hoernle, K., Hauff, F., Groom, S., 2017. Geochemical and volcanological evolution of la palma, Canary Islands. Journal of Petrology 58, 1227–1248. https://doi.org/10.1093/petrology/egx052

Klügel, A., Hansteen, T.H., Galipp, K., 2005. Magma storage and underplating beneath Cumbre Vieja volcano, La Palma (Canary Islands). Earth Planet Sci Lett 236, 211–226. https://doi.org/10.1016/j.epsl.2005.04.006

Klügel, A., Hoernle, K.A., Schmincke, H.U., White, J.D.L., 2000. The chemically zoned 1949 eruption on La Palma (Canary Islands): Petrologic evolution and magma supply dynamics of a rift zone eruption. J Geophys Res Solid Earth 105, 5997–6016. https://doi.org/10.1029/1999jb900334

Larsen, M.L., 1976. Clinopyroxenes and Coexisting Mafic Minerals from the Alkaline Dimaussaq Intrusion, South Greenland 17, 258–290.

Longpré, M.A., Felpeto, A., 2021. Historical volcanism in the Canary Islands; part 1: A review of precursory and eruptive activity, eruption parameter estimates, and implications for hazard assessment. Journal of Volcanology and Geothermal Research 419. https://doi.org/10.1016/j.jvolgeores.2021.107363

Longpré, M.A., Klügel, A., Diehl, A., Stix, J., 2014. Mixing in mantle magma reservoirs prior to and during the 2011-2012 eruption at El Hierro, Canary Islands. Geology 42, 315–318. https://doi.org/10.1130/G35165.1

Longpré, M.A., Tramontano, S., Pankhurst, M.J., Roman, D.C., Reiss, M.C., Cortese, F., James, M.R., Spina, L., Rodríguez, F., Coldwell, B., Martín-Lorenzo, A., Barbee, O., D'Auria, L., Chamberlain, K.J., Scarrow, J.H., 2025. Shifting melt composition linked to volcanic tremor at Cumbre Vieja volcano. Nat Geosci. https://doi.org/10.1038/s41561-024-01623-x

Longpré, M.A., Troll, V.R., Hansteen, T.H., 2008. Upper mantle magma storage and transport under a Canarian shield-volcano, Teno, Tenerife (Spain). J Geophys Res Solid Earth 113. https://doi.org/10.1029/2007JB005422

MacDonald, A., Ubide, T., Mollo, S., Masotta, M., Pontesilli, A., 2022. Trace element partitioning in zoned clinopyroxene as a proxy for undercooling: Experimental constraints from trachybasaltic magmas. Geochim Cosmochim Acta 336, 249–268. https://doi.org/10.1016/j.gca.2022.09.007

MacDonald, A., Ubide, T., Mollo, S., Pontesilli, A., Masotta, M., 2023. The Influence of Undercooling and Sector Zoning on Clinopyroxene-Melt Equilibrium and Thermobarometry. Journal of Petrology 64, 1–18. https://doi.org/10.1093/petrology/egad074

MacDonald, A., Ubide, T., Mollo, S., Taddeucci, J., 2024. Spatial and temporal mush heterogeneity during eruptions recorded in clinopyroxene from the 2021 paroxysms at Mt. Etna, Italy. Contributions to Mineralogy and Petrology 179. https://doi.org/10.1007/s00410-024-02174-5

Masotta, M., Mollo, S., Freda, C., Gaeta, M., Moore, G., 2013. Clinopyroxene-liquid thermometers and barometers specific to alkaline differentiated magmas. Contributions to Mineralogy and Petrology 166, 1545–1561. https://doi.org/10.1007/s00410-013-0927-9

Mollo, S., Blundy, J., Scarlato, P., De Cristofaro, S.P., Tecchiato, V., Di Stefano, F., Vetere, F., Holtz, F., Bachmann, O., 2018. An integrated P-T-H2O-lattice strain model to quantify the role of clinopyroxene fractionation on REE+Y and HFSE patterns of mafic alkaline magmas: Application to eruptions at Mt. Etna. Earth Sci Rev. https://doi.org/10.1016/j.earscirev.2018.05.014

Mollo, S., Del Gaudio, P., Ventura, G., Iezzi, G., Scarlato, P., 2010. Dependence of clinopyroxene composition on cooling rate in basaltic magmas: Implications for thermobarometry. Lithos 118, 302–312. https://doi.org/10.1016/j.lithos.2010.05.006

Musu, A., Corsaro, R.A., Higgins, O., Jorgenson, C., Petrelli, M., Caricchi, L., 2023. The magmatic evolution of South-East Crater (Mt. Etna) during the February–April 2021 sequence of lava fountains from a mineral chemistry perspective. Bull Volcanol 85. https://doi.org/10.1007/s00445-023-01643-2

Neave, D.A., Putirka, K.D., 2017. A new clinopyroxene-liquid barometer , and implications for magma storage pressures under Icelandic rift zones. American Mineralogist 102, 777–794. https://doi.org/http://dx.doi.org/10.2138/am-2017-5968

Palme, H., O'Neill, H., 2014. Cosmochemical Estimates of Mantle Composition, in: Treatise on Geochemistry: Second Edition. Elsevier Inc., pp. 1–39. https://doi.org/10.1016/B978-0-08-095975-7.00201-1

Pankhurst, M.J., Scarrow, J.H., Barbee, O.A., Hickey, J., Coldwell, B.C., Rollinson, G.K., Rodríguez-Losada, J.A., Martín-Lorenzo, A., Rodríguez, F., Hernández, W., Calvo Fernández, D., Hernández, P.A., Pérez, N.M., Sánchez, F., 2022. Rapid response petrology for the opening eruptive phase of the 2021 Cumbre Vieja eruption, La Palma, Canary Islands. Volcanica.

Petrelli, M., 2024. Machine Learning in Petrology: State-of-the-Art and Future Perspectives. Journal of Petrology 65. https://doi.org/10.1093/petrology/egae036

Petrelli, M., Morgavi, D., Vetere, F., Perugini, D., 2016. Elemental imaging and petro-volcanological applications of an improved Laser Ablation Inductively Coupled Quadrupole Plasma Mass Spectrometry. Periodico di Mineralogia. https://doi.org/10.2451/2015PM0465

Petrone, C.M., Mollo, S., Gertisser, R., Buret, Y., Scarlato, P., Del Bello, E., Andronico, D., Ellis, B., Pontesilli, A., De Astis, G., Giacomoni, P.P., Coltorti, M., Reagan, M., 2022. Magma recharge and mush rejuvenation drive paroxysmal activity at Stromboli volcano. Nat Commun 13. https://doi.org/10.1038/s41467-022-35405-z

Pietruszka, A.J., Marske, J.P., Heaton, D.E., Garcia, M.O., Rhodes, J.M., 2018. An isotopic perspective into the magmatic evolution and architecture of the rift zones of kilauea volcano. Journal of Petrology 59, 2311–2352. https://doi.org/10.1093/petrology/egy098

Putirka, K.D., 2008. Thermometers and barometers for volcanic systems. Rev Mineral Geochem 69, 61–120. https://doi.org/10.2138/rmg.2008.69.3

Putirka, K.D., Mikaelian, H., Ryerson, F., Shaw, H., 2003. New clinopyroxene-liquid thermobarometers for mafic, evolved, and volatile-bearing lava compositions, with applications to lavas from Tibet and the Snake River Plain, Idaho. American Minerologist 88, 1542–1554.

Ranero, C.R., Torné, M., Banda, E., 1995. Gravity and multichannel seismic reflection constraints on the lithospheric structure of the Canary Swell. Mar Geophys Res (Dordr) 17, 519–534.

Romero, J.E., Burton, M., Cáceres, F., Taddeucci, J., Civico, R., Ricci, T., Pankhurst, M.J., Hernández, P.A., Bonadonna, C., Llewellin, E.W., Pistolesi, M., Polacci, M., Solana, C., D'Auria, L., Arzilli, F., Andronico, D., Rodríguez, F., Asensio-Ramos, M., Martín-Lorenzo, A., Hayer, C., Scarlato, P., Perez, N.M., 2022. The initial phase of the 2021 Cumbre Vieja ridge eruption (Canary Islands): Products and dynamics controlling edifice growth and collapse. Journal of Volcanology and Geothermal Research 431. https://doi.org/10.1016/j.jvolgeores.2022.107642

Tenzer, R., Bagherbandi, M., Vajda, P., 2013. Global model of the upper mantle lateral density structure based on combining seismic and isostatic models. Geosciences Journal 17, 65–73. https://doi.org/10.1007/s12303-013-0009-z

Torres-González, P.A., Luengo-Oroz, N., Lamolda, H., D'Alessandro, W., Albert, H., Iribarren, I., Moure-García, D., Soler, V., 2020. Unrest signals after 46 years of quiescence at Cumbre Vieja, La Palma, Canary Islands. Journal of Volcanology and

Geothermal Research 392, 106757. https://doi.org/10.1016/J.JVOLGEORES.2019.106757

Turner, S., Hoernle, K., Hauff, F., Johansen, T.S., Klügel, A., Kokfelt, T., Lundstrom, C., 2015. 238 U–230 Th–226 Ra disequilibria constraints on the magmatic evolution of the Cumbre Vieja volcanics on La Palma, Canary Islands. Journal of Petrology 56, 1999–2024.

Ubide, T., Galé, C., Arranz, E., Lago, M., Larrea, P., 2014. Clinopyroxene and amphibole crystal populations in a lamprophyre sill from the Catalonian Coastal Ranges (NE Spain): A record of magma history and a window to mineral-melt partitioning. Lithos 184–187, 225–242. https://doi.org/10.1016/j.lithos.2013.10.029

Ubide, T., Kamber, B.S., 2018. Volcanic crystals as time capsules of eruption history. Nat Commun 9, 326. https://doi.org/10.1038/s41467-017-02274-w

Ubide, T., Larrea, P., Becerril, L., Galé, C., 2022. Volcanic plumbing filters on ocean-island basalt geochemistry. Geology 50, 26–31. https://doi.org/10.1130/G49224.1

Ubide, T., Márquez, Á., Ancochea, E., Huertas, M.J., Herrera, R., Jesús Coello-Bravo, J., Sanz-Mangas, D., Mulder, J., Macdonald, A., Galindo, I., 2023. Discrete magma injections drive the 2021 La Palma eruption. Sci Adv.

Ubide, T., Neave, D.A., Petrelli, M., Longpré, M.A., 2021. Crystal Archives of Magmatic Processes. Front Earth Sci (Lausanne) 9, 1–7. https://doi.org/10.3389/feart.2021.749100

Weis, F.A., Skogby, H., Troll, V.R., Deegan, F.M., Dahren, B., 2015. Magmatic water contents determined through clinopyroxene: Examples from the Western Canary Islands, Spain. Geochemistry, Geophysics, Geosystems 16, 2127–2146. https://doi.org/10.1002/2015GC005800

Wieser, P.E., Gleeson, M.L.M., Matthews, S., DeVitre, C., Gazel, E., 2024. Determining the pressure-temperature-composition (P-T-X) conditions of magma storage, 3rd ed, Reference Module in Earth Systems and Environmental Sciences. Elsevier Inc. https://doi.org/10.1016/b978-0-323-99762-1.00024-3

Wieser, P.E., Petrelli, M., Lubbers, J., Wieser, E., Özaydın, S., Kent, A.J.R., Till, C.B., 2022. Thermobar: An open-source Python3 tool for thermobarometry and hygrometry. Volcanica 5, 349–384. https://doi.org/10.30909/vol.05.02.349384

Zanon, V., Schiavi, F., Cyrzan, K., Pankhurst, M.J., 2024. Toward a near real-time magma ascent monitoring by combined fluid inclusion barometry and ongoing seismicity, Sci. Adv.

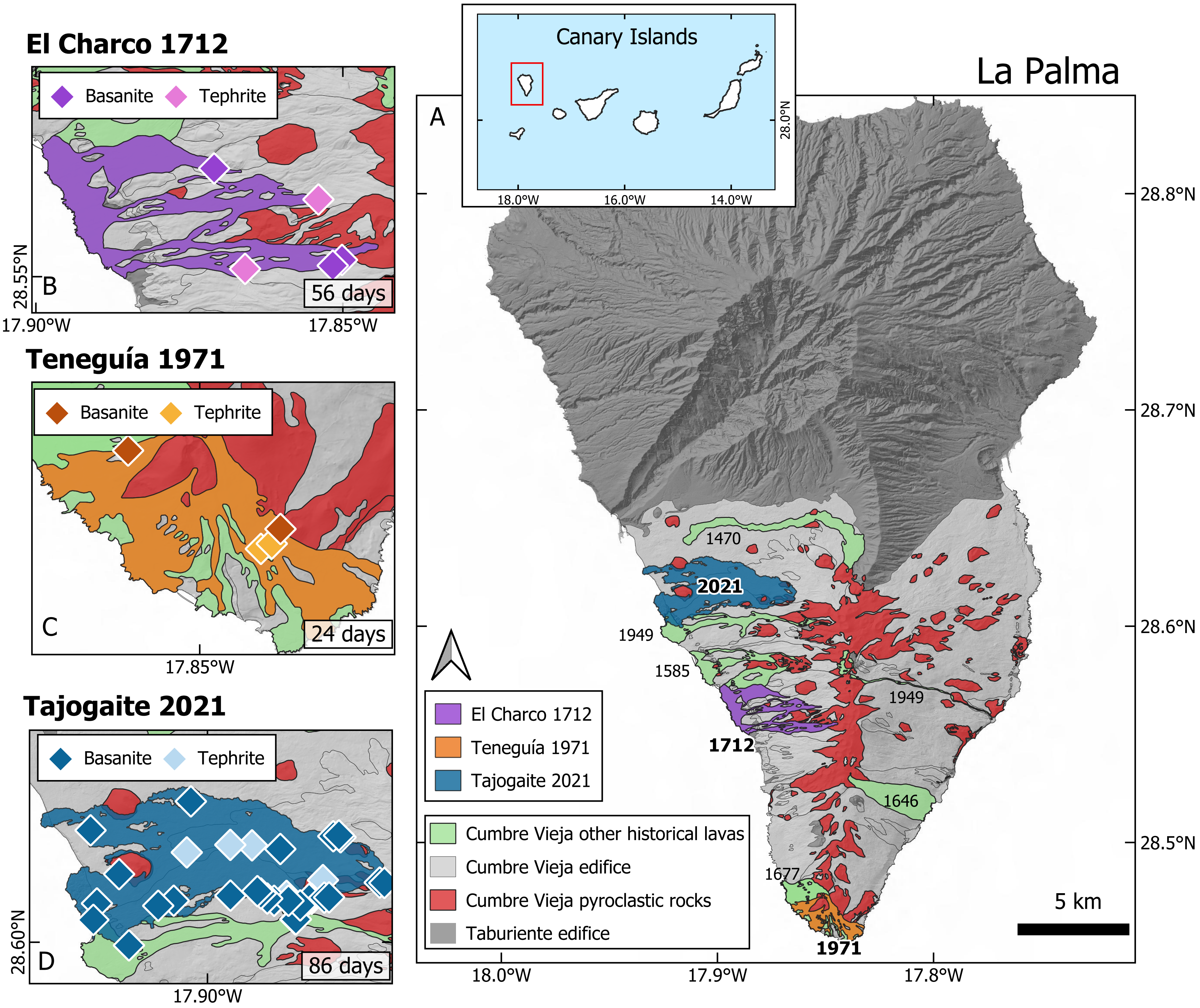
El Charco 1712
Basanite
Tephrite
B
56 days
28.55°N
17.90°W
17.85°W
Teneguía 1971
Basanite
Tephrite
C
24 days
17.85°W
Tajogaite 2021
Basanite
Tephrite
D
86 days
28.60°N
17.90°W
Canary Islands
18.0°W
16.0°W
14.0°W
28.0°N
La Palma
A
28.8°N
28.7°N
28.6°N
28.5°N
1470
2021
1949
1585
1949
1712
1646
1677
1971
El Charco 1712
Teneguía 1971
Tajogaite 2021
Cumbre Vieja other historical lavas
Cumbre Vieja edifice
Cumbre Vieja pyroclastic rocks
Taburiente edifice
5 km
18.0°W
17.9°W
17.8°W

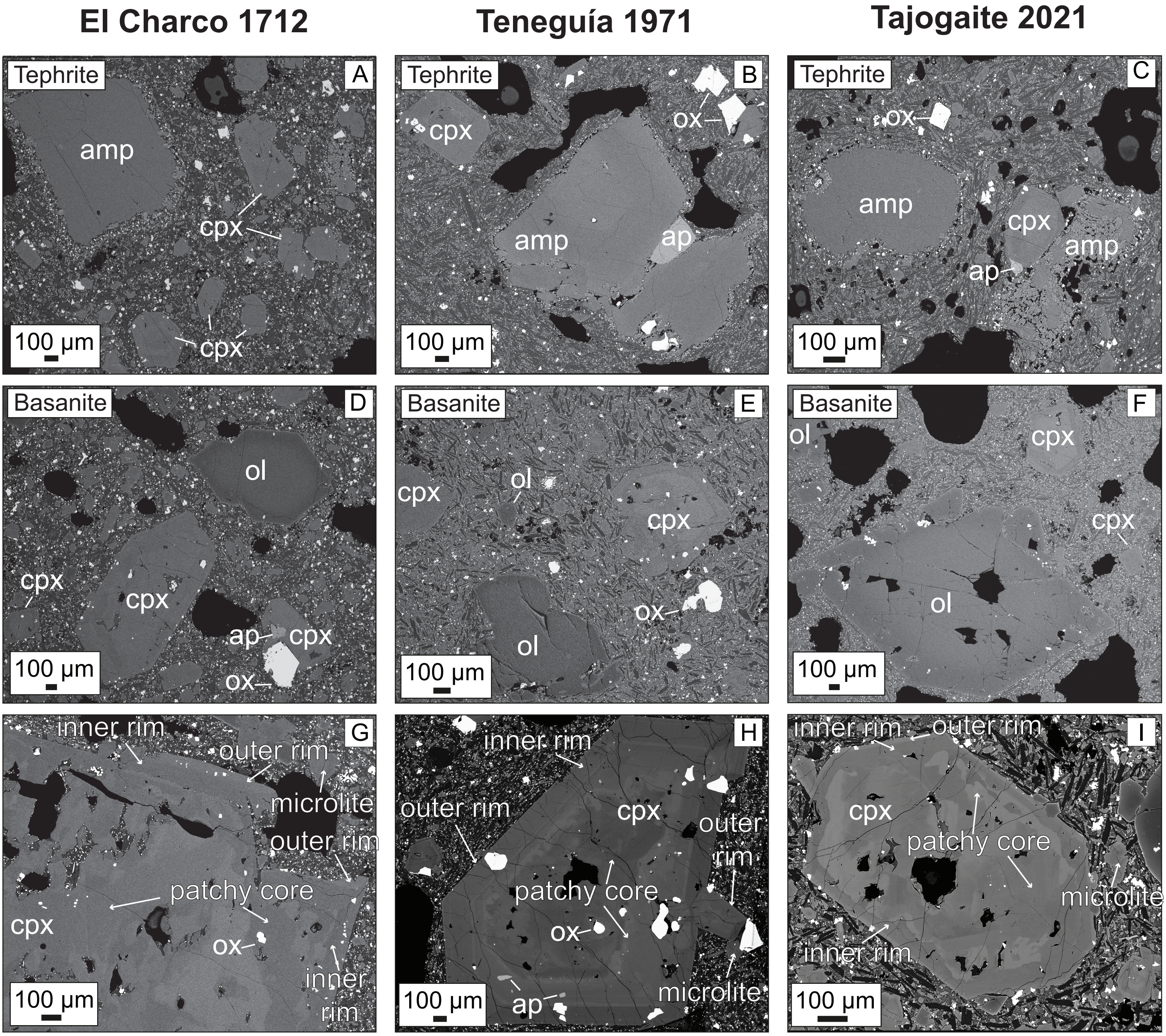
El Charco 1712
Teneguía 1971
Tajogaite 2021
Tephrite
A
amp
cpx
cpx
100 µm
Tephrite
B
cpx
ox
amp
ap
100 µm
Tephrite
C
ox
amp
cpx
amp
ap
100 µm
Basanite
D
ol
cpx
cpx
ap
cpx
ox
100 µm
Basanite
E
cpx
ol
cpx
ox
ol
100 µm
Basanite
F
ol
cpx
cpx
ol
100 µm
G
inner rim
outer rim
microlite
outer rim
patchy core
cpx
ox
inner rim
100 µm
H
inner rim
outer rim
cpx
outer rim
patchy core
ox
ap
microlite
100 µm
I
inner rim
outer rim
cpx
patchy core
microlite
inner rim
100 µm

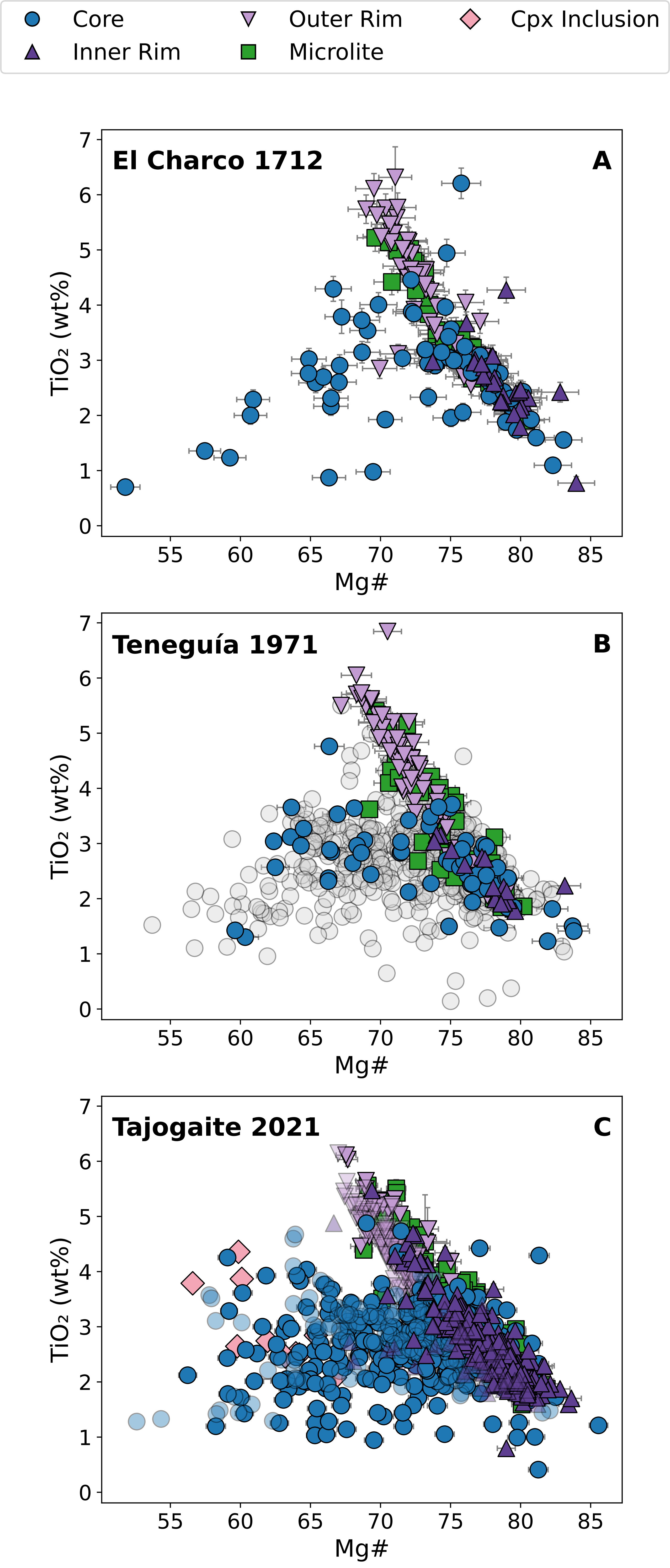
Core
Outer Rim
Cpx Inclusion
Inner Rim
Microlite
El Charco 1712
A
Teneguía 1971
B
Tajogaite 2021
C
TiO₂ (wt%)
Mg#
0
1
2
3
4
5
6
7
55
60
65
70
75
80
85

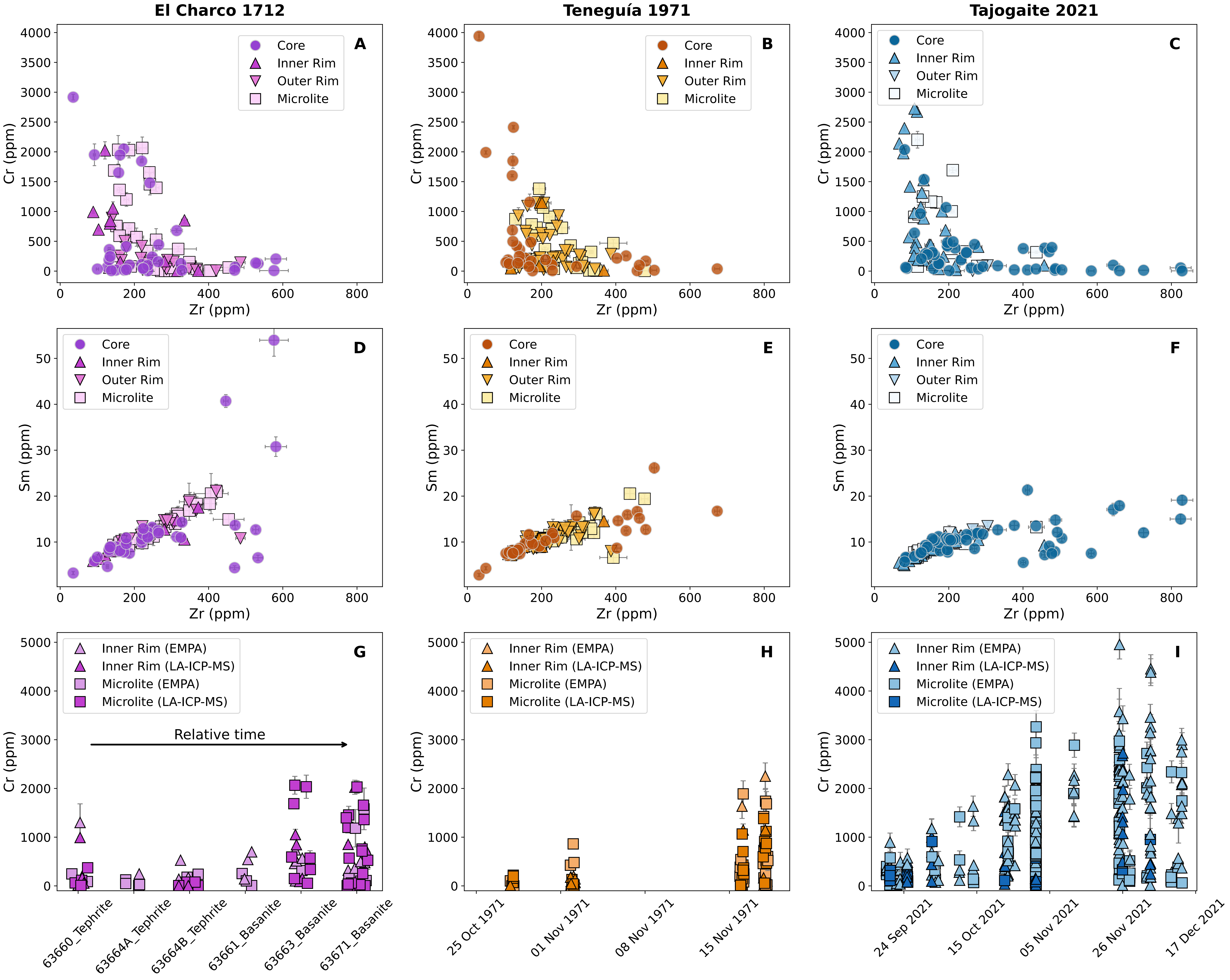
El Charco 1712
Teneguía 1971
Tajogaite 2021
A
B
C
D
E
F
G
H
I
Core
Inner Rim
Outer Rim
Microlite
Cr (ppm)
Sm (ppm)
Zr (ppm)
0
200
400
600
800
500
1000
1500
2000
2500
3000
3500
4000
10
20
30
40
50
Inner Rim (EMPA)
Inner Rim (LA-ICP-MS)
Microlite (EMPA)
Microlite (LA-ICP-MS)
Relative time
5000
63660_Tephrite
63664A_Tephrite
63664B_Tephrite
63661_Basanite
63663_Basanite
63671_Basanite
25 Oct 1971
01 Nov 1971
08 Nov 1971
15 Nov 1971
24 Sep 2021
15 Oct 2021
05 Nov 2021
26 Nov 2021
17 Dec 2021

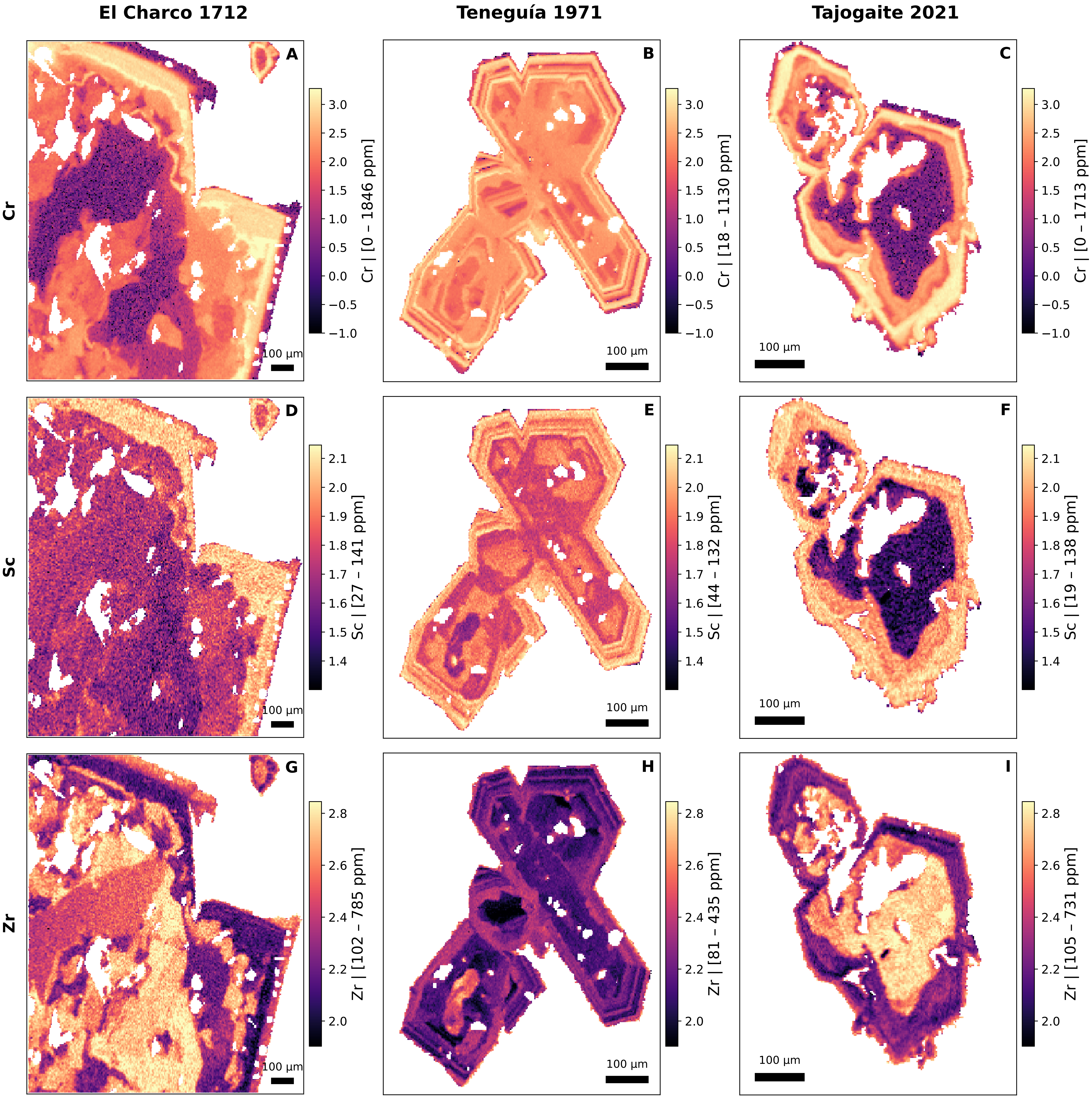
El Charco 1712
Teneguía 1971
Tajogaite 2021
Cr
Sc
Zr
A
B
C
D
E
F
G
H
I
Cr | [0 – 1846 ppm]
Cr | [18 – 1130 ppm]
Cr | [0 – 1713 ppm]
Sc | [27 – 141 ppm]
Sc | [44 – 132 ppm]
Sc | [19 – 138 ppm]
Zr | [102 – 785 ppm]
Zr | [81 – 435 ppm]
Zr | [105 – 731 ppm]
3.0
2.5
2.0
1.5
1.0
0.5
0.0
−0.5
−1.0
2.1
2.0
1.9
1.8
1.7
1.6
1.5
1.4
2.8
2.6
2.4
2.2
2.0
100 µm

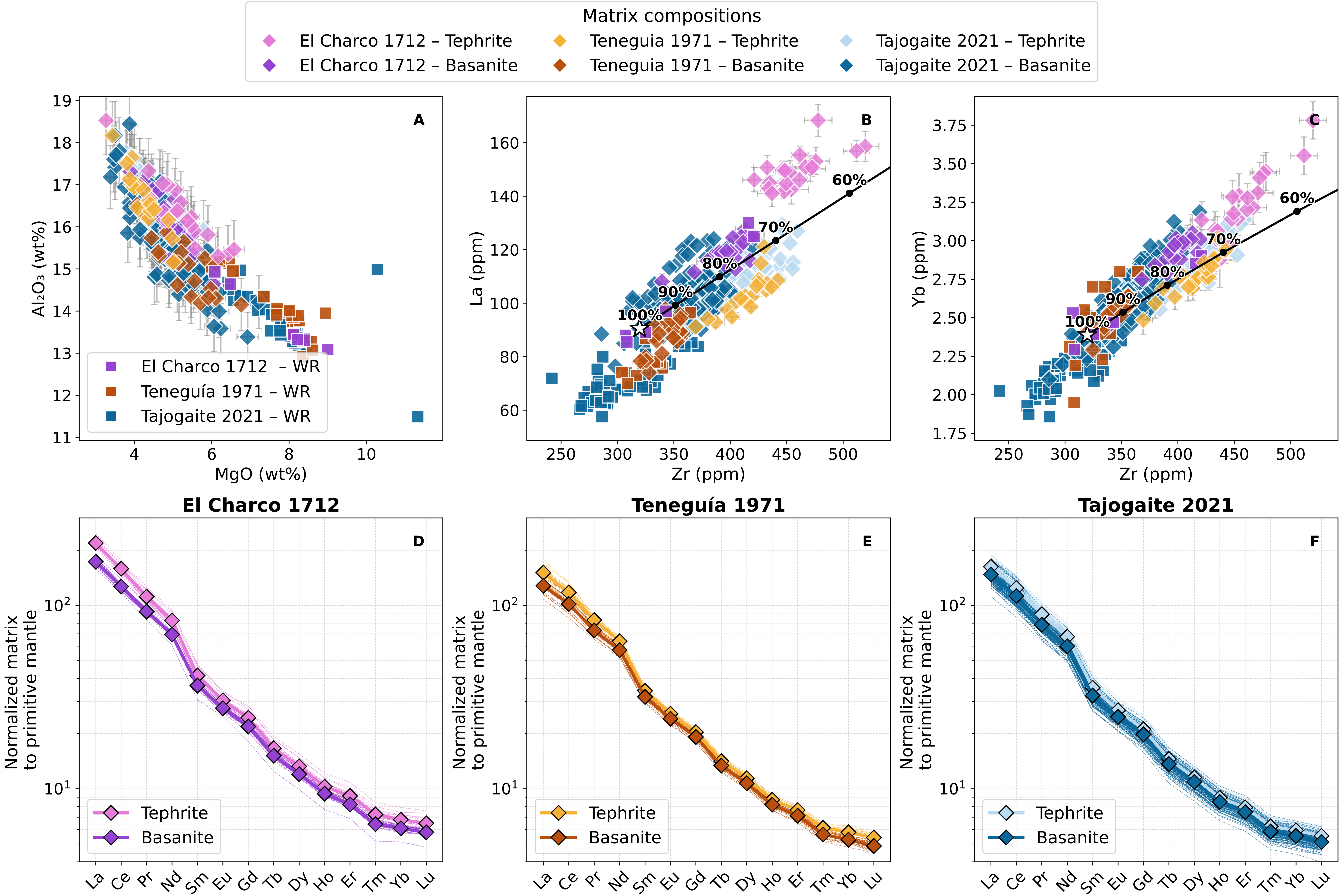
Matrix compositions
El Charco 1712 – Tephrite
El Charco 1712 – Basanite
Teneguia 1971 – Tephrite
Teneguia 1971 – Basanite
Tajogaite 2021 – Tephrite
Tajogaite 2021 – Basanite
A
Al₂O₃ (wt%)
MgO (wt%)
19
18
17
16
15
14
13
12
11
4
6
8
10
El Charco 1712 – WR
Teneguía 1971 – WR
Tajogaite 2021 – WR
B
La (ppm)
Zr (ppm)
160
140
120
100
80
60
250
300
350
400
450
500
100%
90%
80%
70%
60%
C
Yb (ppm)
Zr (ppm)
3.75
3.50
3.25
3.00
2.75
2.50
2.25
2.00
1.75
250
300
350
400
450
500
100%
90%
80%
70%
60%
El Charco 1712
D
Teneguía 1971
E
Tajogaite 2021
F
Normalized matrix to primitive mantle
10^2
10^1
Tephrite
Basanite
La
Ce
Pr
Nd
Sm
Eu
Gd
Tb
Dy
Ho
Er
Tm
Yb
Lu

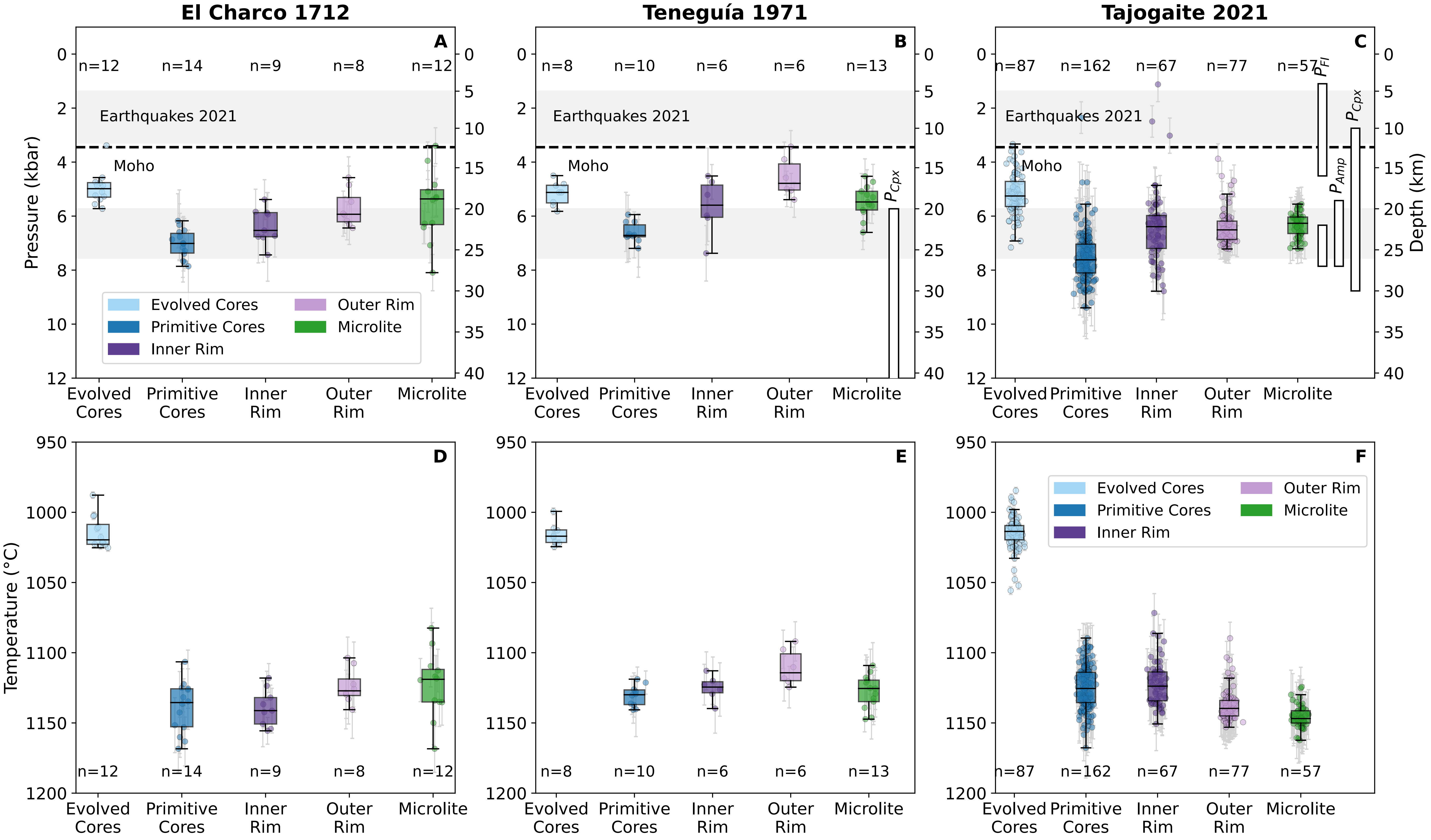
El Charco 1712
Teneguía 1971
Tajogaite 2021
A
B
C
D
E
F
Pressure (kbar)
Depth (km)
Temperature (°C)
Earthquakes 2021
Moho
P_{Cpx}
P_{Fl}
P_{Amp}
n=12
n=14
n=9
n=8
n=12
n=8
n=10
n=6
n=6
n=13
n=87
n=162
n=67
n=77
n=57
Evolved Cores
Primitive Cores
Inner Rim
Outer Rim
Microlite
0
2
4
6
8
10
12
0
5
10
15
20
25
30
35
40
950
1000
1050
1100
1150
1200

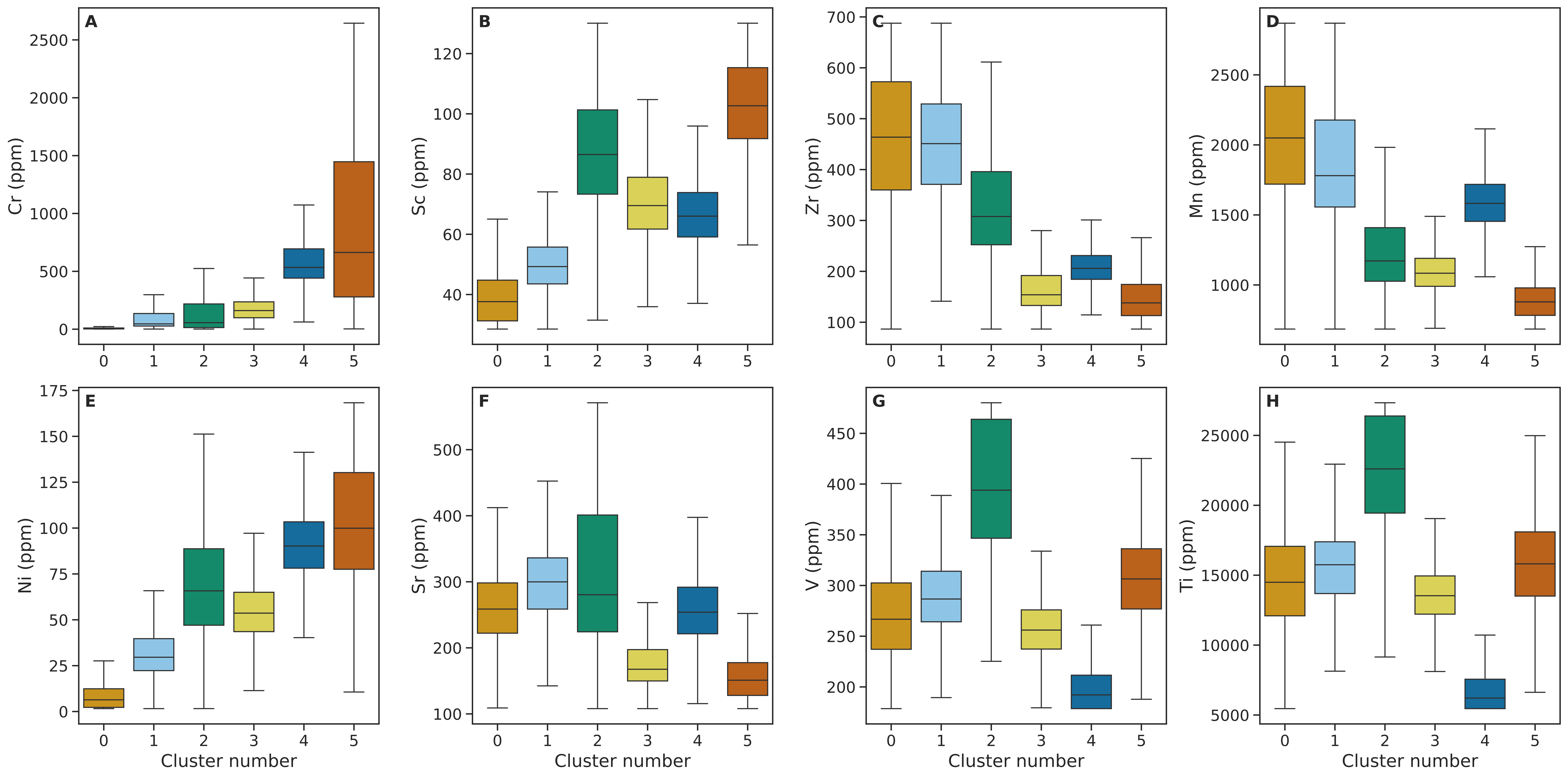
A
Cr (ppm)
0
500
1000
1500
2000
2500
B
Sc (ppm)
40
60
80
100
120
C
Zr (ppm)
100
200
300
400
500
600
700
D
Mn (ppm)
1000
1500
2000
2500
E
Ni (ppm)
0
25
50
75
100
125
150
175
F
Sr (ppm)
100
200
300
400
500
G
V (ppm)
200
250
300
350
400
450
H
Ti (ppm)
5000
10000
15000
20000
25000
0
1
2
3
4
5
Cluster number

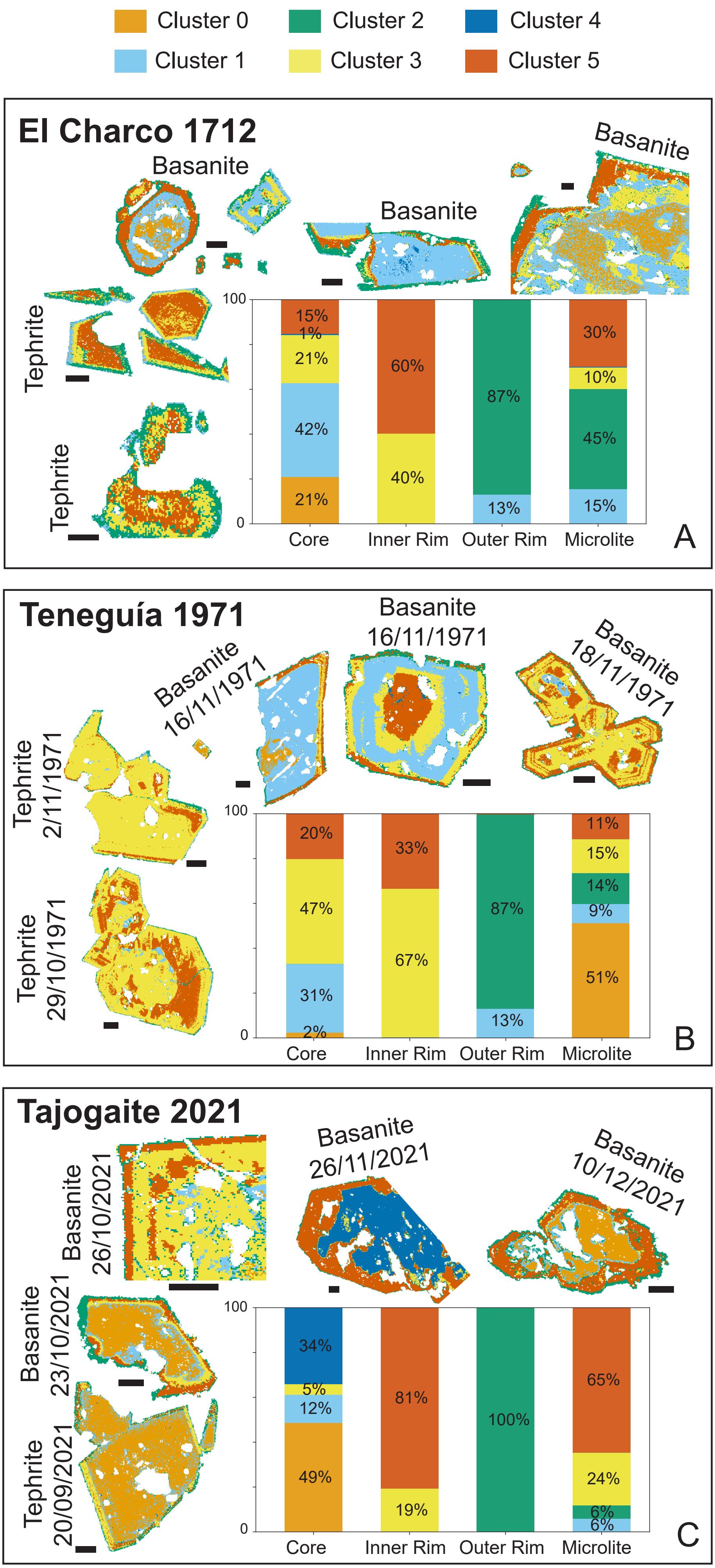
Cluster 0
Cluster 2
Cluster 4
Cluster 1
Cluster 3
Cluster 5
El Charco 1712
Basanite
Basanite
Basanite
Tephrite
Tephrite
100
0
15%
1%
21%
42%
21%
60%
40%
87%
13%
30%
10%
45%
15%
Core
Inner Rim
Outer Rim
Microlite
A
Teneguía 1971
Basanite 16/11/1971
Basanite 16/11/1971
Basanite 18/11/1971
Tephrite 2/11/1971
Tephrite 29/10/1971
100
0
20%
47%
31%
2%
33%
67%
87%
13%
11%
15%
14%
9%
51%
Core
Inner Rim
Outer Rim
Microlite
B
Tajogaite 2021
Basanite 26/10/2021
Basanite 26/11/2021
Basanite 10/12/2021
Basanite 23/10/2021
Tephrite 20/09/2021
100
0
34%
5%
12%
49%
81%
19%
100%
65%
24%
6%
6%
Core
Inner Rim
Outer Rim
Microlite
C

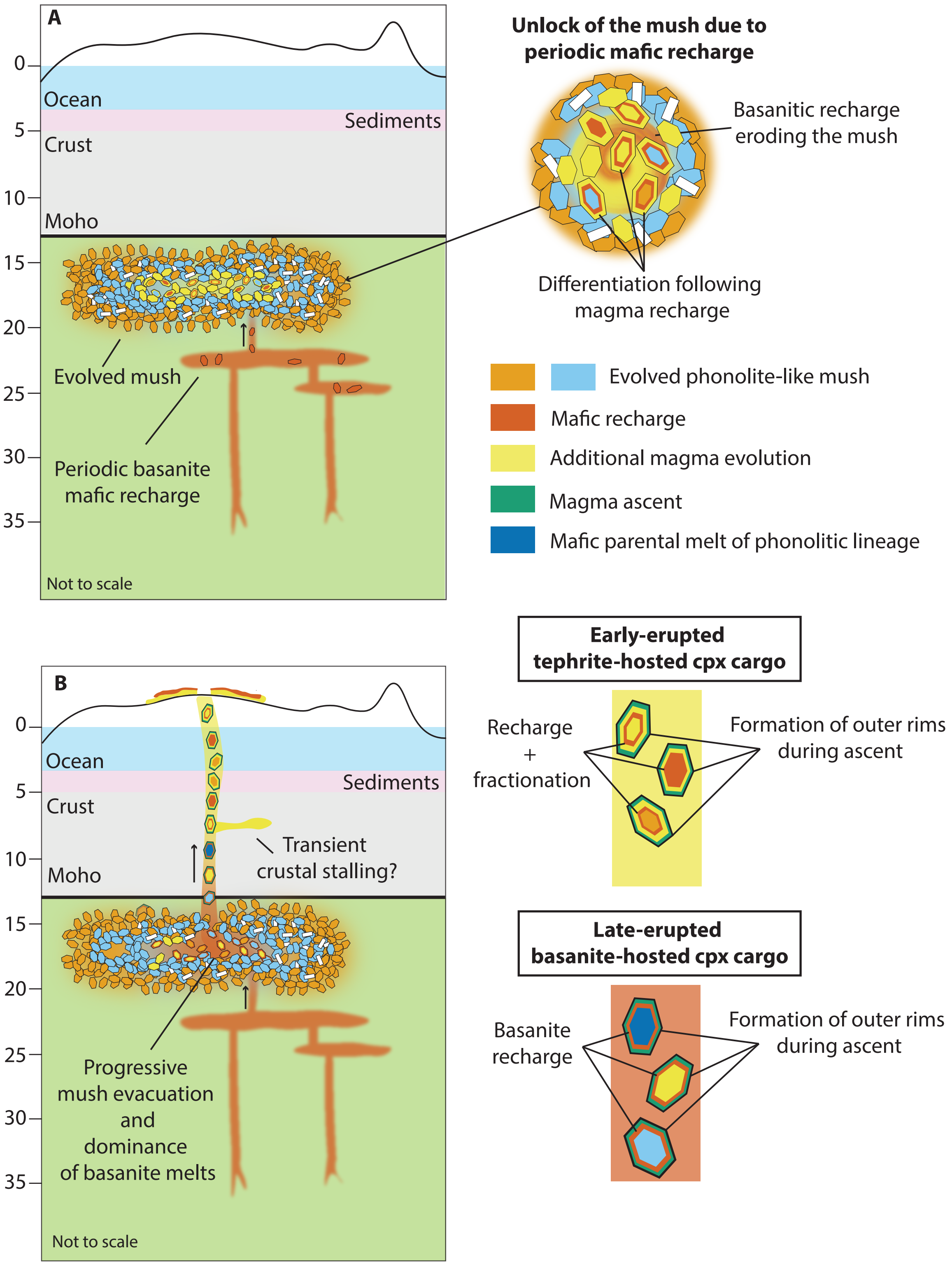
A
0
5
10
15
20
25
30
35
Ocean
Sediments
Crust
Moho
Evolved mush
Periodic basanite mafic recharge
Not to scale
Unlock of the mush due to periodic mafic recharge
Basanitic recharge eroding the mush
Differentiation following magma recharge
Evolved phonolite-like mush
Mafic recharge
Additional magma evolution
Magma ascent
Mafic parental melt of phonolitic lineage
B
0
5
10
15
20
25
30
35
Ocean
Sediments
Crust
Moho
Transient crustal stalling?
Progressive mush evacuation and dominance of basanite melts
Not to scale
Early-erupted tephrite-hosted cpx cargo
Recharge + fractionation
Formation of outer rims during ascent
Late-erupted basanite-hosted cpx cargo
Basanite recharge
Formation of outer rims during ascent

Recurrent evacuation of mantle mush by mafic recharge in ocean island basalts, recorded by La Palma clinopyroxene

Alberto Caracciolo, Teresa Ubide, Mónica Ágreda-López, Raquel Herrera, Alvaro Marquez, Diego González-García, Maria Jose Huertas, Eumenio Ancochea, Nicolás Chicharro, Juan Jesús Coello-Bravo, Maurizio Petrelli

Supplementary Material Text and Figures

Corresponding author: Alberto Caracciolo, (alberto@hi.is)

Table of Contents

1. Geological setting

The Canary Islands are an example of intraplate volcanism, commonly attributed to a hotspot beneath Jurassic oceanic lithosphere (Wilson, 1973), although alternative plate-related models have also been proposed (e.g. Anguita et al., 2025). La Palma is one of the westernmost and youngest islands of the archipelago. It is composed of the older, now extinct Garafía and Taburiente shield volcanoes in the north, and the younger, historically active Cumbre Vieja ridge in the south (Fig. 1). La Palma is the most volcanically active island in the Canaries during historical times, having experienced eight eruptions since the late 15th century, including the most recent Tajogaite eruption in 2021 (Carracedo et al., 2022; Hernandez-Pacheco and Valls, 1984). Historical eruptions occurred in 1470, 1585, 1677-78, 1712, 1949, 1971 and 2021, with return periods varying between 22 and 237 years (Longpré and Felpeto, 2021). Eruptions at Cumbre Vieja are typically strombolian, producing highly alkaline magma series, ranging from basanitic to tephritic lavas (Klugel et al., 1999) although more evolved phonolites are occasionally erupted (Klügel et al., 2022). In this work, we focus on the 1712 El Charco, 1971 Teneguía and 2021 Tajogaite eruptions (Fig. 1), for which we have well characterized samples across the tephrite and basanite stages.

The 1712 El Charco eruption is the least documented eruption of the Canaries and the available information is described by Romero Ruiz (1990). The 1712 eruption occurred in the central west part of Cumbre Vieja and began on October 9, with the opening of a main cone and multiple secondary vents along a 3 km-long fracture, trending SE–NW. Although there was some phreatomagmatic activity, the eruption was essentially strombolian, producing lava flows approximately 5 km in length that reached the sea, forming several lava deltas. The eruption lasted for 56 days, from October 9 to December 3, 1712 (Romero Ruiz, 1990). This event produced tephrite to basanite lavas (Chicharro Fermín, 2024), with an estimated total lava volume of 36 x 10^6 m^3 (Longpré and Felpeto, 2021). Samples for El Charco 1712 were collected from different parts of the lava field, and amphibole-bearing tephrites are consistently found at the bottom of the olivine-bearing basanites (Supplementary Data Table 1, SDT1).

The 1971 Teneguía eruption took place at the southern tip of La Palma, near the site of the 1677–1678 eruption. Activity began on October 26 with the opening of an eruptive fissure that produced pyroclastic material and lava flows, which rapidly reached the coast. Several vents were active during the eruption. The eruption continued for 24 days, ending on November 18, 1971. This event produced tephrite to basanite lavas and the total eruption volume is estimated to be 40 x 10^6 m^3 (Afonso et al., 1974; Longpré and Felpeto, 2021). Samples from the 1971 Teneguía eruption were collected during the eruption, allowing the construction of a time series of samples (SDT1).

The Tajogaite 2021 eruption began on 19 September 2021, at Cabeza de Vaca locality, in the middle part of Cumbre Vieja ridge. The eruption began with Strombolian activity and lava fountaining, transitioning to more intense lava and pyroclastic emissions from multiple vents in October–November 2021. Early tephritic magmas shifted to basanitic compositions over the first few days, with the eruption ending on 13 December 2021. The minimum erupted volume is estimated at 170 ± 85 x10^6 m^3 (Bonadonna et al., 2022). For this most recent eruption, modern geophysical and petrological monitoring provide a more detailed eruption evolution. The first signs of volcanic unrest preceding the 2021 Tajogaite eruption occurred in 2017, interpreted as related to magmatic intrusions (Fernández et al., 2021; Torres-González et al., 2020). After eight days of seismic swarms, the eruption began on 19 September 2021, producing tephritic magma rich in amphibole and clinopyroxene until the first break on 27 September (Pankhurst et al., 2022; Ubide et al., 2023). Following the few-hours long break, the eruption continued emitting more fluid basanite magmas, dominated by olivine and clinopyroxene crystals, until the end of the eruption, on 13 December 2021 (e.g. Day et al., 2022; Ubide et al., 2023). Temporal changes are observed during the 2021 Tajogaite eruption, the most significant being a shift towards more mafic melts over the course of the eruption, followed by a reversal in that trend since the end of November to the end of the eruption, as observed in clinopyroxene, plagioclase and olivine rims, microlites, matrix and whole rock compositions (Bonechi et al., 2024; Chamberlain et al., 2025; Day et al., 2022; Dayton et al., 2023; Ubide et al., 2023). The eruption is overall interpreted as a result of a mafic basanite magma gradually invading a tephrite reservoir (e.g. Day et al., 2022; Ubide et al., 2023), with the basanite sourced from the upper mantle and interacting with a tephrite reservoir located in the upper mantle (e.g. Chamberlain et al., 2025; Ubide et al., 2023) or in the middle to lower crust (Fabbrizio et al., 2023; Scarrow et al., 2024). Samples from Tajogaite 2021 eruption were collected both during and after the eruption and correspond to the same sample set published in Ubide et al. (2023) (SDT1).

2. EMPA methods

Clinopyroxene crystals from the different eruptions were analysed using three different electron microprobe analysers (EMPA). Data are reported in Supplementary Data Table 2 (SDT2).

Tajogaite 2021 crystals were analysed at the Centro Nacional de Microscopía Electrónica of the Complutense University in Madrid, Spain, using a JEOL JXA-8900M electron microprobe equipped with four wavelength-dispersive spectrometers (WDS). Measurements were conducted using a beam current of 20 nA, an accelerating voltage of 15 kV and a beam diameter of 5 µm. Elemental counting times were 10 s on the peak and 5 s on background positions. Calibration standards included: albite for Na and Si; sillimanite for Al; microcline for K; almandine for Fe and Mn; kaersutite for Mg, Ca, and

Ti; fluor-apatite for P, F, and Cl; and pure metal elements for Ni and Cr. Data were corrected using the ZAF matrix correction procedure. The analyses were conducted in 2021 and 2022, following the same procedure as described in Ubide et al. (2023), as the clinopyroxene data presented here were acquired during the same analytical sessions. These new EMPA data presented in this work complement the Ubide et al. (2023) dataset by adding crystal core and outer rim compositions to the previously reported crystal inner rim and microlite analyses.

El Charco 1712 crystals were analysed at the Unidad de Microscopía Electrónica of the University of Huelva, Spain, using a JEOL JXA-8200 electron microprobe, equipped with four WDS and one energy-dispersive X-ray spectrometer (EDS). Measurements were conducted using a beam current of 20 nA, an accelerating voltage of 15 kV and a beam diameter of 5 µm. Elemental counting times were set at 10 seconds on peak and 5 seconds on background for each element. Calibration standards included: K-feldspar for Al, Na, and K; wollastonite for Ca and Si; fayalite for Fe; forsterite for Mg; manganosite for Mn; chromite for Cr; rutile for Ti. Data were corrected using the ZAF matrix correction procedure.

Teneguía 1971 crystals were analysed at the Centro Nacional de Microscopía Electrónica of the Complutense University in Madrid, Spain, using a new JEOL Field Emission Gun (FEG) JXA-iHP200F electron microprobe, equipped with four WDS. Measurements were conducted using a beam current of 10 nA, an accelerating voltage of 15 kV and a beam diameter of 5 µm or a focused beam. Elemental counting times were 10s on the peak and 5s on background positions. Calibration standards and data correction procedure are the same as for the JEOL JXA-8900M microprobe described above.

To assess data consistency across three microprobe instruments, we re-analyzed selected clinopyroxene crystals of the 1712 (30 analyses) and 2021 (38 analyses) samples using the new JEOL JXA iHP200F electron microprobe at the Centro Nacional de Microscopía Electrónica (Madrid). Re-analyses were conducted at the same locations as the original analyses. Overall, the new data are consistent with the original measurements within analytical uncertainty (based on Poisson statistics), confirming the robustness and inter-instrument reproducibility of the dataset (Fig. S1-S2). Minor offsets observed in some analyses likely reflect minor positional offsets or patchy crystal domains. Data quality was monitored by analyzing clinopyroxene secondary standards from the Smithsonian Institution of Washington (Kakanui augite NMNH 122142, Cr-augite NMNH 164905 and Diopside NMNH 117733). Accuracy and precision determined using the Cr-augite standard NMNH 164905, which closely matches the composition of our samples, are better than 1–6% and 1–3% for major elements, respectively. For minor elements, accuracy ranges from 2–7% and precision from 1–8%, except for Mn, which exceeds 10%. Data of secondary standards are reported at the bottom of SDT3.

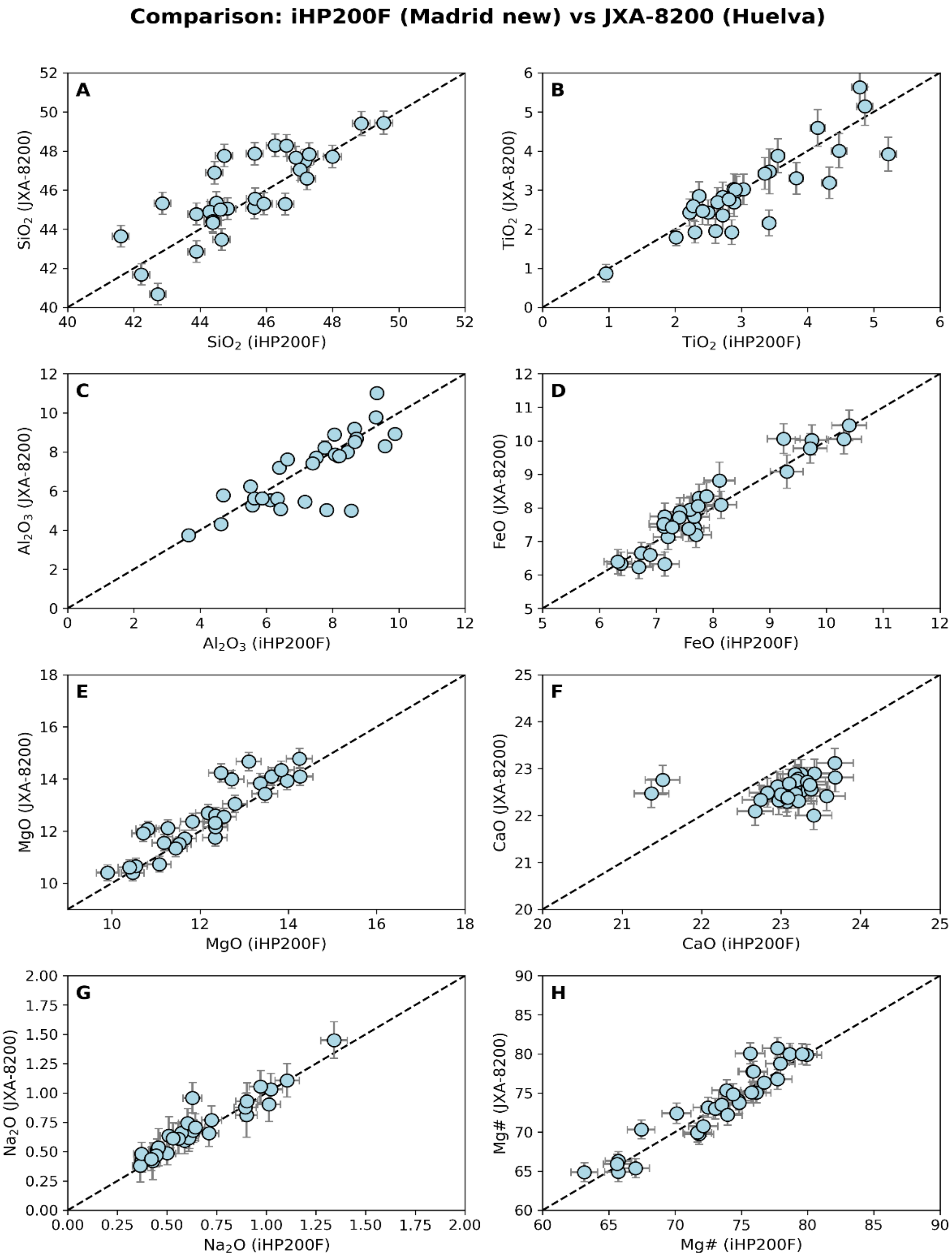

Fig. S1. EMPA Comparison El Charco 1712. Comparison of major and minor element data for samples from El Charco 1712 collected with the new iHP200F microprobe in Madrid and JXA-8200 microprobe in Huelva. Error bars indicate 2σ uncertainties derived from EMPA counting statistics.

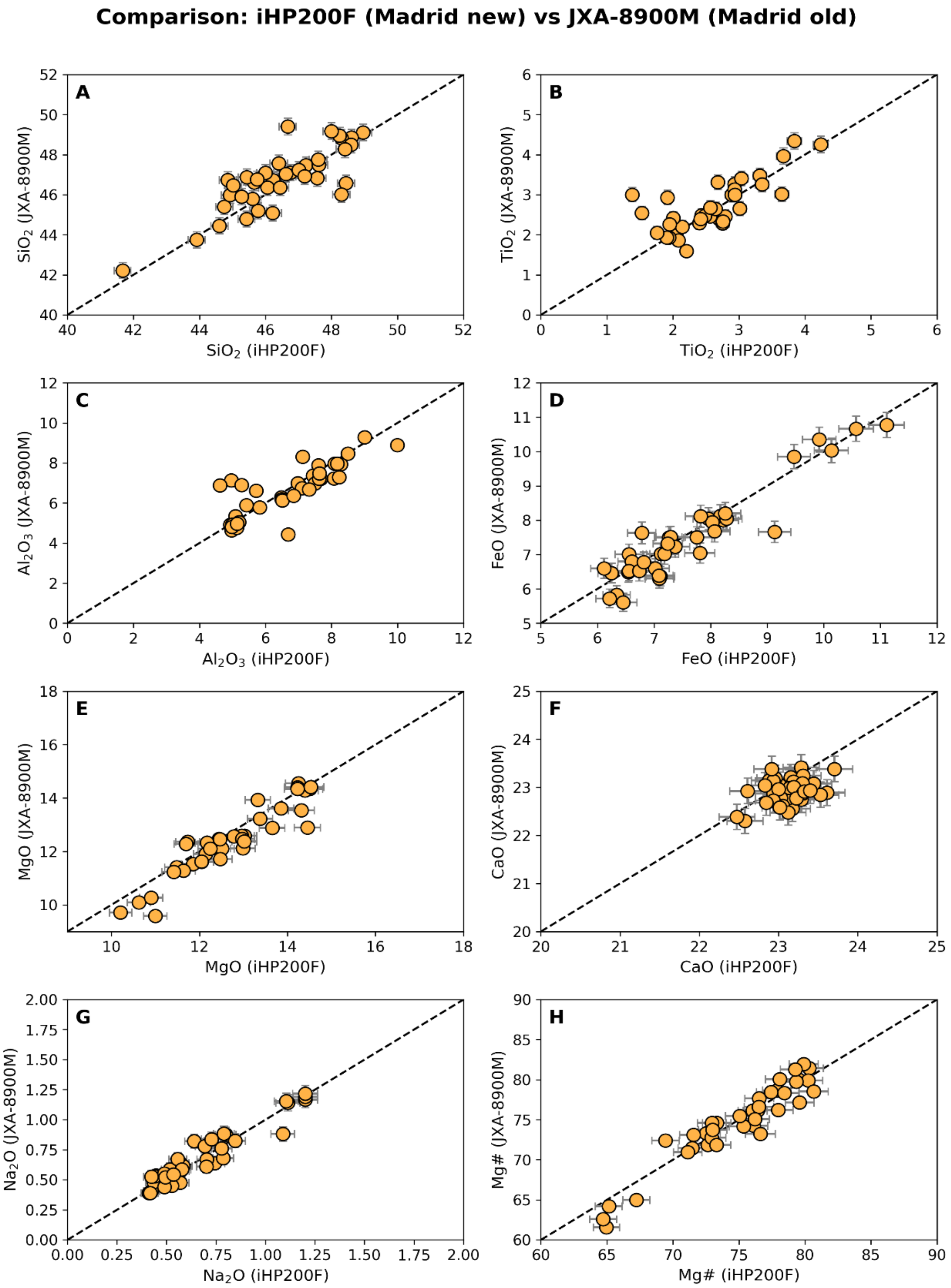

Fig. S2. EMPA Comparison Tajogaite 2021. Comparison of major and minor element data for samples from Tajogaite 2021 collected with the iHP200F microprobe in Madrid and the old JXA-8900M microprobe in Madrid. Error bars indicate 2σ uncertainties derived from EMPA counting statistics.

3. LA-ICP-MS methods

LA-ICP-MS was used to determine trace element compositions of clinopyroxene crystals via single-spot analyses (following Petrelli et al. 2016) (Supplementary Data Table 4, SDT4), to acquire quantitative trace element maps of clinopyroxene (following Ágreda-López et al. 2025) (Zenodo repository 10.5281/zenodo.17635257) and to measure major and trace element compositions of the microcrystalline matrix (following the rastering method of Ubide et al. 2023) (Supplementary Data Table 6, SDT6). LA-ICP-MS analyses were done at the Dipartimento di Fisica e Geologia, University of Perugia, using a 193 nm Analyte G2 laser ablation system operated with Chromium software coupled to a quadrupole iCAP-Q ICP-MS (Thermo Fisher Scientific) operated with Qtegra software. For all analyses, helium carrier gas was set to 0.6 and 0.3 L min^{-1} for the ablation cell and cup, respectively.

Matrix compositions were analysed following the method described in Ubide et al. (2023), consisting in laser rastering over equigranular microcrystalline areas via overlapping spots. In total, 10 rasters were acquired per thin section across four thin sections (two basanite and two tephrite samples) from the El Charco 1712 and Teneguía 1971 eruptions. These data are complemented by matrix analyses from Tajogaite 2021 eruption published in Ubide et al. (2023), to which the reader can refer for full details on analytical conditions and matrix data reduction, which uses BCR-2G glass reference material as external standard and normalisation to total 100wt.% oxides as internal standard. For major elements, accuracy and precision were assesed using glass reference materials BHVO-2G and GSD-1G, resulting mostly in values <5% and always better than 8% (Supplementary Data Table 7, SDT7). For trace elements, accuracy was monitored using glass reference materials BHVO-2G, GSD-1G, NIST-610 and NIST-612 (Supplementary Data Table 8, SDT8). Accuracy for BHVO-2G and GSD-1G is within 5–10% relative to accepted values, except for Ta which was ~13%. Precision is always <3% for both major and trace elements (SDT7-8).

Trace element composition of clinopyroxene single-spots were acquired using a spot size of 30 µm and repetition rate of 10 Hz. Data reduction was performed using Iolite (Paton et al., 2011), using a 3D trace element calibration including NIST-SRM610, NIST-SRM612, GSD-1G and BHVO-2G as the calibrators, Ca as measured by EMPA as the internal standard, and USGS-BCR2G as the quality control. This configuration ensured precision and accuracy within ±5% for most analysed trace elements, with all elements exhibiting accuracy better than ±10% (Supplementary Data Table 5, SDT5).

Compositional maps of clinopyroxene were acquired using oversampling, by overlapping laser squares to generate subsequent ablation lines that build the mapped area (Ubide et al., 2015). We used a spot size of 10 µm, resulting in a resolution of 5 µm (Ágreda-López et al., 2025). Dosage was set at 10, Scan speed at 100 µm/s, and the repetition rate at 100 Hz. We analysed 10 elements (Ca, Sc, Ti, V, Cr, Mn, Ni, Sr, Zr, Ce). NIST-SRM610 was used as a calibration standard and Ca was used as internal standard. Measurements of the secondary standard USGS-BCR2G alongside the unknown maps yielded accuracies better than 10% relative to preferred values for all elements, except Sc, which was within 15%. Precision was better than 10% relative standard deviation, with most elements showing precision between 0% and 5% (Supplementary Data Table 5, SDT5). Clinopyroxene maps can be found in the Zenodo repository at this link: 10.5281/zenodo.17635257.

4. Processing of LA-ICP-MS trace element maps

Data processing and image reconstruction of chemical maps were performed using HDIP software (Teledyne Photon Machines). HDIP was used to align and calibrate raw LA-ICP-MS signal intensities, reconstruct the spatial distribution of each element, and export fully calibrated concentration matrices (in ppm) of clinopyroxene crystals. This was done by manually segmenting clinopyroxene crystals within each map and removing the surrounding microcrystalline groundmass, mineral oxides, mineral inclusions, large cracks, and voids. Additionally, we retained only data between the 1st and 99th percentile to eliminate outlier spikes. Clinopyroxene matrices were subsequently processed and visualized using a Python script designed to apply one of three alternative scaling approaches, logarithmic scaling, histogram equalization (HE), or adaptive histogram equalization (AHE), to enhance chemical contrast, depending on the statistical distribution and dynamic range of each element. Logarithmic transformation was applied when elemental concentrations spanned several orders of magnitude, helping to highlight subtle variation in low-concentration domains that would otherwise be suppressed by linear rescaling. Histogram equalization, a global contrast enhancement technique, was applied to datasets with moderate skew to redistribute pixel intensities and make use of the full dynamic range of the display. For highly skewed or spatially heterogeneous data, adaptive histogram equalization was employed. Unlike the HE method, AHE operates on small image regions to enhance local contrast and resolve fine-scale compositional structures. The most appropriate visualization method was automatically selected for each element by comparing visual contrast and feature detectability.

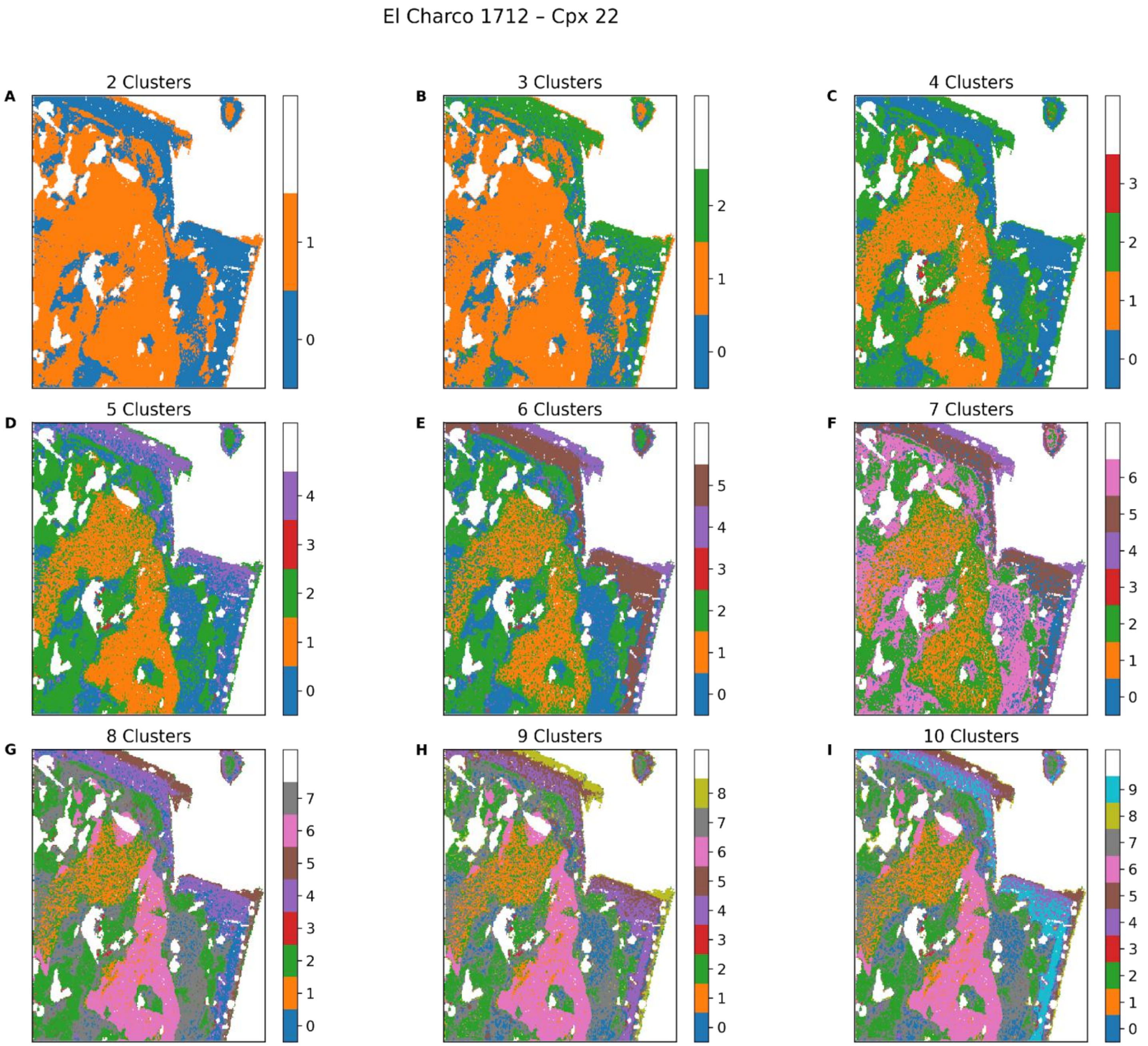

Fig. S3. Clustering number. Example of a clinopyroxene map from El Charco 1712 (Cpx 22), color-coded according to varying numbers of clusters (ranging from 2 to 10). Based on visual inspection, we consider 6 clusters to be the optimal number, as it avoids both oversimplification and excessive complexity of the chemical variations.

5. Thermobarometry methods

Magma storage pressures were estimated using clinopyroxene-melt barometers following guidelines for clinopyroxene-melt equilibrium and selection of calibrations provided by MacDonald et al. (2023), who found that thermobarometers calibrated on isothermal–isobaric experimental datasets (Putirka, 2008; Putirka et al., 2003) yield greater accuracy under low undercooling conditions, whereas those incorporating decompression and undercooling experiments (Mollo et al., 2018) perform better at higher degrees of undercooling. Low undercooling is typically associated with the formation of crystal cores and sector zoned compositions, while high undercooling occurs during magma decompression and degassing, promoting the crystallization of crystal rims and microlites (MacDonald et al., 2023). Hence, we used the barometer from Putirka et al. (2003) (SEE= ± 1.7 kbar, 5.6 km) coupled with the thermometer from Putirka (2008) (Eq. 33, SEE= ±45 °C) for clinopyroxene cores and inner rim compositions, whereas for clinopyroxene outer rims and microlites we used the thermobarometer by Mollo et al. (2018) (SEE= ± 1.5 kbar, 4.9 km and ± 28 °C). These thermobarometers are calibrated for mafic alkaline magmas. For evolved clinopyroxene core compositions, here defined as cores with Mg#<67, we employed a thermobarometer specific for differentiated alkaline magmas by Masotta et al. (2013) (SEE= ± 1.15 kbar, ± 3.8 km and ± 18.2 ºC).

We applied an eruption-specific clinopyroxene–melt matching approach, pairing clinopyroxene compositions with melt compositions from the same eruption. We used clinopyroxene and melt compositions from this study (SDT2 and SDT6) and from the literature (Supplementary Data Table 9 and 10, SDT9-SDT10). For Tajogaite 2021, we used 422 clinopyroxene compositions from this study and 904 from the literature (González-García et al., 2023; Ubide et al., 2023). Melt compositions for Tajogaite 2021 included groundmass and tephra glass (n = 708), microcrystalline groundmass or matrix (n = 176), and melt inclusions (MI, n = 72) from the literature (Day et al., 2022; Longpré et al., 2025; Pankhurst et al., 2022; Ubide et al., 2023). For the 1971 Teneguía eruption, clinopyroxene compositions come exclusively from this study (n = 164). Data from Barker et al. (2015) and Weis et al. (2015) were not included as they show systematically lower CaO and higher Na_2O contents compared to published data (Fig. S8). Melt compositions comprised matrix glass data from this study (n = 40) and one glass composition from the literature (Klügel et al., 2005). For the El Charco 1712 eruption, we used 213 clinopyroxene compositions from this study. Melt compositions included matrix glass (n = 40) from this study and one glass analysis from Klügel et al. (2005). Evolved clinopyroxene core compositions were paired with one titanite-hosted, tephriphonolite melt pocket composition found in a plagioclase macrocryst from the 2021 Tajogaite eruption (Jegal et al., 2025). To increase the number of equilibrium pairs for evolved clinopyroxene cores, we performed a Monte Carlo simulation, varying the starting melt pocket composition by ±5%, generating 1000 compositions to capture analytical variability. Equilibrium between clinopyroxene and putative melts was evaluated by selecting clinopyroxene–melt pairs that met four criteria based on the agreement between measured and predicted components: DiHd (diopside + hedenbergite) within ±10%, EnFs (enstatite + ferrosilite) within ±5%, CaTs (calcium–tschermak component) within 6%, and CaTi (calcium–titanium component) within ±2% (MacDonald et al., 2023). Melt H_2O concentration was set at 1 wt% for the tephrite-basanite magma, as suggested for the 2021 Tajogaite primitive magma (Andújar et al., 2025), and to 3 wt% for evolved core compositions (Klügel et al., 2022). However, we note that H_2O has little effect on thermobarometry calculations (Klügel et al., 2022; Ubide et al., 2023). All calculations were performed with the Thermobar Phyton tool (Wieser et al., 2022).

Throughout this work, we base our conclusions on thermobarometry calculations obtained following guidelines from MacDonald et al. (2023), as their equilibrium criteria improve precision of pressure and temperature estimates of sector zoned clinopyroxene compositions. However, to increase the number of clinopyroxene–melt equilibrium pairs and evaluate different thermobarometric calibrations (Mollo et al., 2018; Neave and Putirka, 2017; Putirka, 2008; Putirka et al., 2003), we applied alternative thermobarometric approaches using a more relaxed set of equilibrium criteria (Fig. S4-S5). These required differences between measured and predicted clinopyroxene components to be within 12% for DiHd, 10% for EnFs, and 6% for CaTs, within 2σ of the thresholds proposed by Neave et al. (2019), and a ($K_D(Fe–Mg)_{cpx–melt}$) of 0.28 ± 0.08 (Putirka, 2008). Overall, this alternative approach yields a larger number of clinopyroxene–melt equilibrium pairs and results comparable to those obtained using the MacDonald et al. (2023) guidelines (Fig. S4-S5).

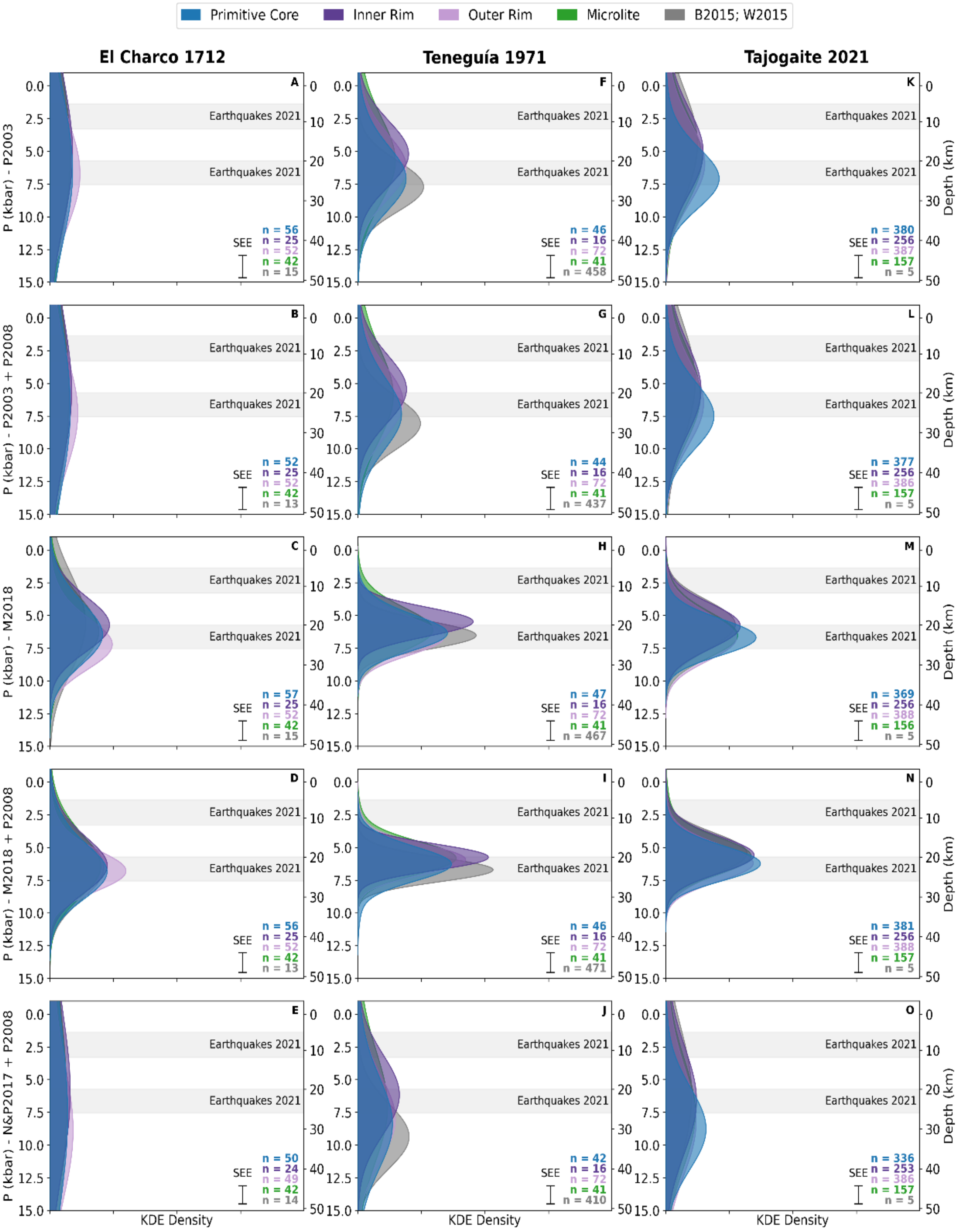

Primitive Core
Inner Rim
Outer Rim
Microlite
B2015; W2015
El Charco 1712
Teneguía 1971
Tajogaite 2021
P (kbar) - P2003
P (kbar) - P2003 + P2008
P (kbar) - M2018
P (kbar) - M2018 + P2008
P (kbar) - N&P2017 + P2008
Depth (km)
KDE Density
Earthquakes 2021
SEE
0.0
2.5
5.0
7.5
10.0
12.5
15.0
0
10
20
30
40
50
A
n = 56
n = 25
n = 52
n = 42
n = 15
B
n = 52
n = 25
n = 52
n = 42
n = 13
C
n = 57
n = 25
n = 52
n = 42
n = 15
D
n = 56
n = 25
n = 52
n = 42
n = 13
E
n = 50
n = 24
n = 49
n = 42
n = 14
F
n = 46
n = 16
n = 72
n = 41
n = 458
G
n = 44
n = 16
n = 72
n = 41
n = 437
H
n = 47
n = 16
n = 72
n = 41
n = 467
I
n = 46
n = 16
n = 72
n = 41
n = 471
J
n = 42
n = 16
n = 72
n = 41
n = 410
K
n = 380
n = 256
n = 387
n = 157
n = 5
L
n = 377
n = 256
n = 386
n = 157
n = 5
M
n = 369
n = 256
n = 388
n = 156
n = 5
N
n = 381
n = 256
n = 388
n = 157
n = 5
O
n = 336
n = 253
n = 386
n = 157
n = 5

Fig. S4. Comparison of P results. Comparison of clinopyroxene – melt magma storage depths using different temperature-dependent barometers coupled with different thermometers. For this comparison we used more relaxed equilibrium criteria as explained in Supplementary Section 5. P2003: barometer of Putirka et al. (2003), coupled with the thermometer of Putirka et al. (2003). P2003 + P2008: barometer of Putirka et al. (2003), coupled with the thermometer (eq. 33) of Putirka (2008). M2018: barometer of Mollo et al. (2018), coupled with thermometer of Mollo et al. (2018). M2018 + P2008: barometer of Mollo et al. (2018), coupled with thermometer (eq. 33) of Putirka (2008). N&P2017 + P2008: barometer of Neave & Putirka (2017) coupled with thermometer (eq. 33) of Putirka (2008). Overall, we note only minor differences among the various calibrations, all of which suggest clinopyroxene crystallization in the upper mantle. Gray fields indicate the location of seismicity during the 2021 Tajogaite eruption (D'Auria et al., 2022). B2015: Barker et al. (2015). W2015: Weis et al. (2015).

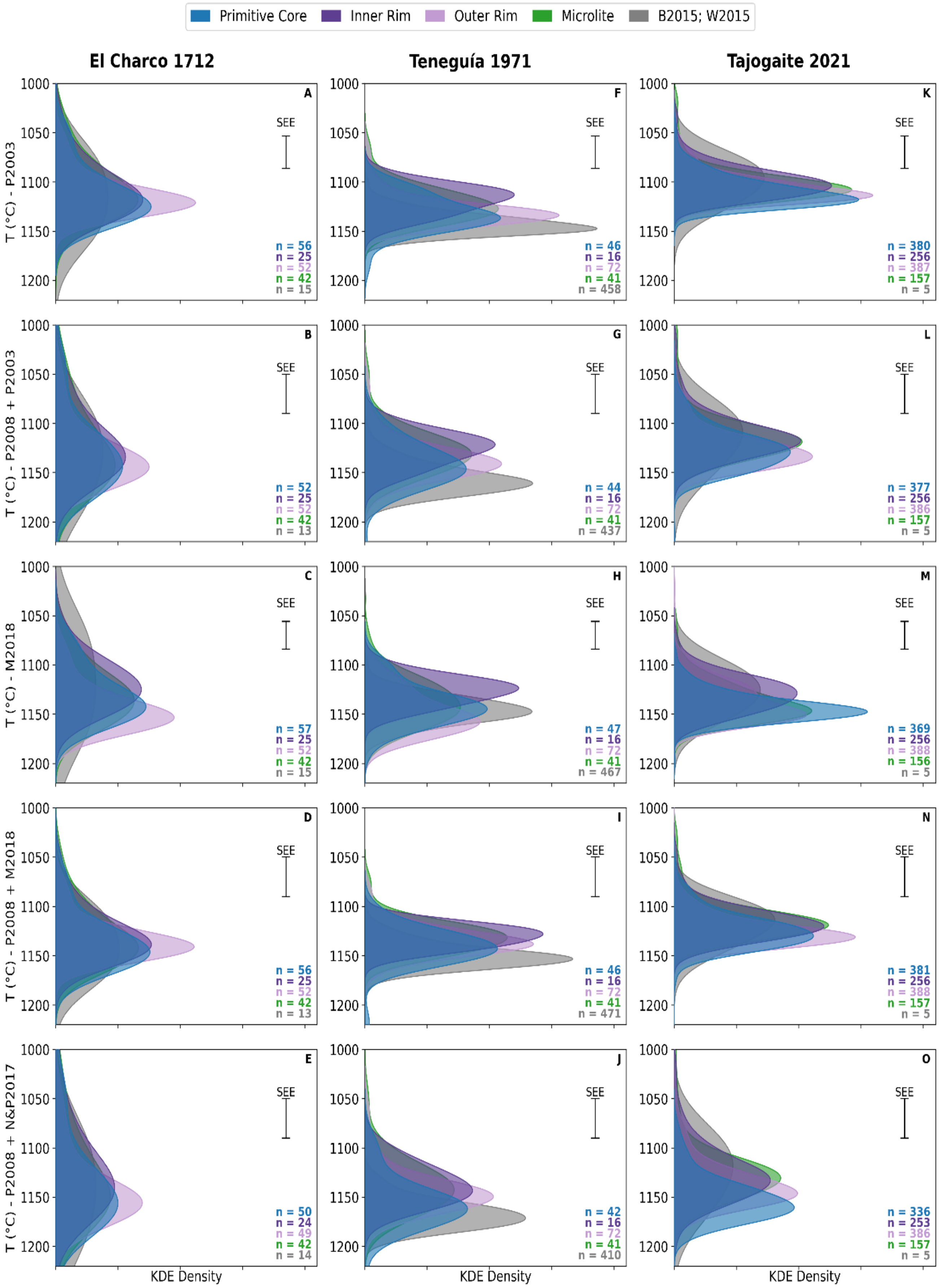
Primitive Core
Inner Rim
Outer Rim
Microlite
B2015; W2015
El Charco 1712
Teneguía 1971
Tajogaite 2021
T (°C) - P2003
T (°C) - P2008 + P2003
T (°C) - M2018
T (°C) - P2008 + M2018
T (°C) - P2008 + N&P2017
1000
1050
1100
1150
1200
SEE
A
n = 56
n = 25
n = 52
n = 42
n = 15
B
n = 52
n = 25
n = 52
n = 42
n = 13
C
n = 57
n = 25
n = 52
n = 42
n = 15
D
n = 56
n = 25
n = 52
n = 42
n = 13
E
n = 50
n = 24
n = 49
n = 42
n = 14
F
n = 46
n = 16
n = 72
n = 41
n = 458
G
n = 44
n = 16
n = 72
n = 41
n = 437
H
n = 47
n = 16
n = 72
n = 41
n = 467
I
n = 46
n = 16
n = 72
n = 41
n = 471
J
n = 42
n = 16
n = 72
n = 41
n = 410
K
n = 380
n = 256
n = 387
n = 157
n = 5
L
n = 377
n = 256
n = 386
n = 157
n = 5
M
n = 369
n = 256
n = 388
n = 156
n = 5
N
n = 381
n = 256
n = 388
n = 157
n = 5
O
n = 336
n = 253
n = 386
n = 157
n = 5
KDE Density
KDE Density
KDE Density

Fig. S5. Comparison of T results. Comparison of clinopyroxene – melt magma storage temperatures using different pressure-dependent thermometers coupled with different barometers. P2003: thermometer of Putirka et al. (2003), coupled with the barometer of Putirka et al. (2003). P2003 + P2008: thermometer of Putirka et al. (2003), coupled with the barometer (eq. 33) of Putirka (2008). M2018: thermometer of Mollo et al. (2018), coupled with barometer of Mollo et al. (2018). M2018 + P2008: thermometer of Mollo et al. (2018), coupled with barometer (eq. 33) of Putirka (2008). N&P2017 + P2008: thermometer of Neave & Putirka (2017) coupled with barometer (eq. 33) of Putirka (2008).

6. Clinopyroxene major elements

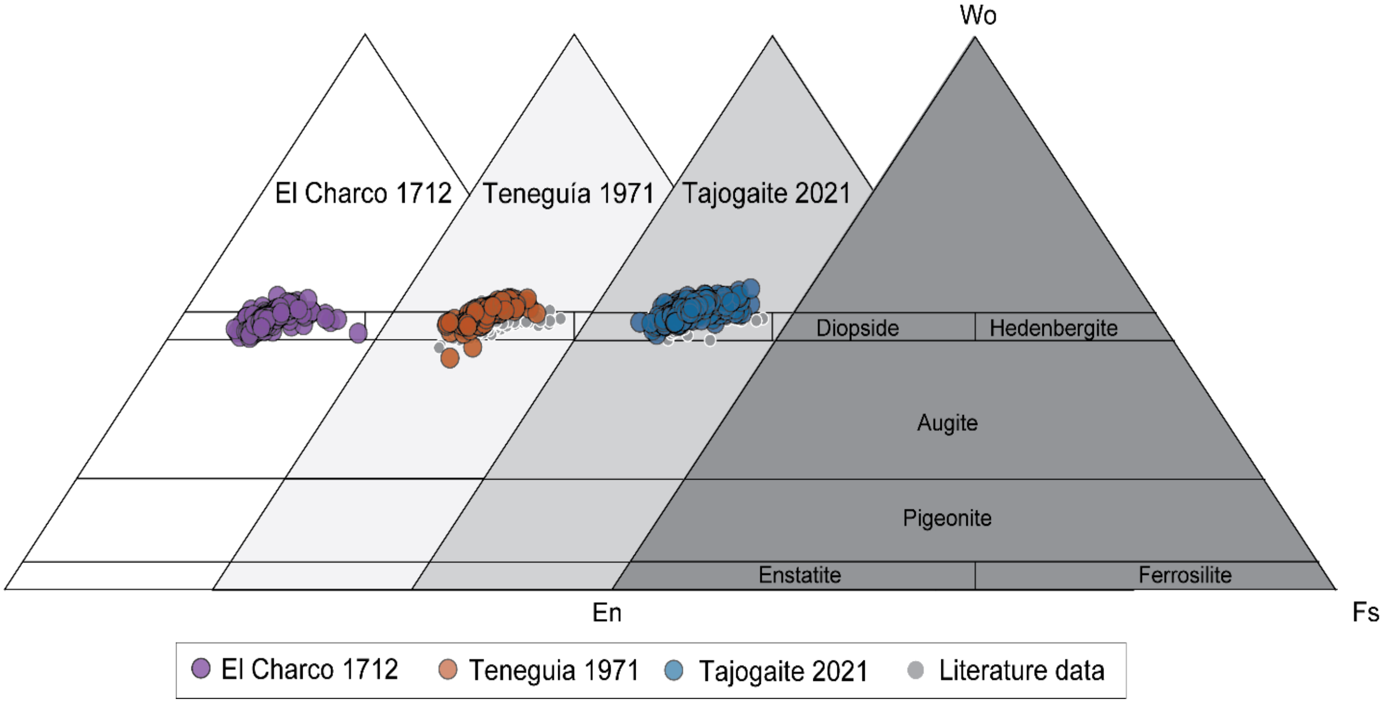

Fig. S6. Classification of Cpx. Composition of clinopyroxene crystals in the En-Fs-Wo ternary diagram. All compositions plot within the diopside field, with no differences between eruptions. Gray symbols represent clinopyroxene data from the literature (Barker et al., 2015; González-García et al., 2023; Ubide et al., 2023; Weis et al., 2015).

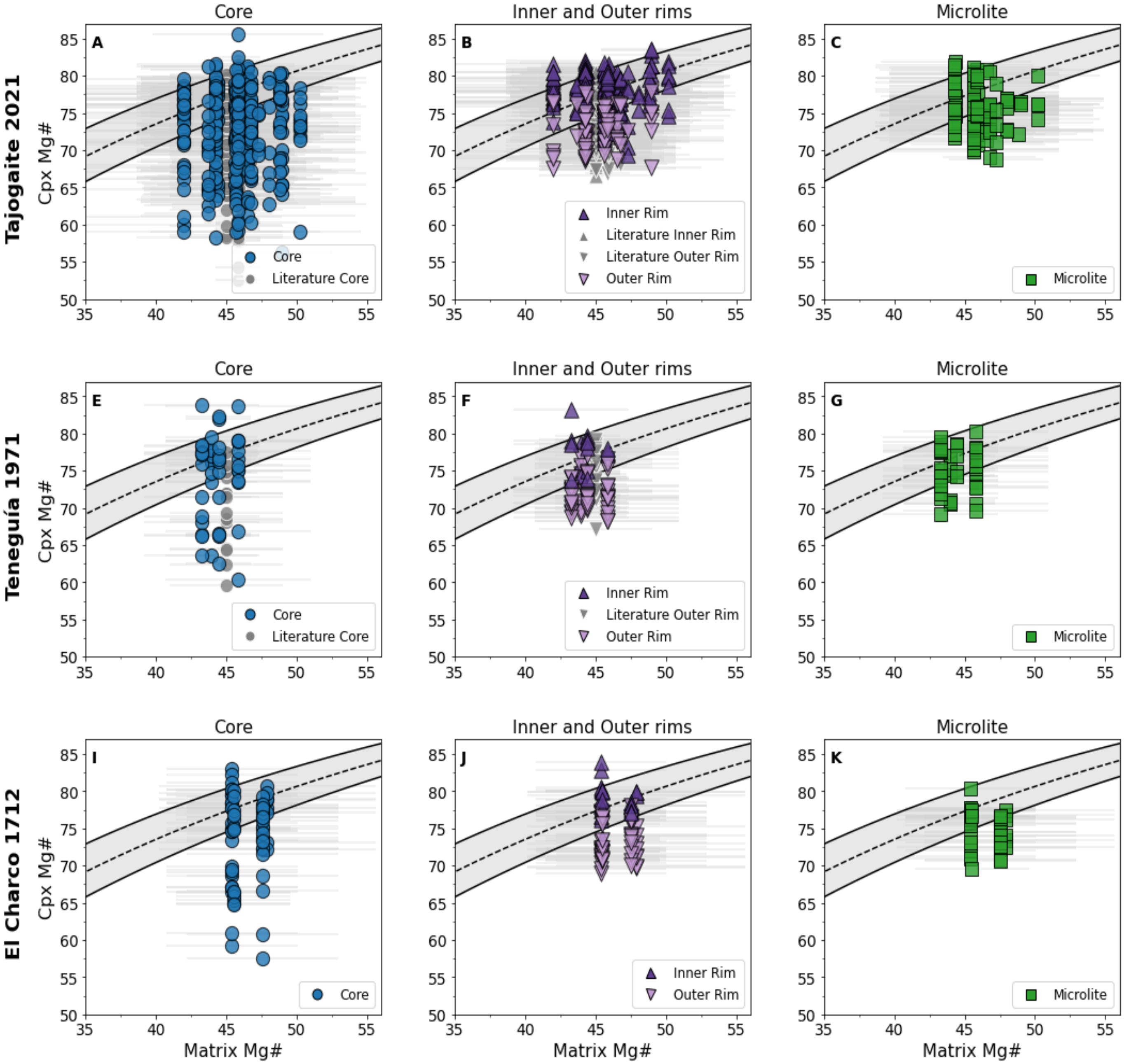

Fig. S7. Cpx – melt equilibrium. Matrix Mg# vs clinopyroxene Mg# for (A-C) Tajogaite 2021 (E-G) Teneguía 1971 and (I-K) El Charco 1712. Each symbol and color represent a different textural position (Core, Inner and Outer rims, Microlites, and Cpx inclusions), as indicated in the legend. Gray symbols correspond to literature data (Barker et al., 2015; González-García et al., 2023; Weis et al., 2015). Inner rim and microlite compositions from the 2021 Tajogaite eruption are from Ubide et al. (2023). The gray field in each panel indicates the KD(Fe–Mg)$_{cpx-melt}$ of 0.28 ± 0.08 (Putirka, 2008), which is used to assess major element equilibrium between clinopyroxene and the matrix composition. Horizontal error bars reflect the matrix Mg# 2σ variability.

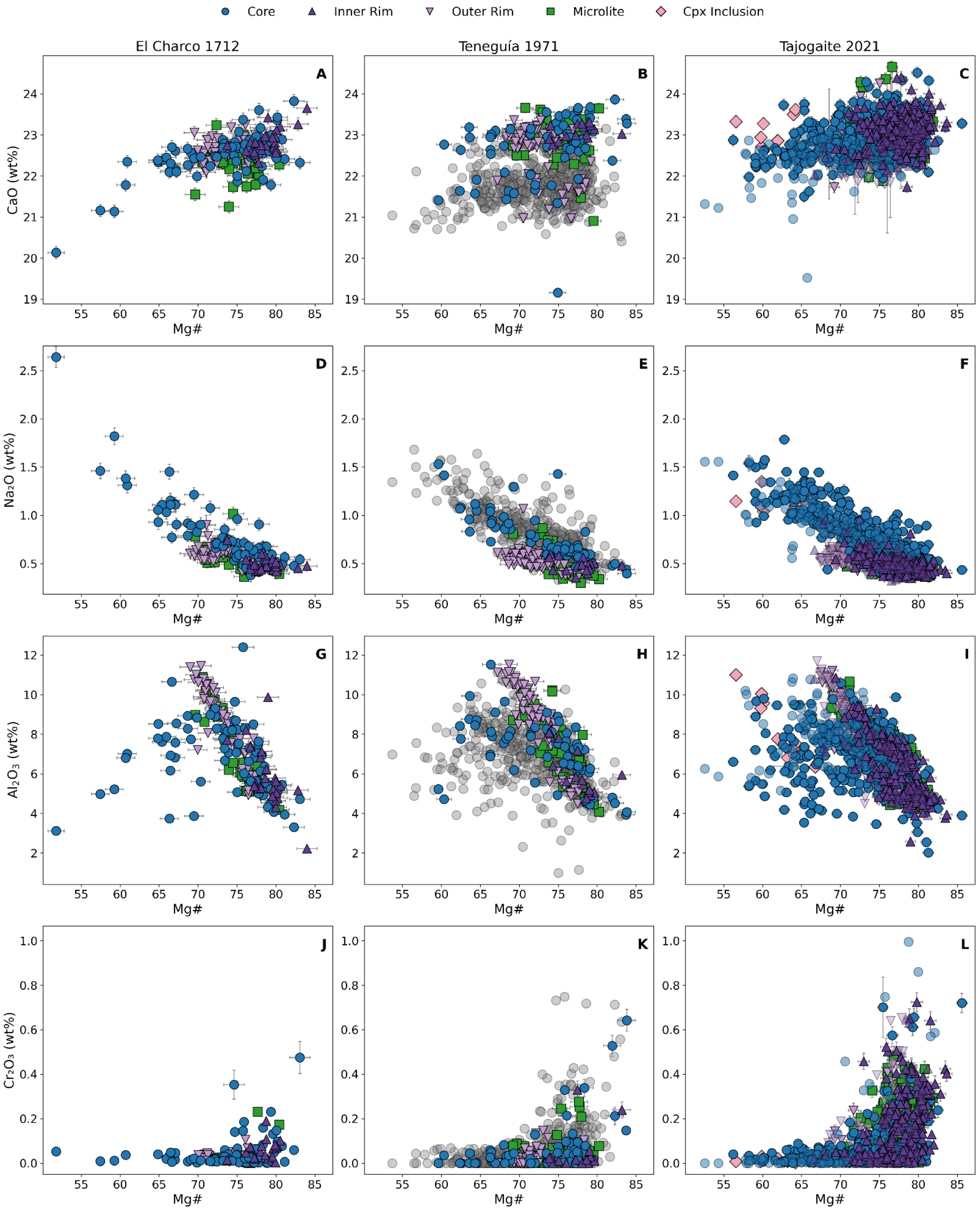

Fig. S8. Cpx major element. CaO, Na_2O, Al_2O_3 and Cr_2O_3 variation in clinopyroxene from the different eruptions studied in this work, with symbols and colors based on different textural positions. Literature data for Teneguía 1971 from Barker et al. (2015) and Weis et al. (2015) are not grouped into textures and are ploted as filled faded grey circles. For Tajogaite 2021, literature data are from González-García et al. (2023), shown with faded colours according to textural positions. We observe an offset in CaO contents between our data and previously published data from Teneguía, and a minor offset also in Na_2O and Al_2O_3 (Barker et al., 2015; Weis et al., 2015). We consider our measurements of good quality, as they closely match concentrations in clinopyroxenes from other eruptions, which were analyzed using various microprobes. The data quality is further supported by our cross-validation across instruments (see Fig. S1-S2). In contrast, the literature data from Teneguía (Barker et al., 2015; Weis et al., 2015) were acquired using the same instrument (JEOL JXA-8530F at Uppsala University), and the observed discrepancy may reflect a calibration issue specific to CaO and on that instrument. Error bars indicate 2σ uncertainties derived from EMPA counting statistics.

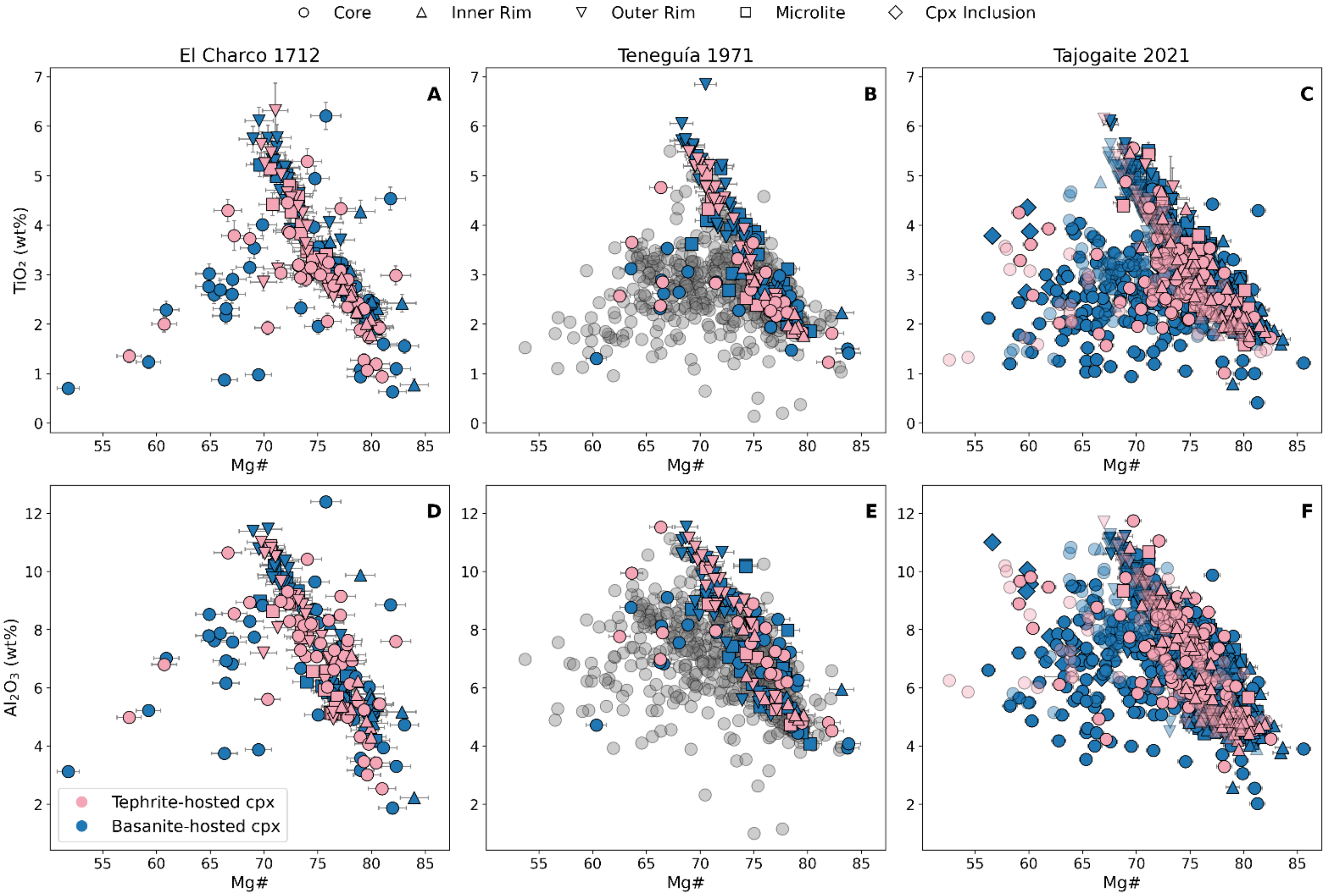

Fig. S9. Tephrite and Basanite-hosted Cpx. (A–C) TiO_2 and (D–F) Al_2O_3 variations as a function of Mg# in clinopyroxene, color-coded based on whether they occur in amphibole-bearing tephrite (pink) or olivine-bearing basanite (blue) rocks. No clear relationship is observed between clinopyroxene composition and rock type. . Literature data for Teneguía 1971 from Barker et al. (2015) and Weis et al. (2015) are plotted as faded filled grey circles. For Tajogaite 2021, literature data are from González-García et al. (2023), shown with faded colors. Error bars indicate 2σ uncertainties derived from EMPA counting statistics.

7. Clinopyroxene trace elements

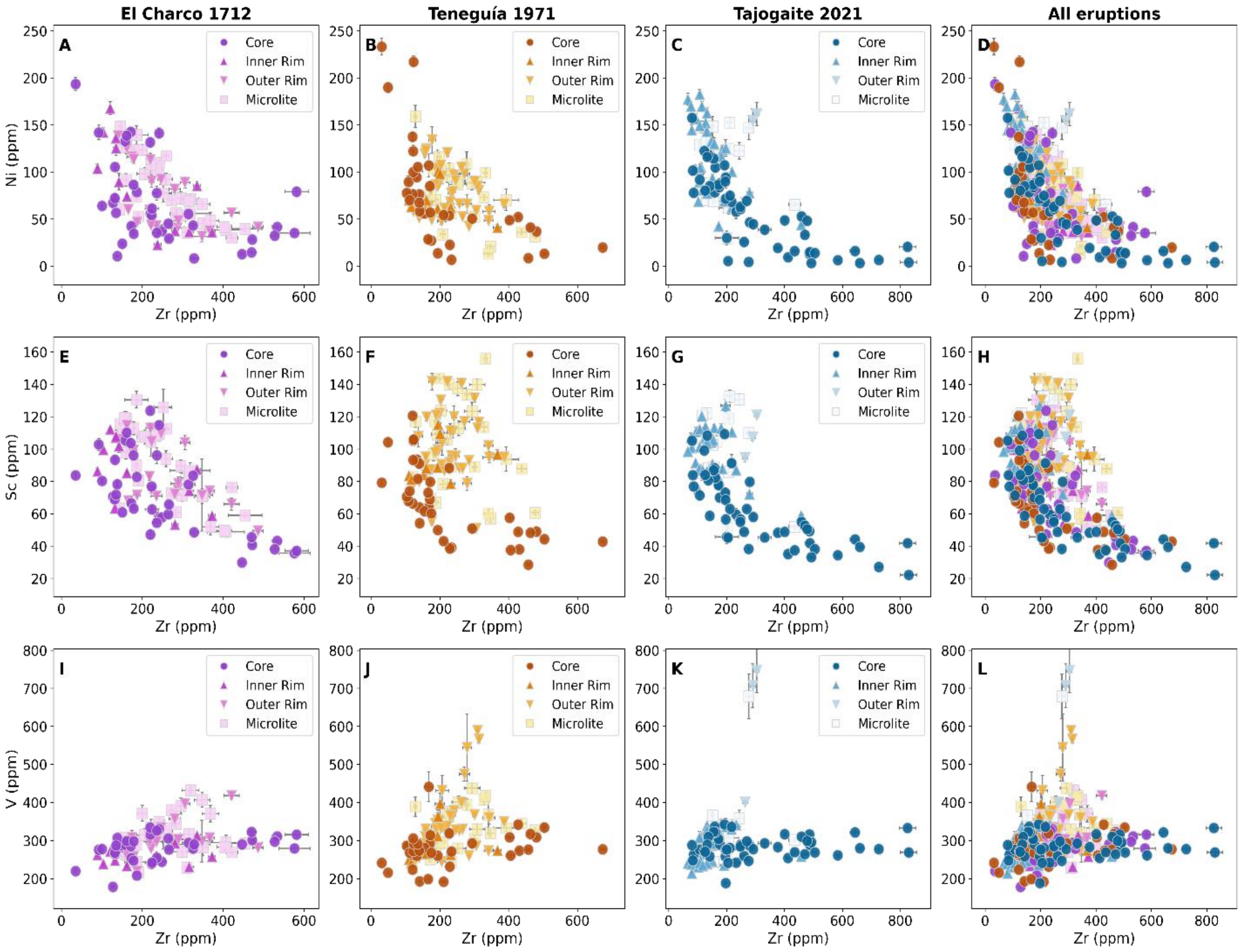

Fig. S10. Cpx compatible TE composition (NI, Sc, V). Clinopyroxene trace element bivariant plots of (A-D) Ni (E-H) Sc and (I-L) V vs Zr. Each column corresponds to a different eruption, as indicated by the column titles, with the final column showing data from all eruptions combined. Each symbol represents a different clinopyroxene textural position. Error bars indicate the internal 2SE analytical uncertainty.

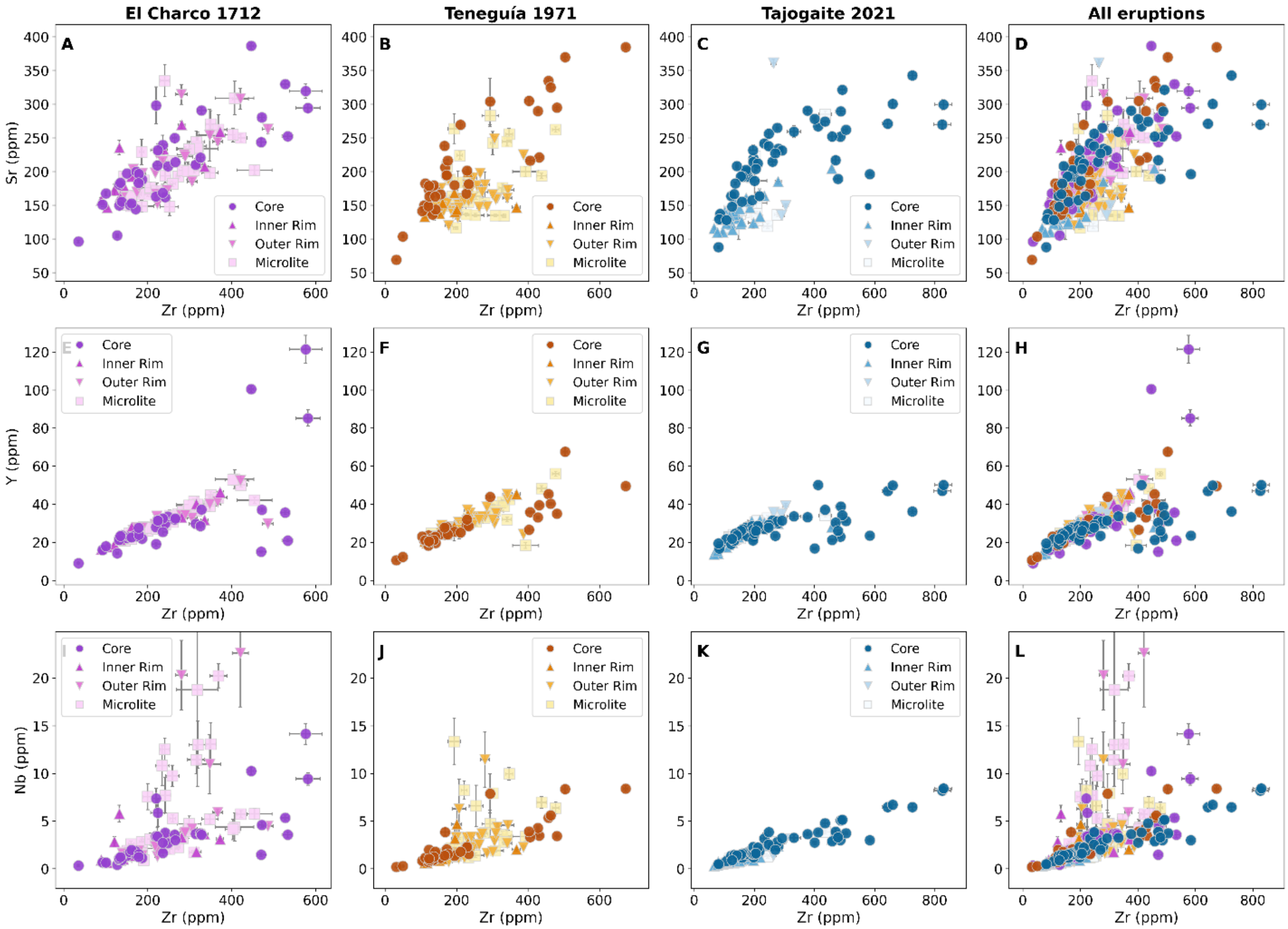

Fig. S11. Cpx incompatible TE composition (Sr, Y, Nb). Clinopyroxene trace element bivariant plots of (A-D) Sr (E-H) Y and (I-L) Nb vs Zr. Each column corresponds to a different eruption, as indicated by the column titles, with the final column showing data from all eruptions combined. Each symbol represents a different clinopyroxene textural position. Error bars indicate the internal 2SE analytical uncertainty.

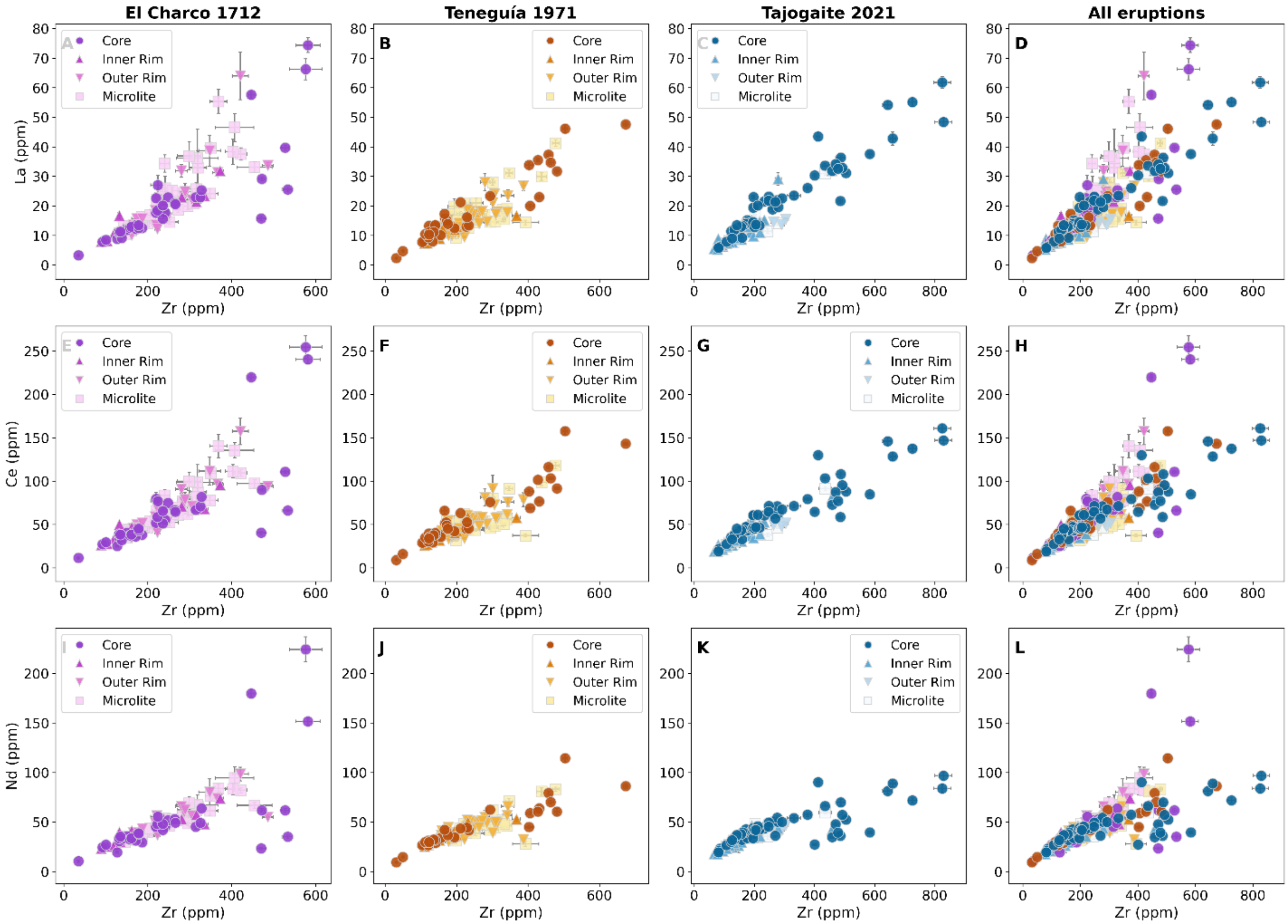

Fig. S12. Cpx incompatible TE composition (La, Ce, Nd). Clinopyroxene trace element bivariant plots of (A-D) La (E-H) Ce and (I-L) Nd vs Zr. Each column corresponds to a different eruption, as indicated by the column titles, with the final column showing data from all eruptions combined. Each symbol represents a different clinopyroxene textural position. Error bars indicate the internal 2SE analytical uncertainty.

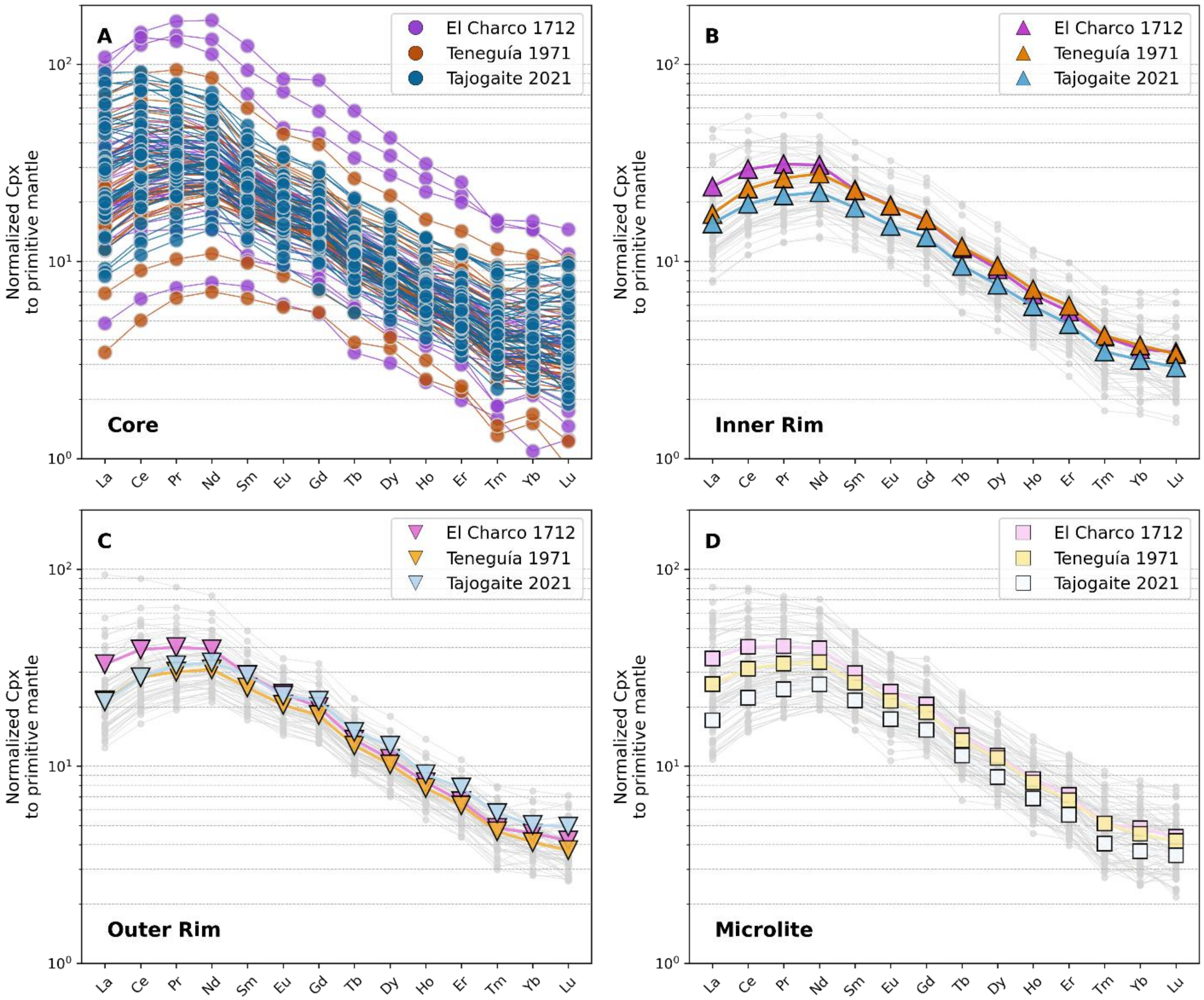

Fig. S13. Texture-grouped cpx REE patterns. Rare earth element (REE) patterns of clinopyroxene, normalized to the composition of primitive mantle (Palme and O'Neill, 2014). REE patterns of cores are shown as individual data, whereas for inner rims, outer rims, and microlites we show the average for each eruption, with individual patterns displayed in light grey.

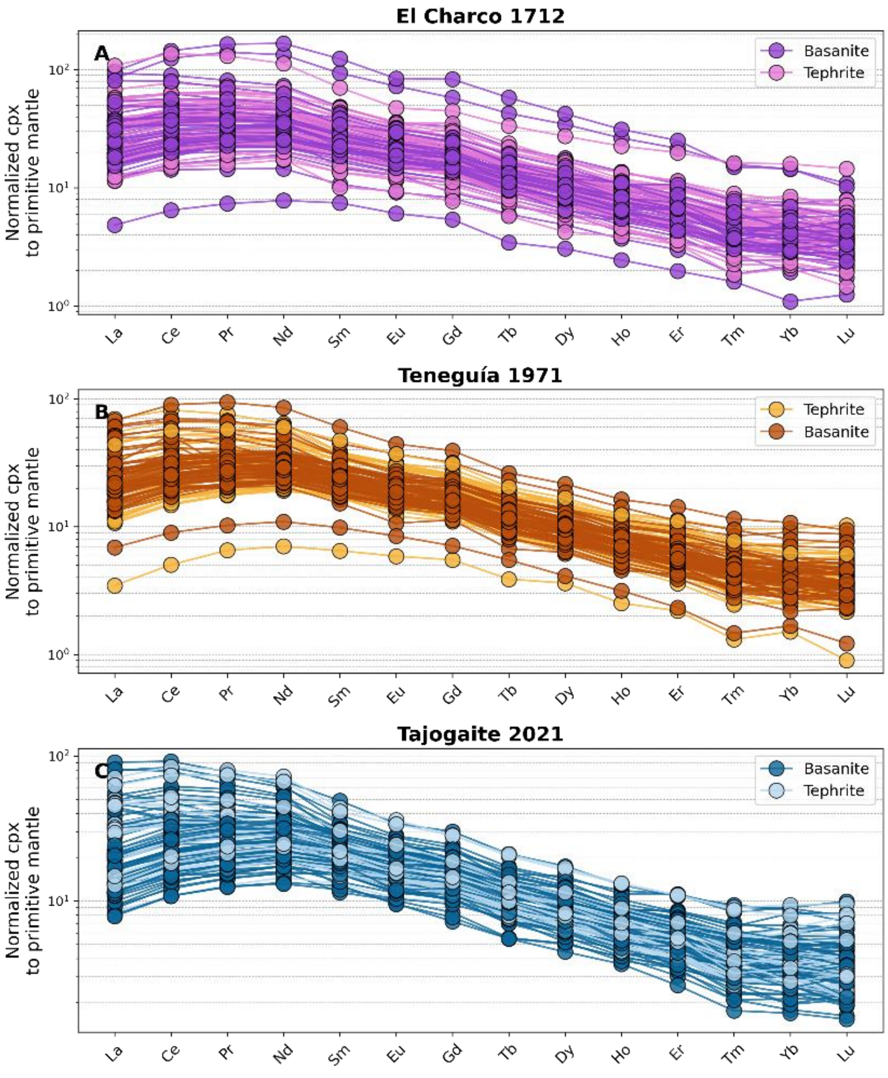

Fig. S14. Rock-grouped cpx REE patterns. Clinopyroxene trace element patterns colored by host rock type, tephrite and basanite.

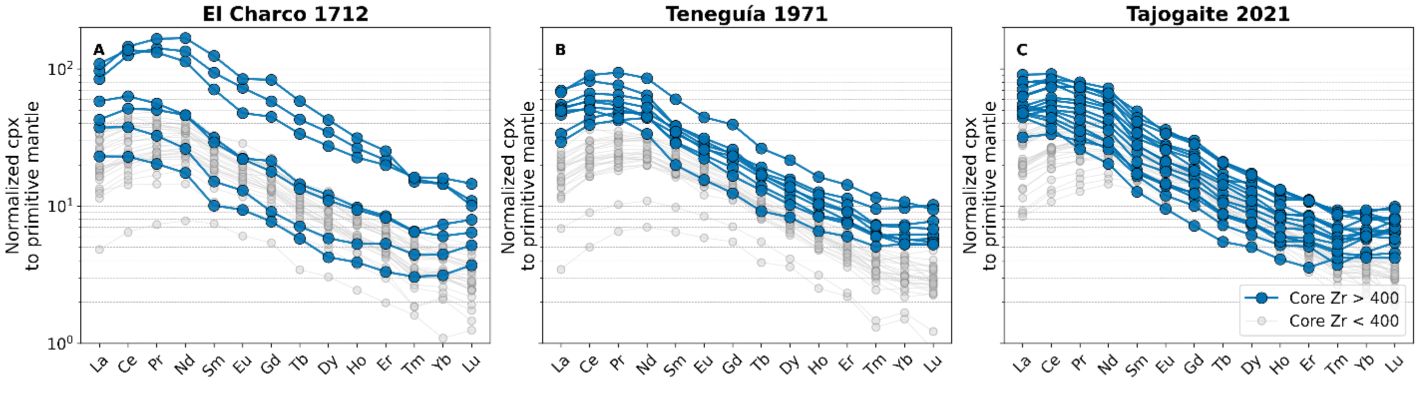

Fig. S15. Cpx core REE patterns. Trace element pattern of clinopyroxene cores, color-coded based on Zr concentrations, used as a proxy for magma evolution. Evolved core compositions (Zr>400 ppm), marked in blue, are the most fractionated and show a slight enrichment in heavy REE elements Tm, Yb and Lu compared to less evolved core compositions (Zr<400 ppm).

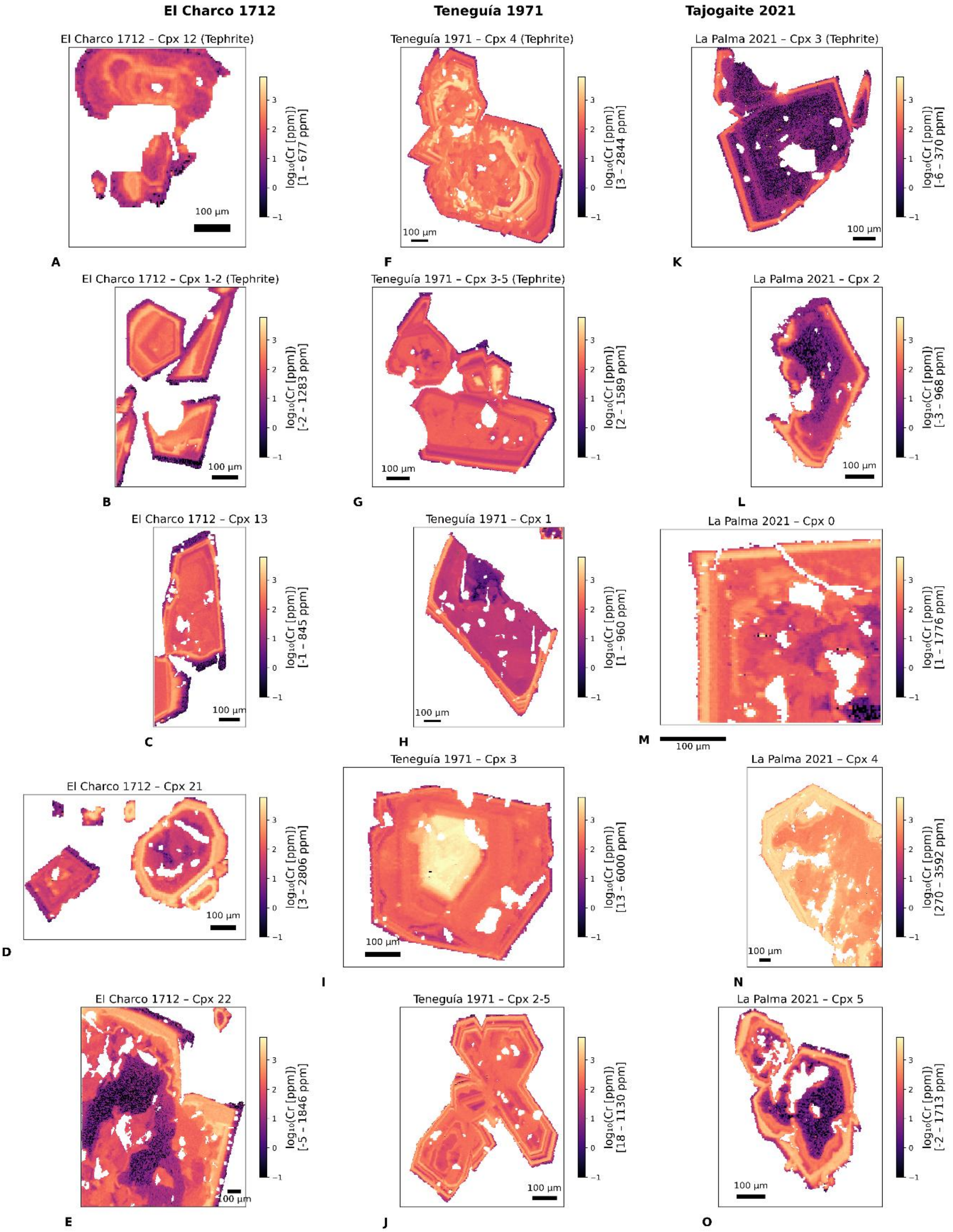

Fig. S16. Cr chemical maps. LA-ICP-MS maps of Cr in clinopyroxene from El Charco 1712, Teneguía 1971 and Tajogaite 2021. Maps are visualized using a logarithmic scale and scaled to the maximum common range observed across all maps (0.1–6000 ppm Cr; $\log_{10}$ = -1–3.8) to allow direct comparison of Cr variations among samples and eruptions.

8. Geochemistry of the matrix

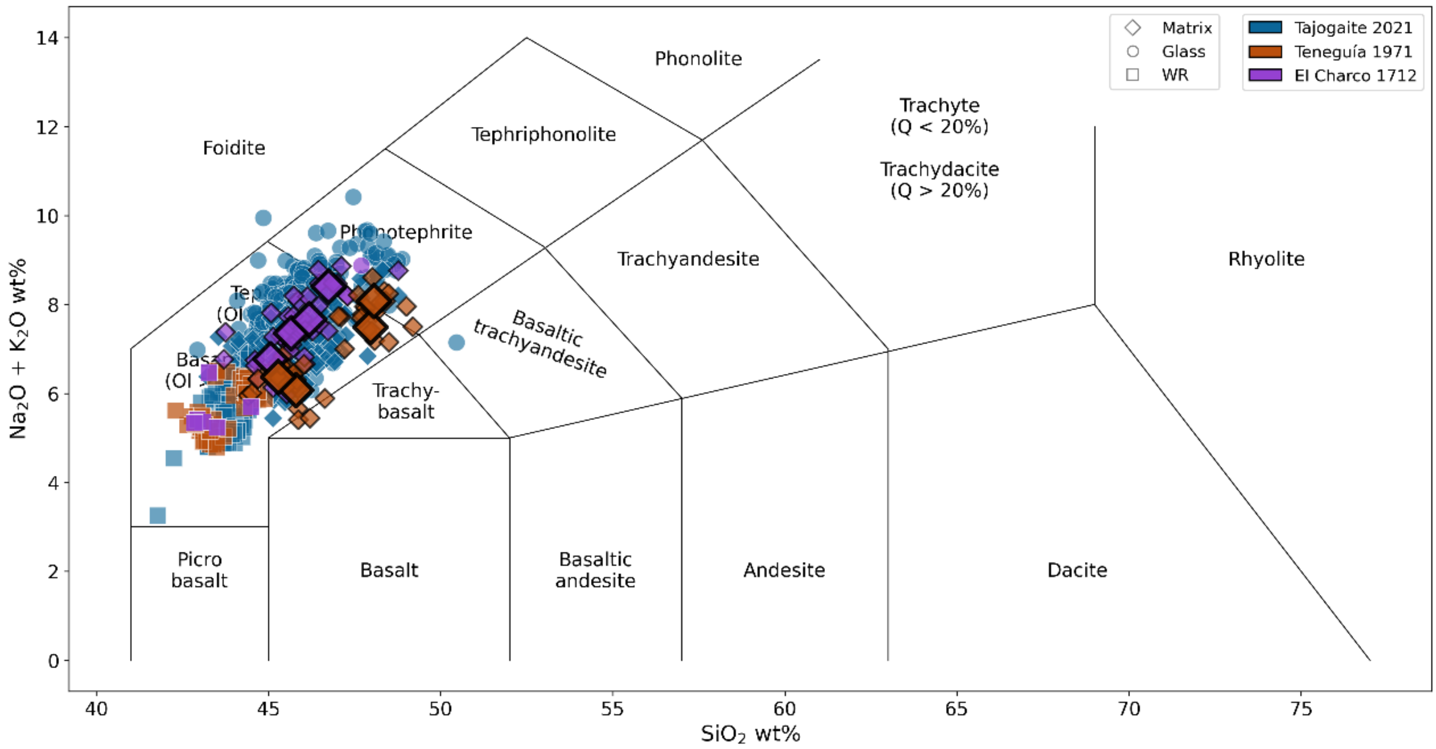

Fig. S17. TAS diagram. TAS diagram showing the matrix compositions studied in this work, compared with literature data. Large diamonds for Teneguía 1971 and El Charco 1712 represent the average matrix compositions based on 10 analyses from this study. Matrix data for Tajogaite 2021 are from Ubide et al. (2023). Whole-rock (WR) data for Tajogaite 2021 are from Day et al. (2022), Pankhurst et al. (2022) and Ubide et al. (2023). WR data for El Charco 1712 (Carracedo et al., 2001; Day et al., 2010; Hernandez-Pacheco and Valls, 1982; Turner et al., 2015) and Teneguía 1971 (Barker et al., 2015; Carracedo et al., 2001; Ibarrola, 1974; Lundstrom et al., 2003; Turner et al., 2015; Weis et al., 2015) were retrieved from the GEOROC database.

9. Clustering results

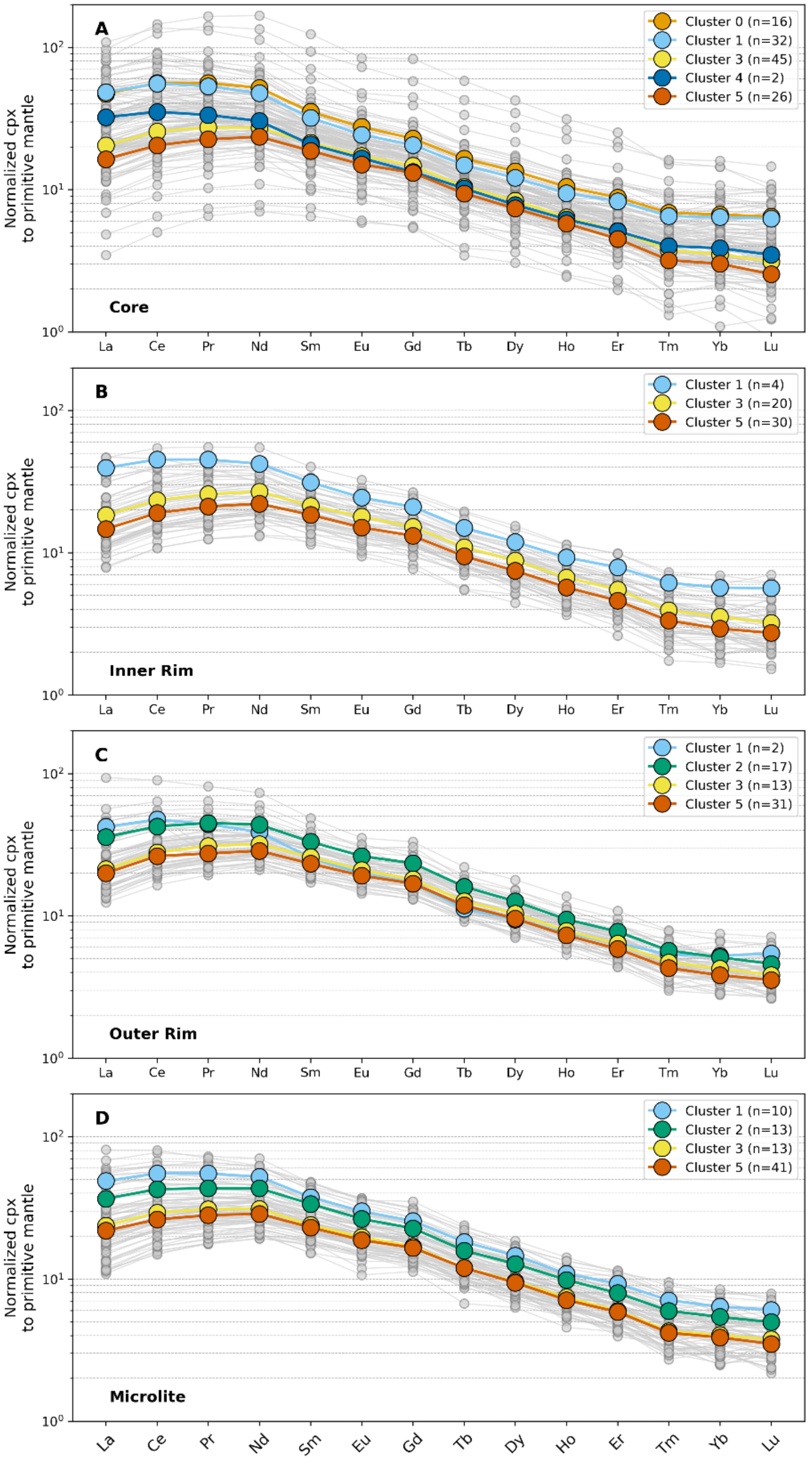

Fig. S18. Cluster-colored cpx REE patterns. Trace element patterns are color-coded based on clusters. Grey lines and points represent individual measurements, while colored lines show the average for each cluster group. Each panel corresponds to a specific textural position: (A) core (B) inner rim (C) outer rim and (D) microlite.

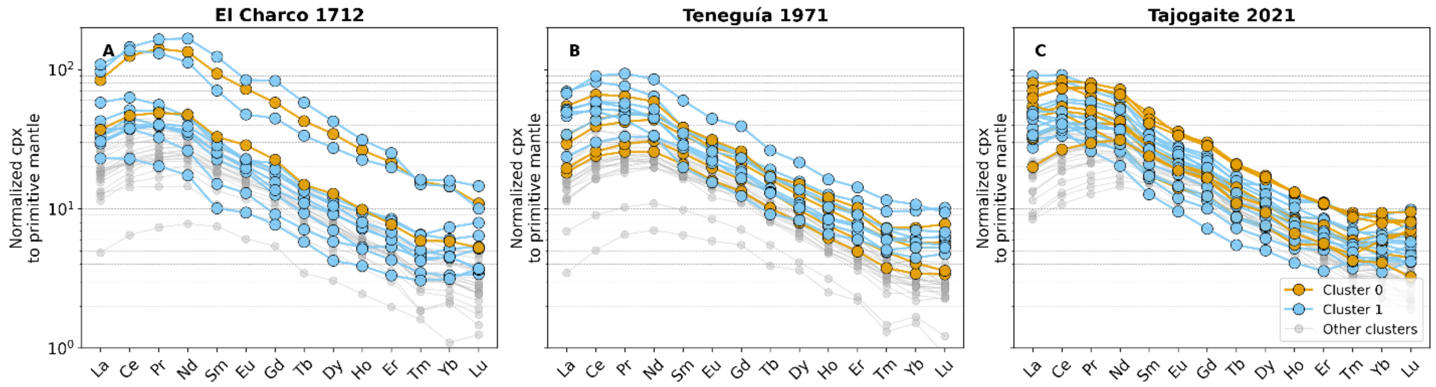

Fig. S19. Evolved cpx REE patterns. Trace element pattern of evolved clinopyroxene cores belonging to Cluster 0 and 1. These compositions are the most differentiated, with patterns showing an enrichment in heavy REE elements Tm, Yb and Lu, typical of phonolite-derived compositions. Grey lines represent patterns of clinopyroxenes belonging to Cluster 2, 3, 4 and 5.

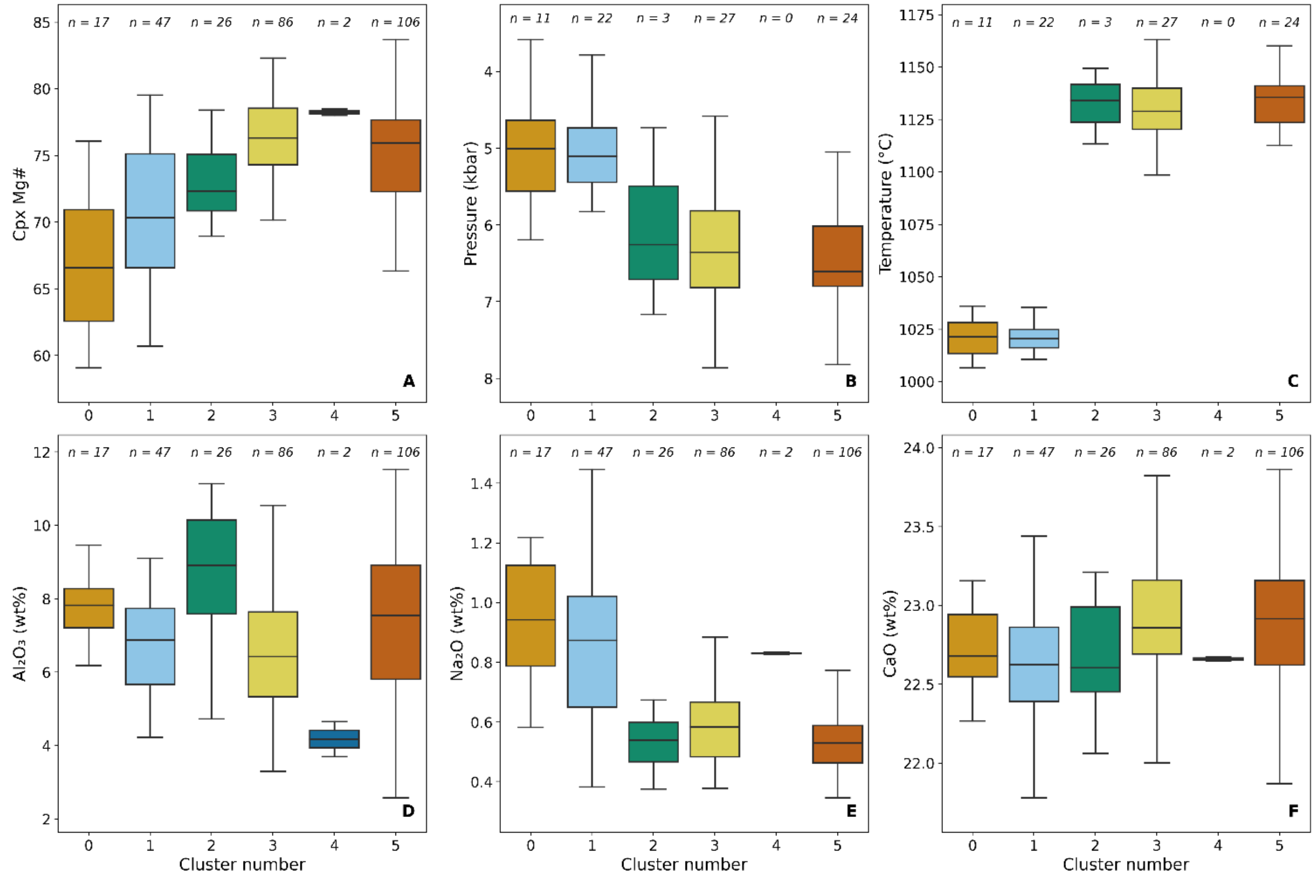

Fig. S20. Cluster-colored cpx composition, P and T. Box plots show the distribution of clinopyroxene (A) Mg# for each cluster. Panels (B) and (C) show clinopyroxene–melt equilibrium pressures and temperatures, respectively, for each cluster. Only data that passed the equilibrium criteria following the approach of MacDonald et al. (2023) are included, as described in the method section. (D-F) Distribution of Al_2O_3, Na_2O and CaO for each cluster. In this figure, only analyses with both EMPA and LA-ICP-MS single-spot data are plotted.

10. Equilibrium melt composition and trace elements modelling

We reconstructed the trace element melt composition in equilibrium with each measured clinopyroxene trace element composition to compare these with the trace element composition of the matrix, interpreted here as representative of the carrier melt, and to model fractional crystallization (FC).

Equilibrium melt compositions were calculated using partition coefficients (KDs) derived from multiple parametrizations published in Bédard (2014). Specifically, for each element, we applied several parameterizations calibrated for terrestrial systems (TE), mafic terrestrial systems (MTS), and low-pressure MTS as reported in Bédard (2014). The resulting KDs were averaged, and uncertainties were estimated based on the 1σ variability across parameterizations. Using these fixed KDs for each trace element, we reconstructed the equilibrium melt composition for each clinopyroxene, incorporating the uncertainty from the different parameterizations. Overall, the calculated KDs are of the same order of magnitude as those reported for alkali basalts in the GERM database.

Fractional crystallization was modeled starting from a primitive matrix composition, obtained by averaging the least differentiated matrix compositions with Zr concentrations between 300–330 ppm. The crystal assemblage was set following Ubide et al. (2023) to reflect the average assemblage observed in natural products (64% clinopyroxene, 28% olivine, 2% oxides, and 6% plagioclase). For clinopyroxenes, we used a fixed Kd for each trace element, calculated as the median of individual values estimated from the Bédard (2014) parameterizations described above. For the other mineral phases, Kd values were taken from the GERM database for alkali basalts. Specifically, Kds for amphibole and olivine are from Adam and Green (2006); for plagioclase, from Schnetzler and Philpotts (1970) and Villemant et al. (1981); and for oxides, from Elkins et al. (2008) and McKenzie and O'nions (1991).

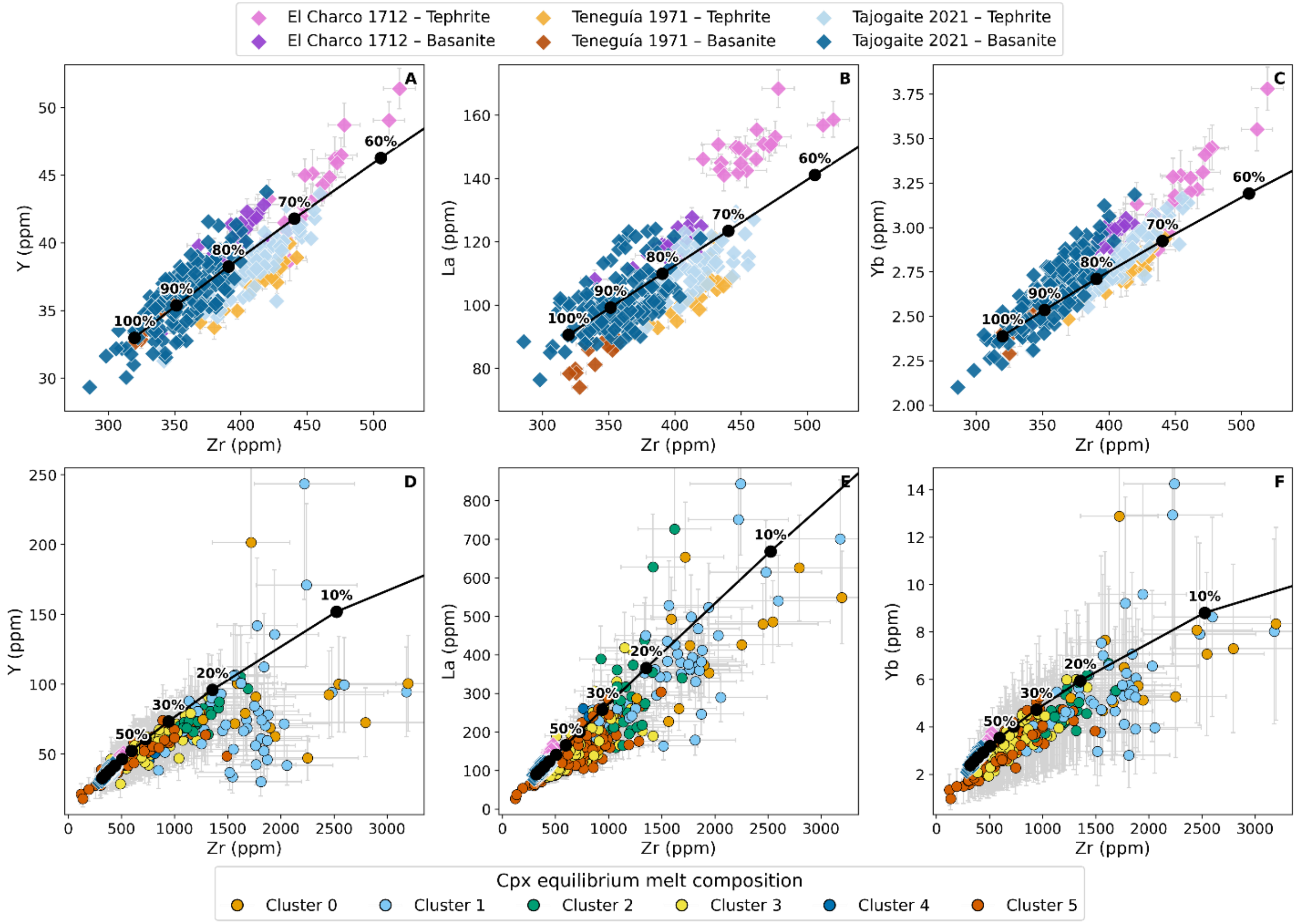

Fig. S21. Equilibrium melt composition and FC model. (A–C) Trace element composition of the matrix and FC results. Each black filled circle represents 10% increments of fractionation starting from 100% melt phase. Note that the tephrite compositions for each eruption can be reproduced by ~10% fractionation from a basanite composition of the same eruption. (D–F) Reconstructed clinopyroxene equilibrium melt compositions, colored according to clustering. The black line represents the FC model. Note that Clusters 0 and 1 compositions are consistent with 80–90% fractionation.

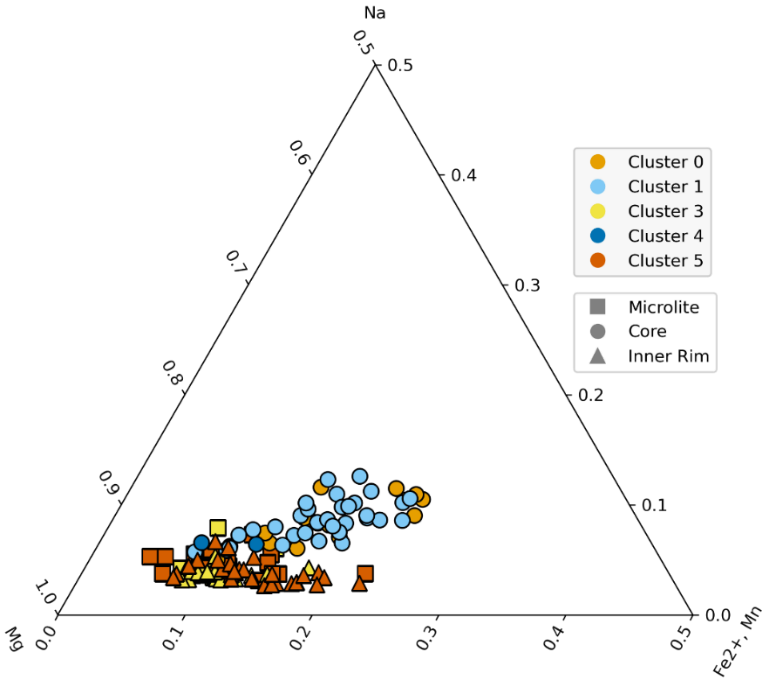

Fig. S22. Mg–Fe^{2+}(+Mn)–Na Cpx classification. Clinopyroxene compositions are plotted on the Mg–Fe^{2+}(+Mn)–Na atoms per formula unit diagram after Larsen (1976). We show Cluster 0 and 1 core compositions, Cluster 4 core compositions (n=2), and Cluster 3 and 5 inner rim and microlite compositions to compare evolutionary trends of the phonolite-derived (Clusters 0 and 1) and tephrite–basanite (Clusters 3 and 5) recharge compositions relative to Cluster 4. Notably, Clusters 0 and 1 cores define a distinct lineage from the Cluster 3 and 5 recharge compositions, while Cluster 4 lies at the beginning of the phonolite lineage, potentially representing a composition capable of evolving into phonolitic melts. Cluster 2 compositions are not included in this plot as they are related to magma ascent and surface cooling.

11. Clinopyroxene trace element maps

Fig. S23. LA-ICP-MS chemical maps. We present 15 figures of clinopyroxene trace element maps for Cr, Mn, Ni, Sc, Sr, Ti, V, and Zr. For each element and each sample, the optimal visualization method, either logarithmic scaling, histogram equalization (HE), or adaptive histogram equalization (AHE), was selected and is indicated at the top of each panel (Panels A–H). Note that colors are not comparable between images, as this approach is designed to enhance zoning contrast within each map. The quantitative range for each element (in ppm) is shown in the title of each color bar. In each figure, Panel I displays the BSE image of the mapped area. BSE images were acquired after crystal mapping and gentle repolishing, which may result in minor differences between the crystals shown in the trace element maps and those in the BSE image. The eruption, clinopyroxene name, and rock type (basanite or tephrite) are indicated at the top of each figure.

Teneguía 1971 – Cpx 4 (Tephrite)

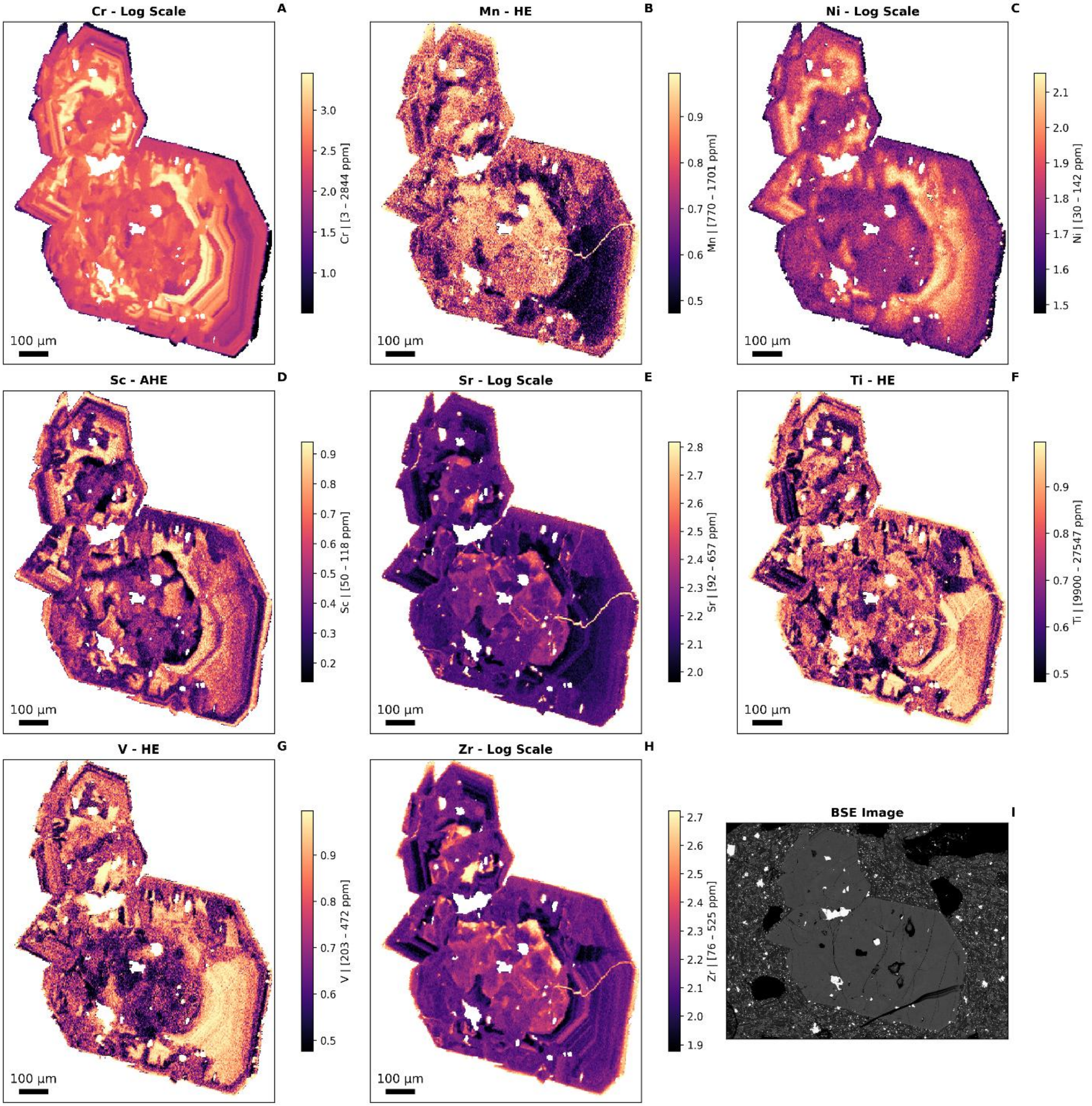

Teneguía 1971 – Cpx 3-5 (Tephrite)

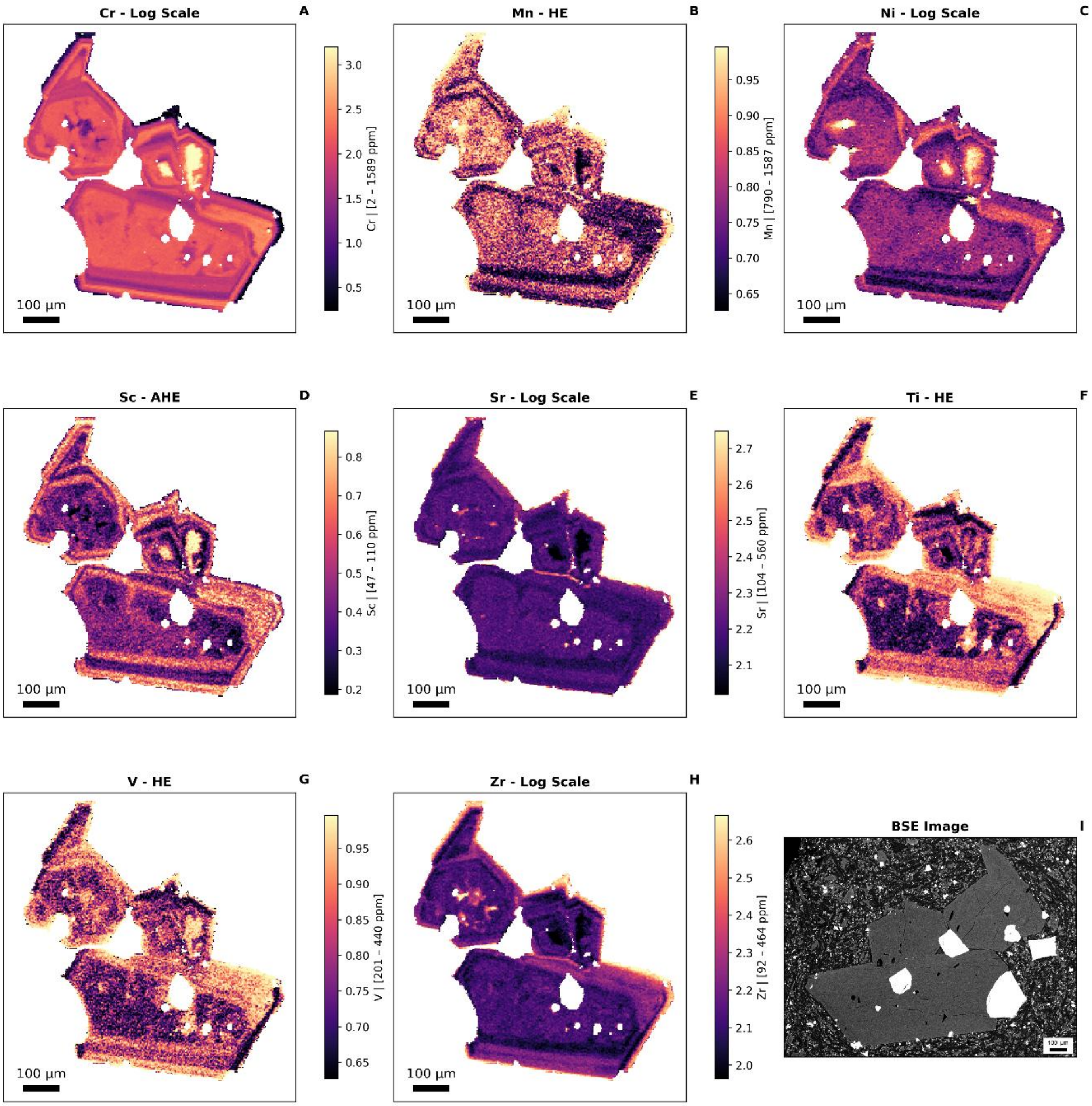

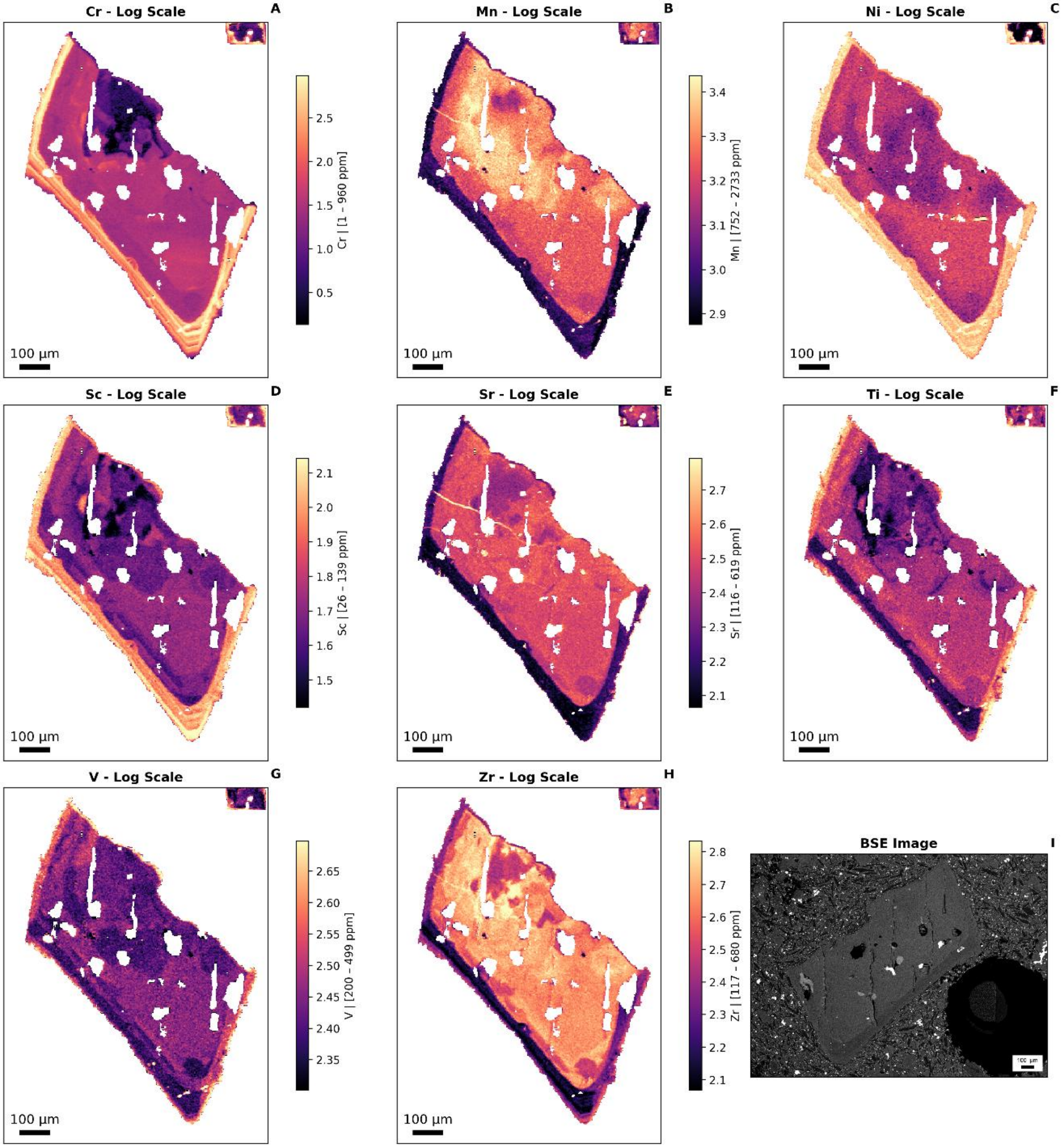

Teneguía 1971 – Cpx 1 (Basanite)

Teneguía 1971 – Cpx 3 (Basanite)

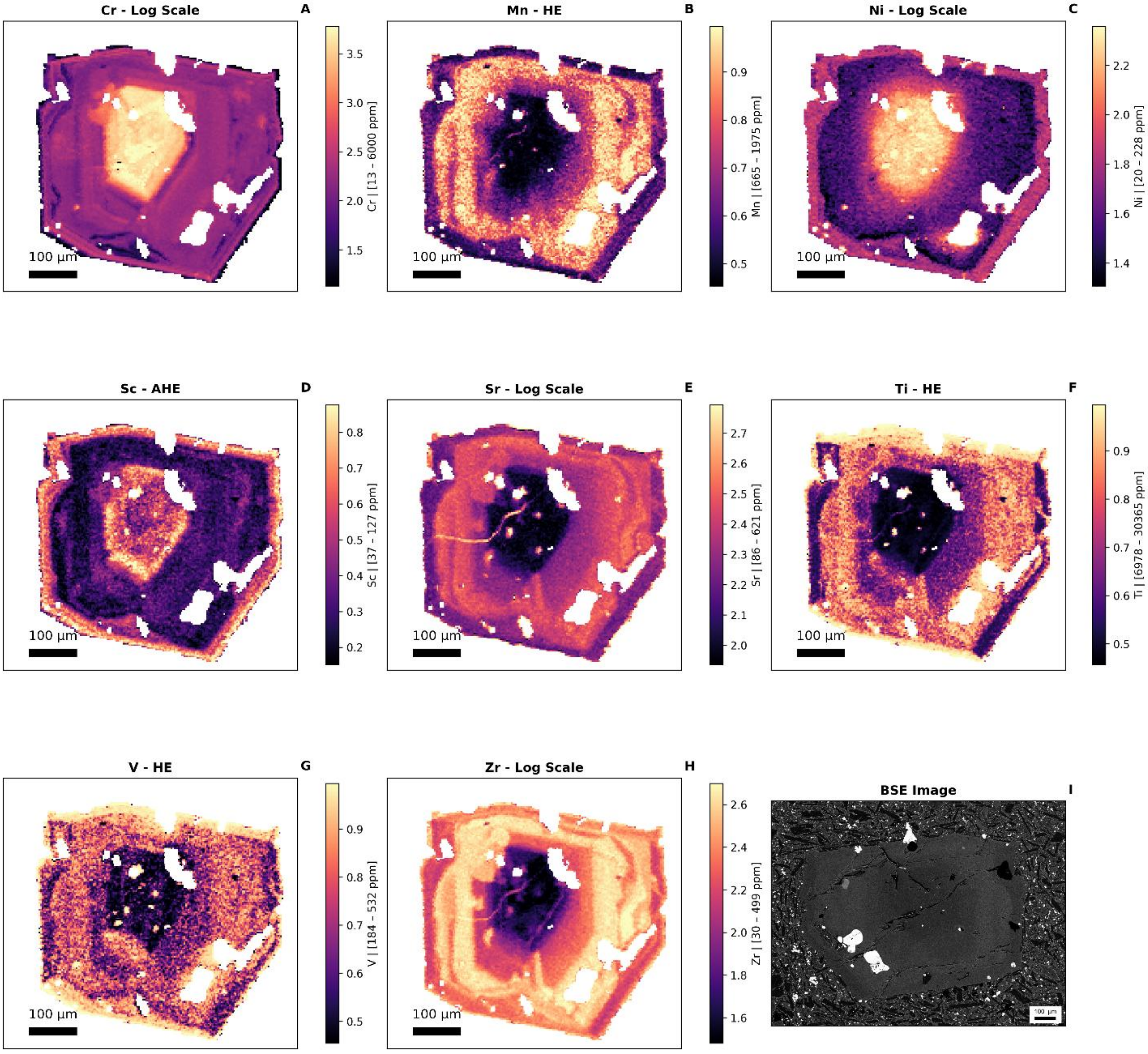

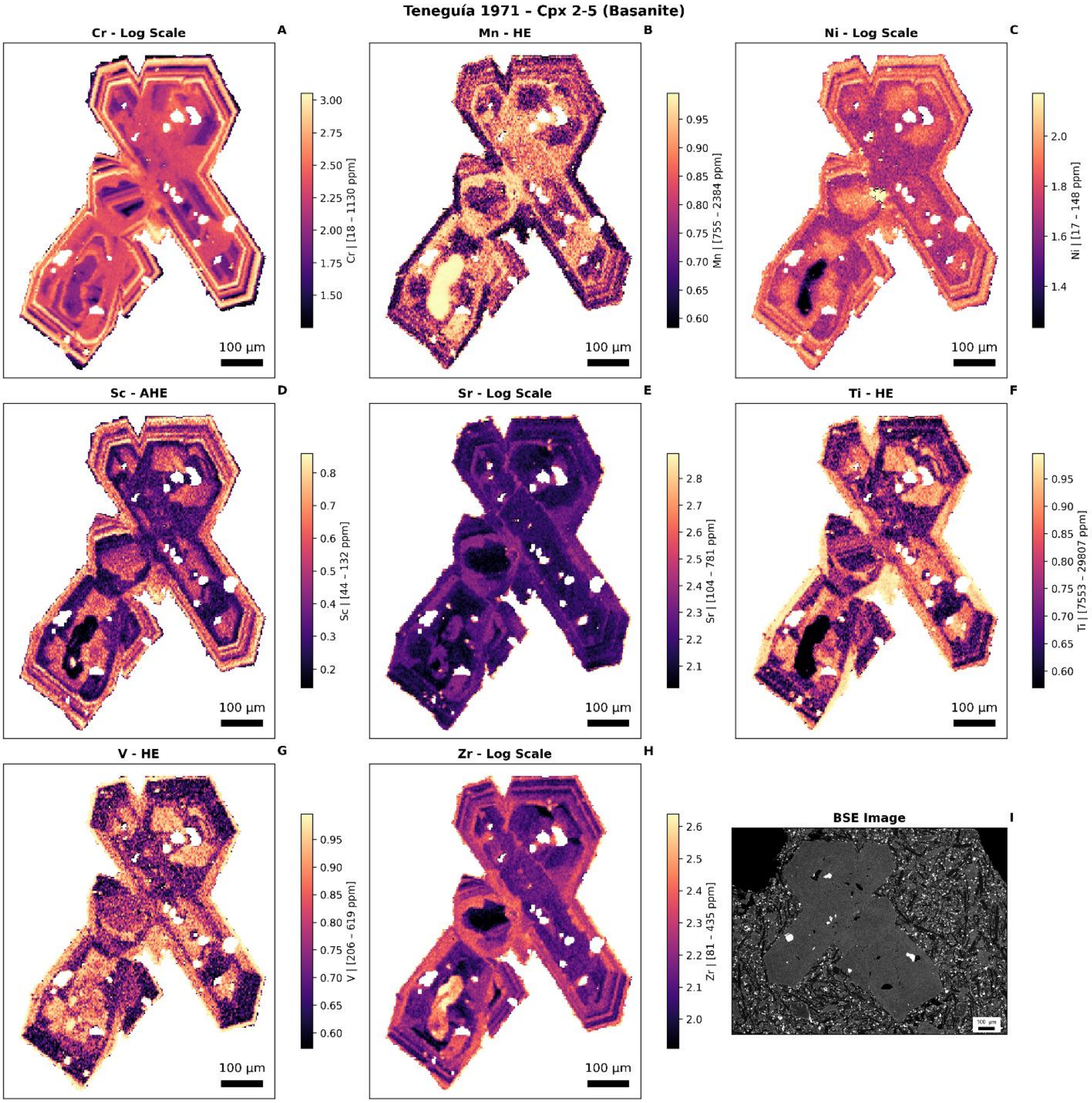
Teneguía 1971 – Cpx 2-5 (Basanite)
Cr - Log Scale
A
Cr | [18 – 1130 ppm]
3.00
2.75
2.50
2.25
2.00
1.75
1.50
100 µm
Mn - HE
B
Mn | [755 – 2384 ppm]
0.95
0.90
0.85
0.80
0.75
0.70
0.65
0.60
100 µm
Ni - Log Scale
C
Ni | [17 – 148 ppm]
2.0
1.8
1.6
1.4
100 µm
Sc - AHE
D
Sc | [44 – 132 ppm]
0.8
0.7
0.6
0.5
0.4
0.3
0.2
100 µm
Sr - Log Scale
E
Sr | [104 – 781 ppm]
2.8
2.7
2.6
2.5
2.4
2.3
2.2
2.1
100 µm
Ti - HE
F
Ti | [7553 – 29807 ppm]
0.95
0.90
0.85
0.80
0.75
0.70
0.65
0.60
100 µm
V - HE
G
V | [206 – 619 ppm]
0.95
0.90
0.85
0.80
0.75
0.70
0.65
0.60
100 µm
Zr - Log Scale
H
Zr | [81 – 435 ppm]
2.6
2.5
2.4
2.3
2.2
2.1
2.0
100 µm
BSE Image
I
100 µm

El Charco 1712 – Cpx 12 (Tephrite)

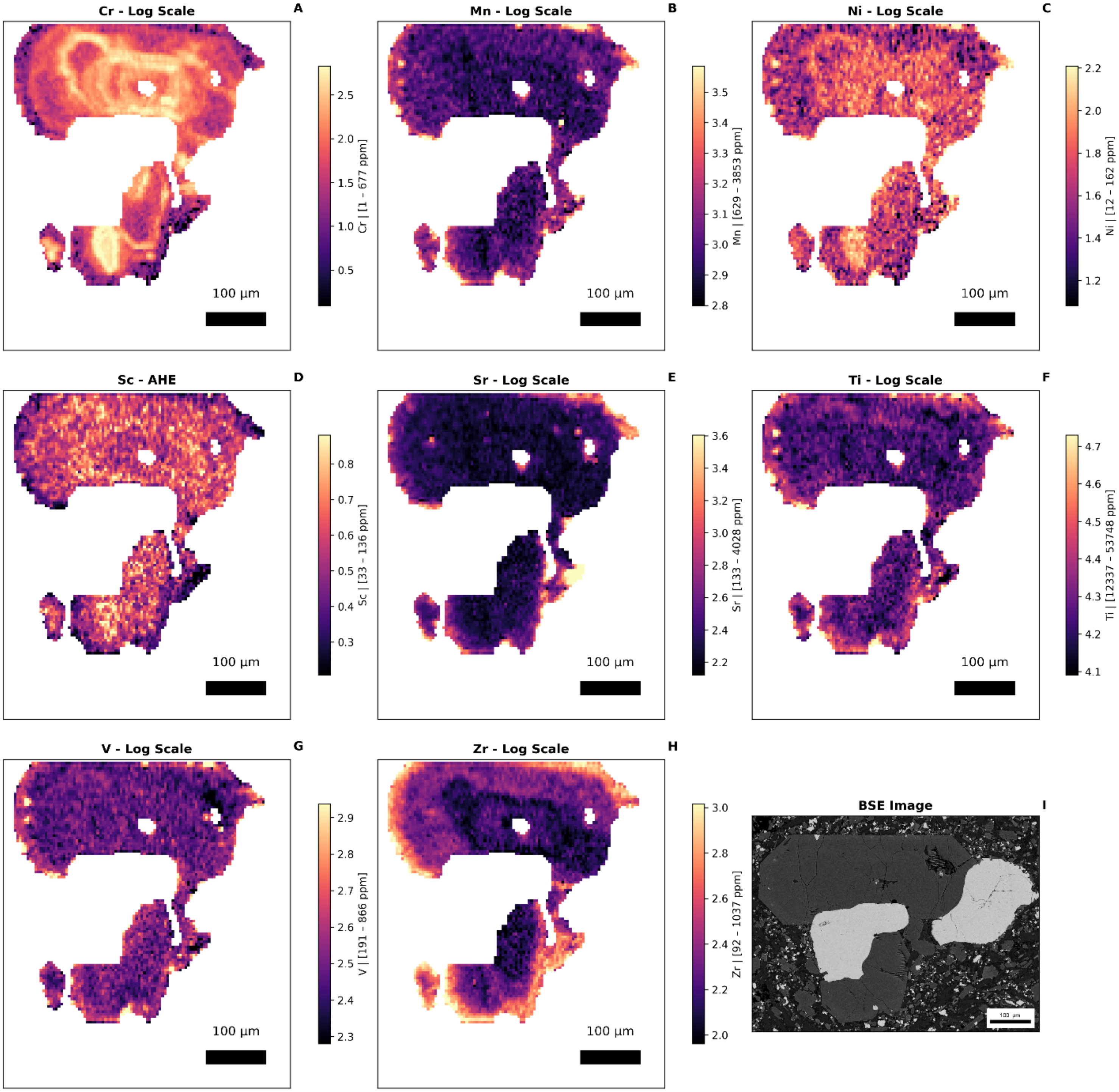

El Charco 1712 – Cpx 13 (Basanite)

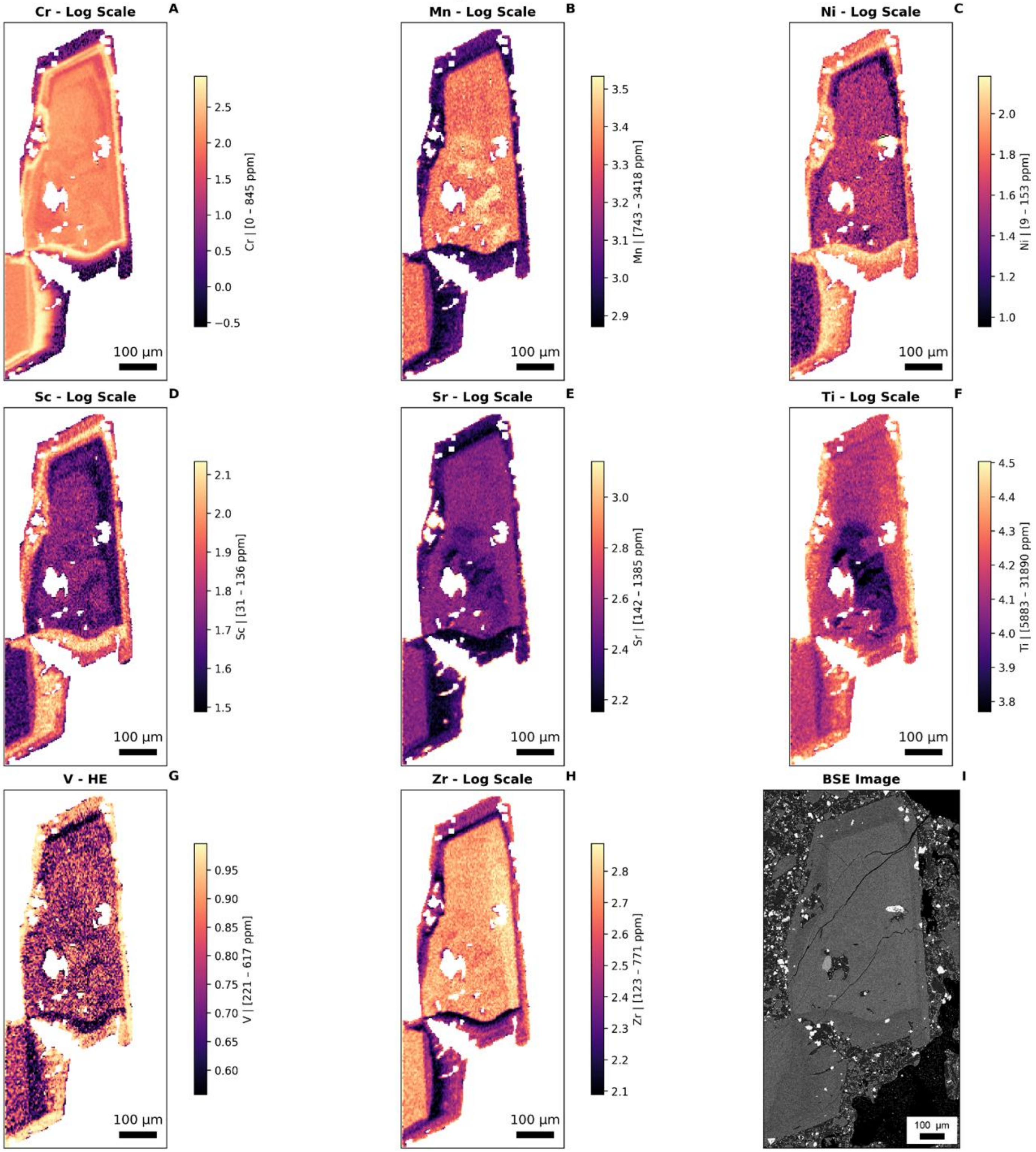

El Charco 1712 – Cpx 1-2 (Tephrite)

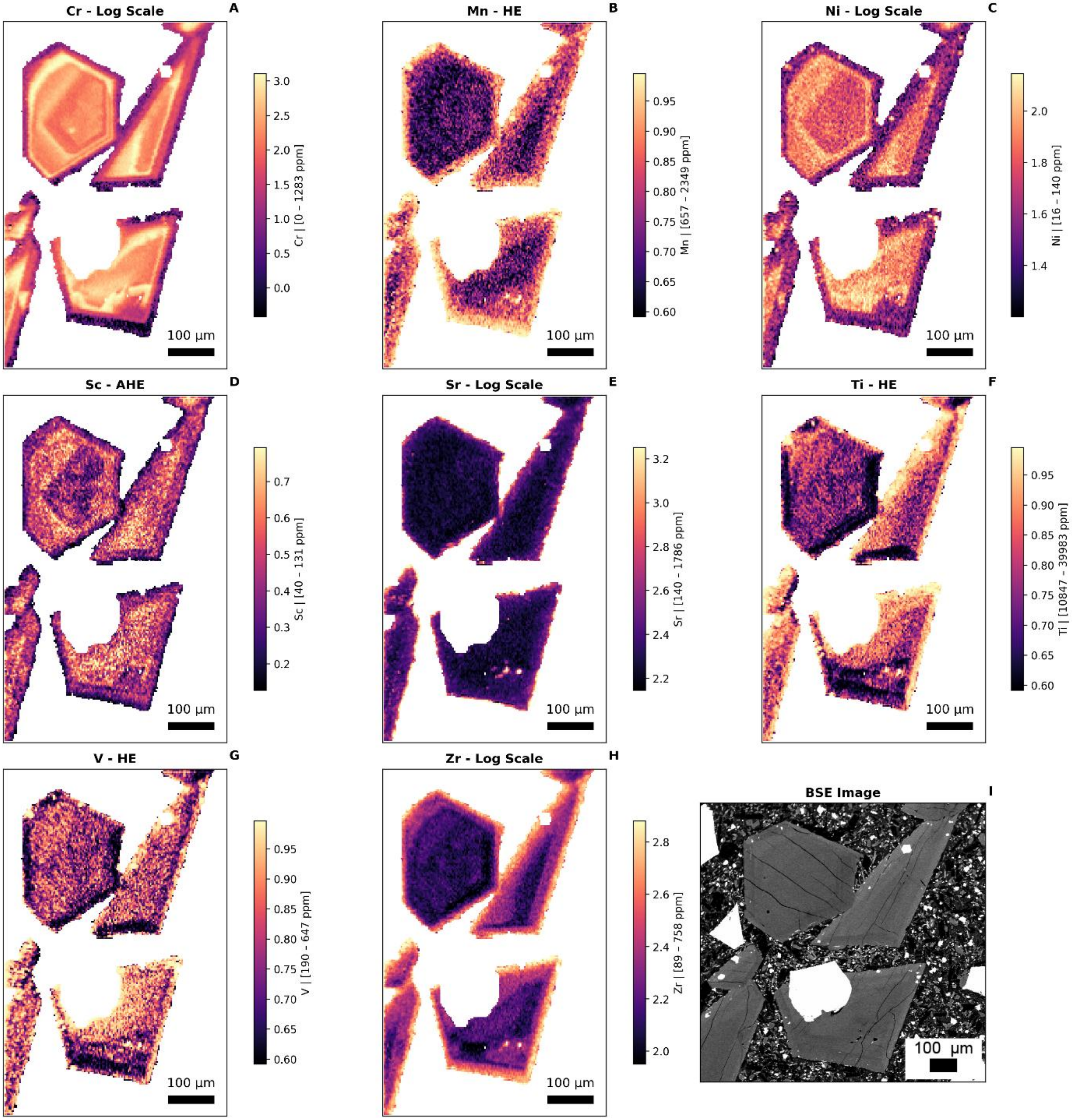

El Charco 1712 – Cpx 21 (Basanite)

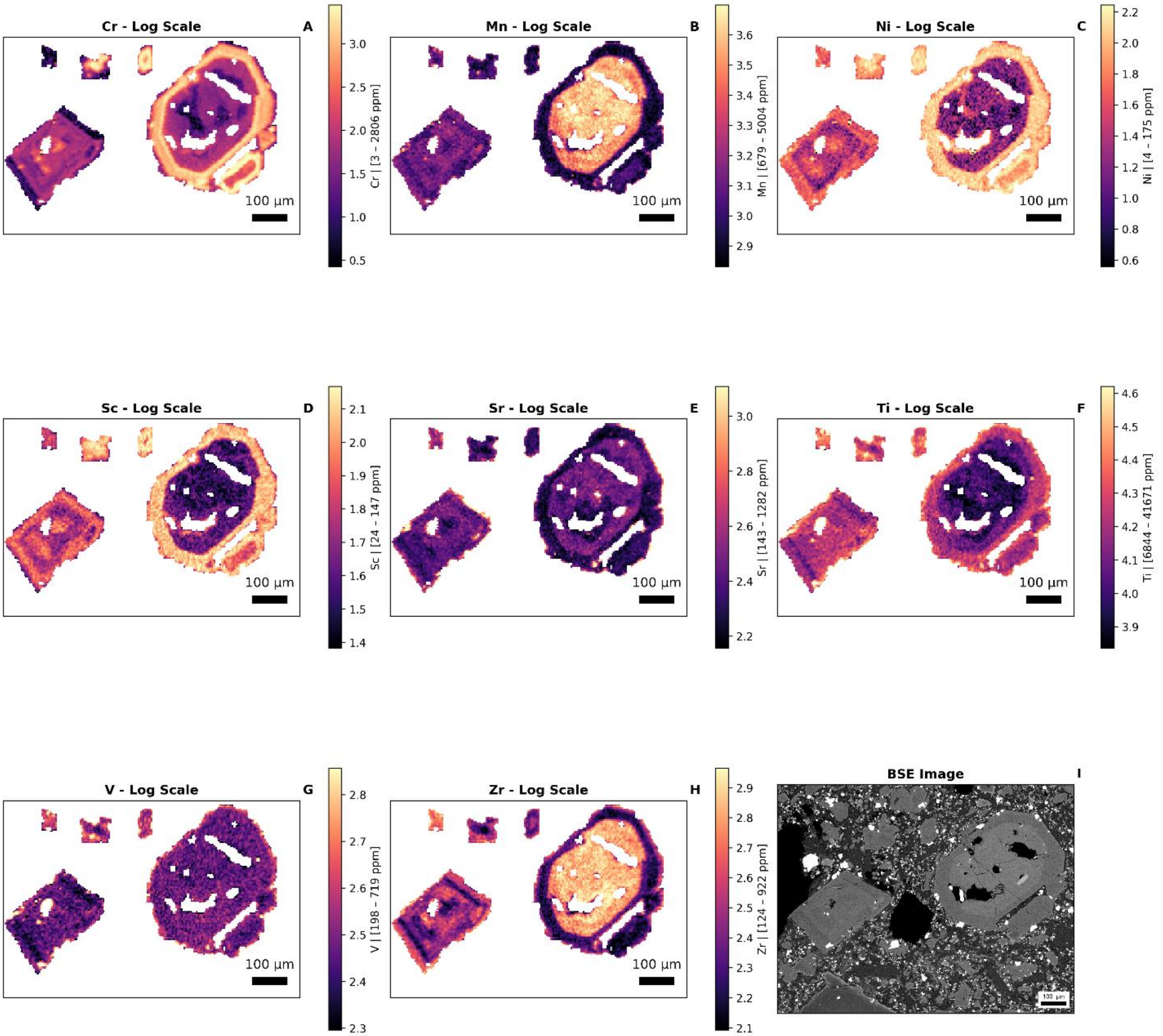

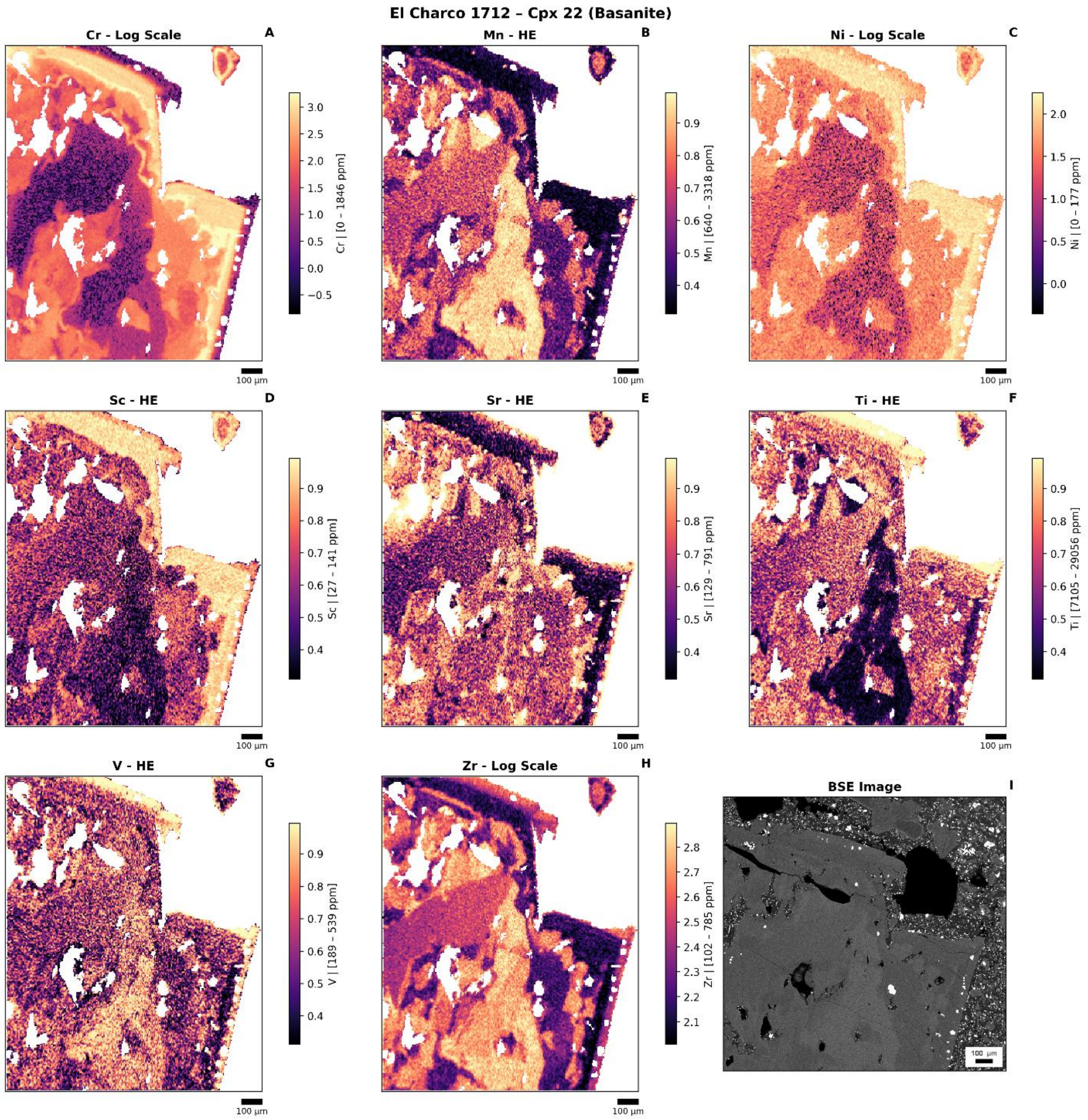
El Charco 1712 – Cpx 22 (Basanite)
Cr - Log Scale
A
Cr | [0 – 1846 ppm]
3.0
2.5
2.0
1.5
1.0
0.5
0.0
−0.5
100 µm
Mn - HE
B
Mn | [640 – 3318 ppm]
0.9
0.8
0.7
0.6
0.5
0.4
100 µm
Ni - Log Scale
C
Ni | [0 – 177 ppm]
2.0
1.5
1.0
0.5
0.0
100 µm
Sc - HE
D
Sc | [27 – 141 ppm]
0.9
0.8
0.7
0.6
0.5
0.4
100 µm
Sr - HE
E
Sr | [129 – 791 ppm]
0.9
0.8
0.7
0.6
0.5
0.4
100 µm
Ti - HE
F
Ti | [7105 – 29056 ppm]
0.9
0.8
0.7
0.6
0.5
0.4
100 µm
V - HE
G
V | [189 – 539 ppm]
0.9
0.8
0.7
0.6
0.5
0.4
100 µm
Zr - Log Scale
H
Zr | [102 – 785 ppm]
2.8
2.7
2.6
2.5
2.4
2.3
2.2
2.1
100 µm
BSE Image
I
100 µm

Tajogaite 2021 – Cpx 3 (Tephrite)

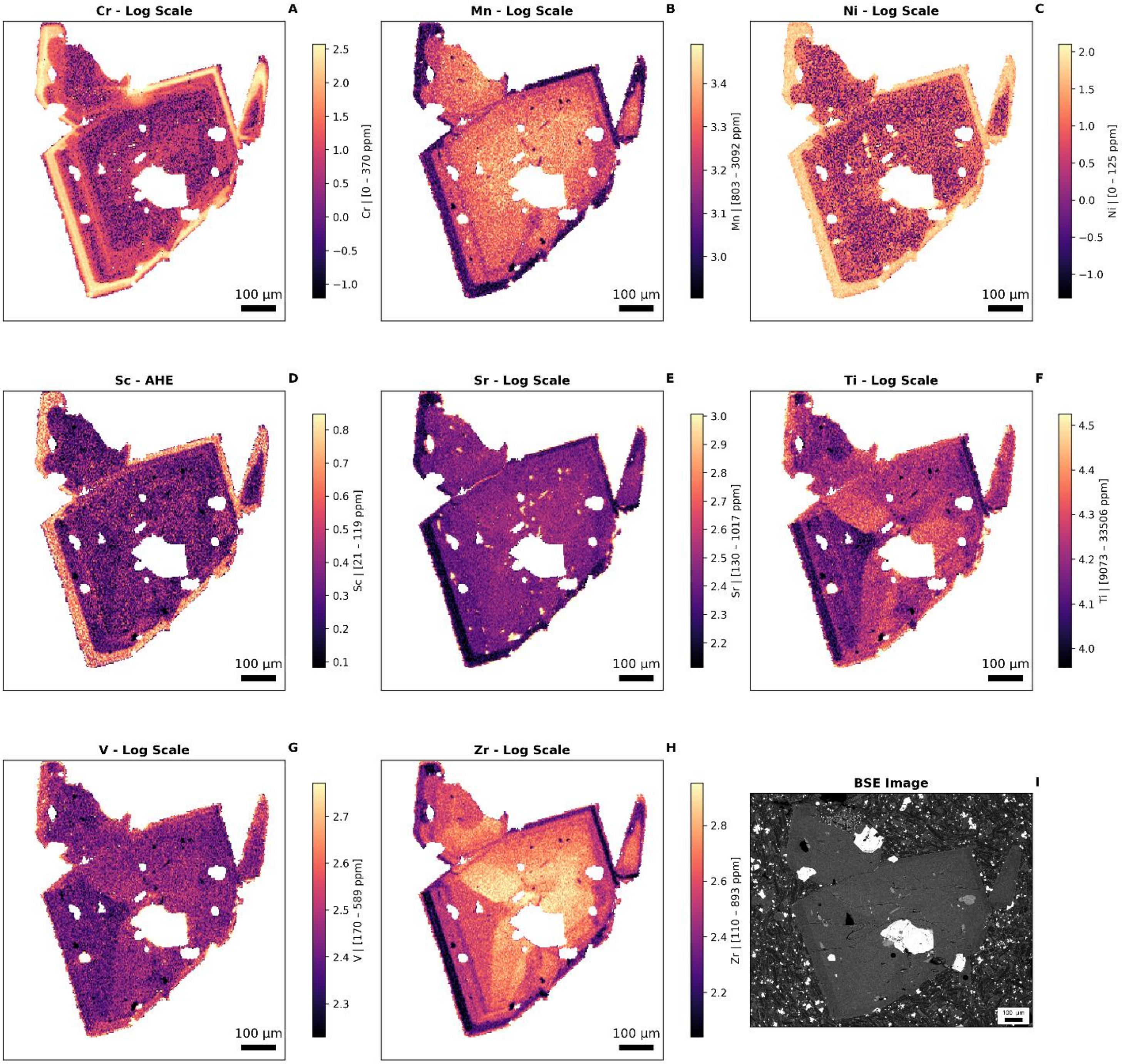

Tajogaite 2021 – Cpx 2 (Basanite)

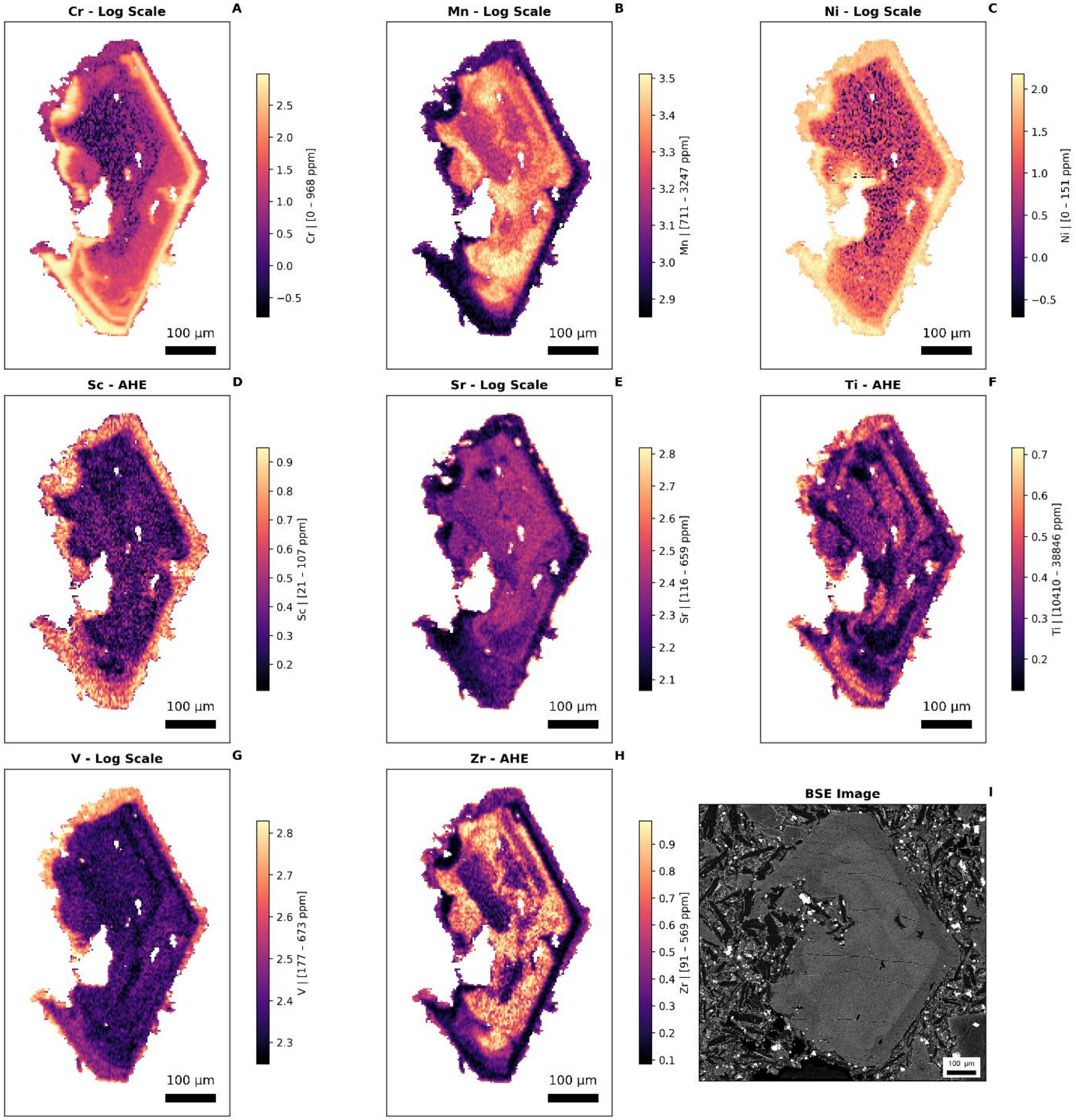

Tajogaite 2021 – Cpx 4 (Basanite)

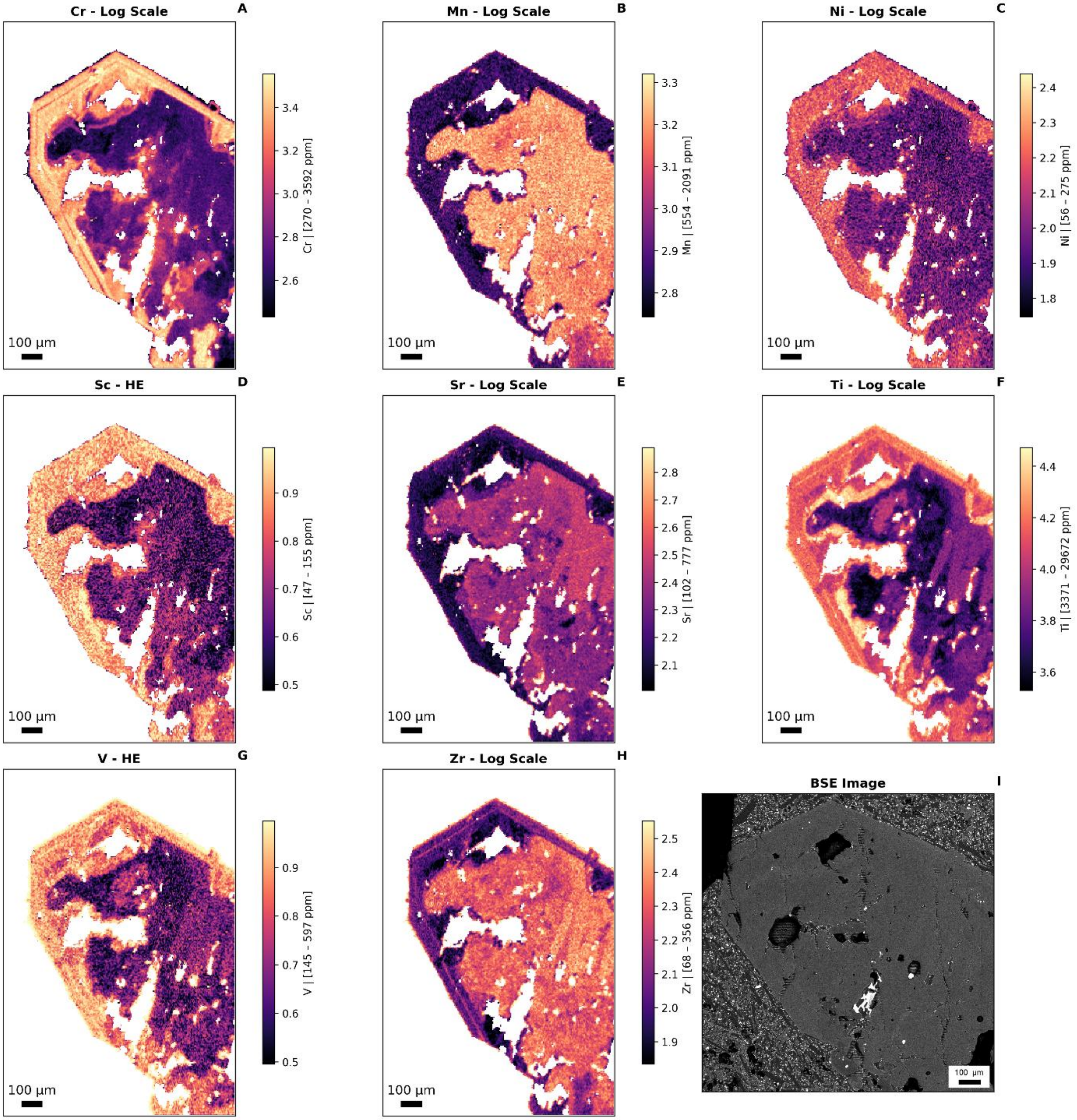

Tajogaite 2021 – Cpx 5 (Basanite)

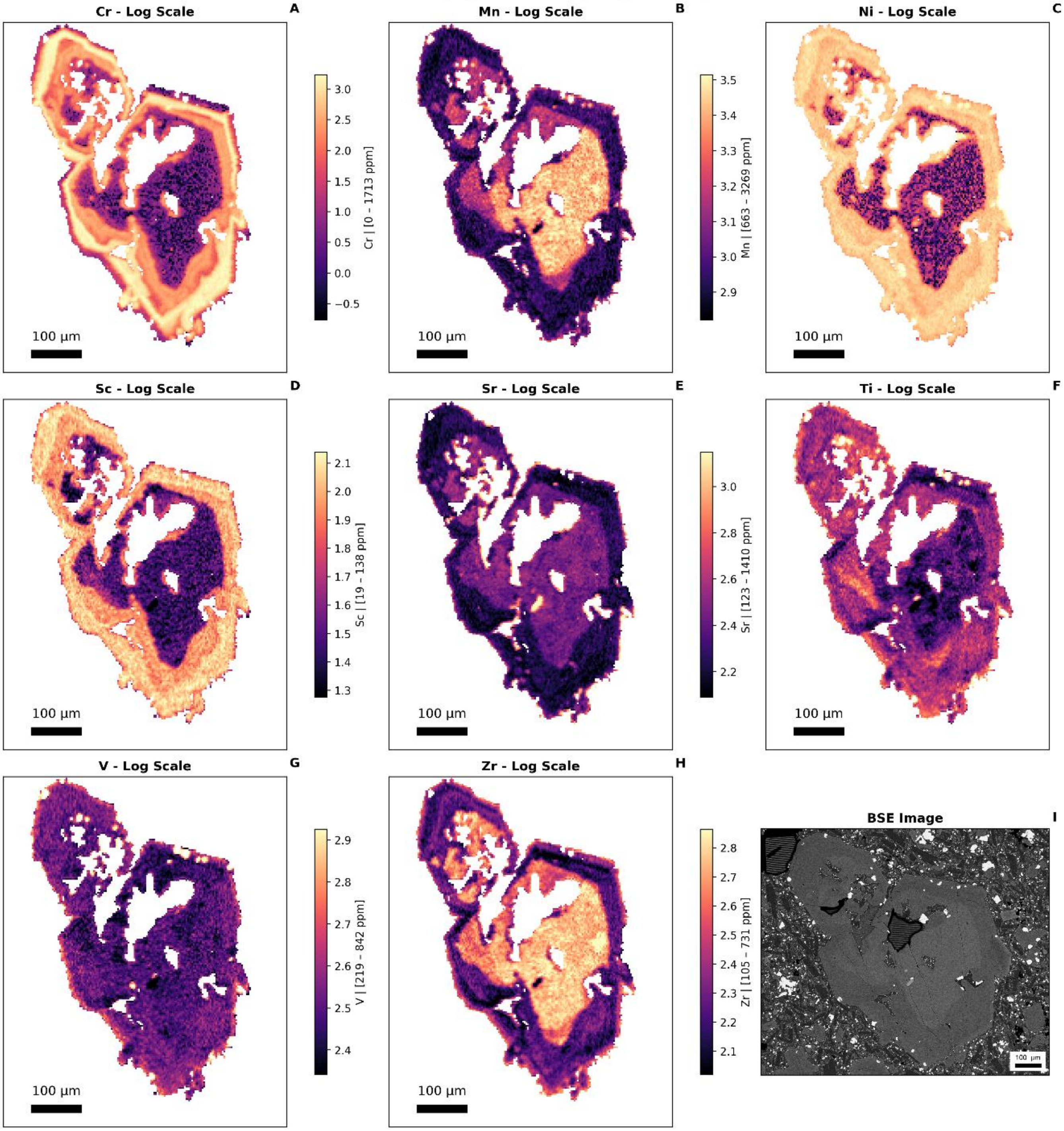

Tajogaite 2021 – Cpx 0 (Basanite)

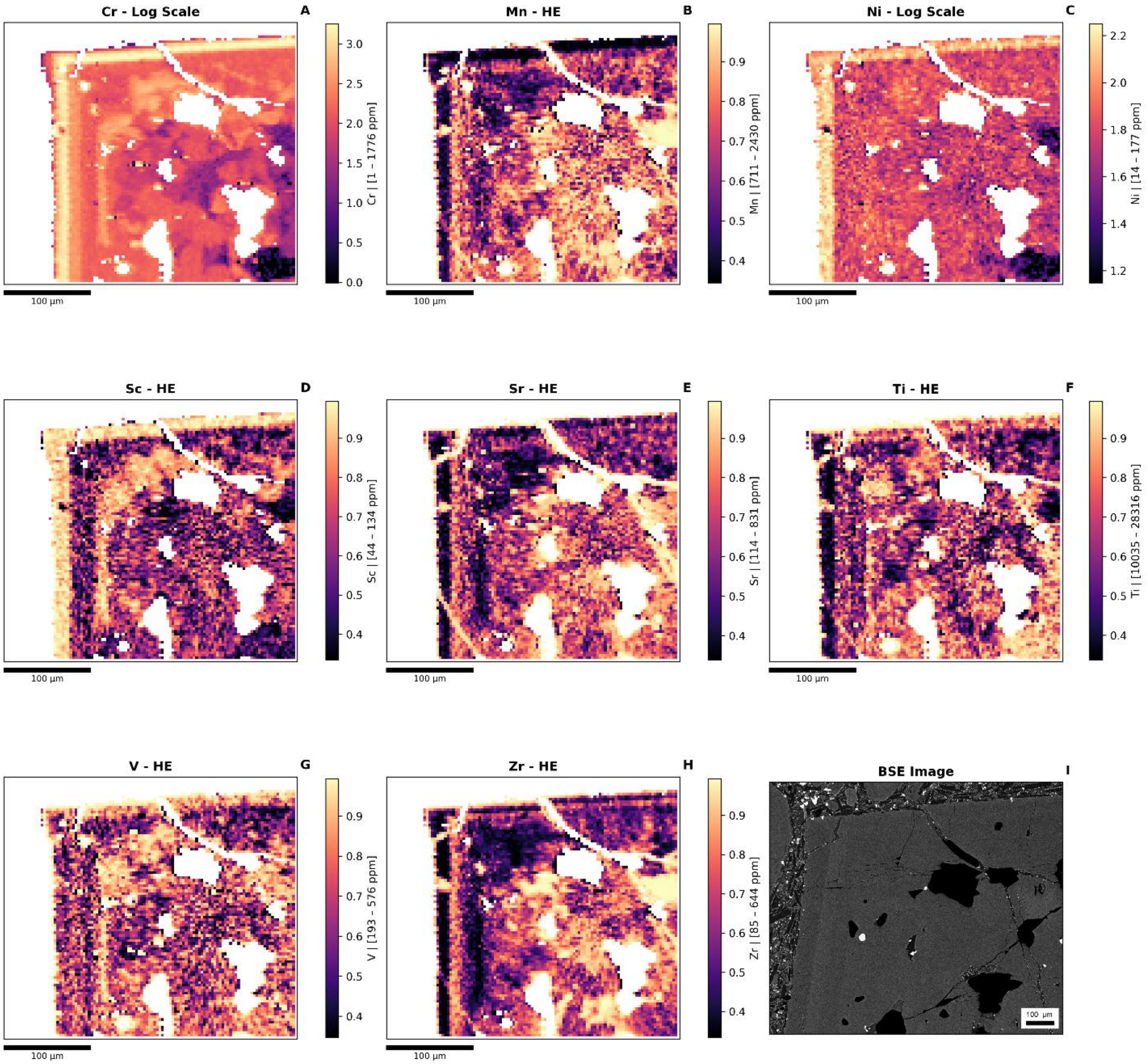

12. Supplementary references

Adam, J., Green, T., 2006. Trace element partitioning between mica-and amphibole-bearing garnet lherzolite and hydrous basanitic melt: 1. Experimental results and the investigation of controls on partitioning behaviour. Contributions to Mineralogy and Petrology 152, 1–17.

Afonso, A., Aparicio, A., Hernández-Pacheco, A., Badiola, E.R., 1974. Morphology evolution of Teneguía volcano area. Estudios Geológicos, Vol. Teneguía 19–26.

Ágreda-López, M., Musu, A., Jorgenson, C., Šala, M., Giordano, G., Caricchi, L., Stremtan, C., Petrelli, M., 2025. The crystal cargo provides a chronicle of pre-caldera dynamics in mafic volcanic systems: insights from Colli Albani. Bull Volcanol 87. https://doi.org/10.1007/s00445-025-01865-6

Andújar, J., Scaillet, B., Frascerra, D., Di Carlo, I., Casillas, R., Suárez, E.D., Domínguez-Cerdeña, I., Meletlidis, S., López, C., Slodczyk, A., Martí, J., Núñez-Guerrero, E., 2025. Evolution of the crustal reservoir feeding La Palma 2021 eruption. Insights from phase equilibrium experiments and petrologically derived time scales. Journal of Volcanology and Geothermal Research 463. https://doi.org/10.1016/j.jvolgeores.2025.108327

Anguita, F., Fernández, C., Márquez, Á., León, R., Casillas, R., 2025. The Canary hotspot revisited: Refutation of the Hawaii paradigm and an alternative, plate-based hypothesis. Earth Sci Rev. https://doi.org/10.1016/j.earscirev.2024.105038

Barker, A.K., Troll, V.R., Carracedo, J.C., Nicholls, P.A., 2015. The magma plumbing system for the 1971 Teneguía eruption on La Palma, Canary Islands. Contributions to Mineralogy and Petrology 170, 1–21. https://doi.org/10.1007/s00410-015-1207-7

Bonechi, B., Polacci, M., Arzilli, F., Romero, J.E., Fellowes, J., Burton, M., 2024. Magma residence time, ascent rate and eruptive style of the November ash-laden activity during the 2021 Tajogaite eruption (La Palma, Spain). Volcanica 7, 51–65. https://doi.org/10.30909/vol.07.01.5165

Carracedo, J.C., Badiola, E.R., Guillou, H., De La Nuez, J., Pérez-Torrado, F.J., 2001. Geology and volcanology of La Palma and El Hierro, Western Canaries. Estudios Geológicos 57, 175–273.

Carracedo, J.C., Troll, V.R., Day, J.M.D., Geiger, H., Aulinas, M., Soler, V., Deegan, F.M., Pérez-Torrado, F.J., Gisbert, G., Gazel, E., Rodríguez-González, A., Albert, H., 2022. The 2021 eruption of the Cumbre Vieja volcanic ridge on La Palma, Canary Islands. Geology Today 38, 94–107. https://doi.org/10.1111/gto.12388

Chamberlain, K.J., Pankhurst, M., Neave, D., Morgan, D., Barbee, O., Scarrow, J., Hickey, J., Broom-Fendley, S., Gardner, J., Rollinson, G., Walshaw, R., Stewart, A., Wieser, P., Coldwell, B., Martín-Lorenzo, A., Rodríguez, F., 2025. Crystal cargo perspectives on magma assembly and dynamics during the 2021 Tajogaite eruption, La Palma, Canary Islands. Volcanica 8, 399–425. https://doi.org/10.30909/vol/vujv5852

Chicharro Fermín, N., 2024. La erupción de El Charco de 1712, La Palma. Características petrológicas e implicaciones en la peligrosidad volcánica. Universidad Complutense de Madrid. https://doi.org/https://docta.ucm.es/entities/publication/b8280

D'Auria, L., Koulakov, I., Prudencio, J., Cabrera-Pérez, I., Ibáñez, J.M., Barrancos, J., García-Hernández, R., Martínez van Dorth, D., Padilla, G.D., Przeor, M., Ortega, V., Hernández, P., Peréz, N.M., 2022. Rapid magma ascent beneath La Palma revealed by seismic tomography. Sci Rep 12. https://doi.org/10.1038/s41598-022-21818-9

Day, J.M.D., Pearson, D.G., Macpherson, C.G., Lowry, D., Carracedo, J.C., 2010. Evidence for distinct proportions of subducted oceanic crust and lithosphere in HIMU-type mantle beneath El Hierro and La Palma, Canary Islands. Geochim Cosmochim Acta 74, 6565–6589. https://doi.org/10.1016/j.gca.2010.08.021

Day, J.M.D., Troll, V.R., Aulinas, M., Deegan, F.M., Geiger, H., Carracedo, J.C., Pinto, G.G., Pérez-Torrado, F.J., 2022. Mantle source characteristics and magmatic processes during the 2021 La Palma eruption. Earth Planet Sci Lett 597. https://doi.org/10.1016/j.epsl.2022.117793

Dayton, K., Gazel, E., Wieser, P., Troll, V.R., Carracedo, J.C., Madrid, H. La, Roman, D.C., Ward, J., Aulinas, M., Geiger, H., Deegan, F.M., Gisbert, G., Pérez-Torrado, F.J., 2023. Deep magma storage during the 2021 La Palma eruption. Sci Adv 9, 1–8. https://doi.org/10.1126/sciadv.ade7641

Elkins, L.J., Gaetani, G.A., Sims, K.W.W., 2008. Partitioning of U and Th during garnet pyroxenite partial melting: Constraints on the source of alkaline ocean island basalts. Earth Planet Sci Lett 265, 270–286.

Fabbrizio, A., Bamber, E.C., Michailidou, E., Romero, J.E., Arzilli, F., Bonechi, B., Polacci, M., Burton, M., 2023. Phase equilibrium experiments and thermodynamic simulations to constrain the pre-eruptive conditions of the 2021 Tajogaite eruption (Cumbre Vieja volcano, La Palma, Canary Islands). Journal of Volcanology and Geothermal Research 442. https://doi.org/10.1016/j.jvolgeores.2023.107901

Fernández, J., Escayo, J., Hu, Z., Camacho, A.G., Samsonov, S. V., Prieto, J.F., Tiampo, K.F., Palano, M., Mallorquí, J.J., Ancochea, E., 2021. Detection of volcanic unrest onset in La Palma, Canary Islands, evolution and implications. Sci Rep 11. https://doi.org/10.1038/s41598-021-82292-3

González-García, D., Boulesteix, T., Klügel, A., Holtz, F., 2023. Bubble-enhanced basanite–tephrite mixing in the early stages of the Cumbre Vieja 2021 eruption, La Palma, Canary Islands. Sci Rep 13. https://doi.org/10.1038/s41598-023-41595-3

Hernandez-Pacheco, A., Valls, M.C., 1984. The historic eruptions of La Palma Island (Canaries). Arquipélago. Série Ciências da Natureza 83–94.

Hernandez-Pacheco, A., Valls, M.C., 1982. The historic eruptions of La Palma Island (Canaries). Arquipélago. Série Ciências da Natureza.

Ibarrola, E., 1974. Temporal modification of the basaltic materials from the 1971 eruption of the Teneguía volcano (La Palma, Canary Islands). Estudios Geológicos 49–58.

Jegal, Y., Ubide, T., Huertas, M.J., Herrera, R., Márquez, Á., Ancochea, E., Coello-Bravo, J.J., 2025. Plagioclase antecrysts record syn-eruptive incorporation of evolved mush during the 2021 Tajogaite eruption (La Palma, Spain). Contributions to Mineralogy and Petrology 180. https://doi.org/10.1007/s00410-025-02241-5

Klügel, A., Albers, E., Hansteen, T.H., 2022. Mantle and Crustal Xenoliths in a Tephriphonolite From La Palma (Canary Islands): Implications for Phonolite Formation at Oceanic Island Volcanoes. Front Earth Sci (Lausanne) 10. https://doi.org/10.3389/feart.2022.761902

Klügel, A., Hansteen, T.H., Galipp, K., 2005. Magma storage and underplating beneath Cumbre Vieja volcano, La Palma (Canary Islands). Earth Planet Sci Lett 236, 211–226. https://doi.org/10.1016/j.epsl.2005.04.006

Klugel, A., Schmincke, H.-U., White, J.D.L., Hoernle, K.A., 1999. Chronology and volcanology of the 1949 multi-vent rift-zone ž / eruption on La Palma Canary Islands, Journal of Volcanology and Geothermal Research.

Larsen, M.L., 1976. Clinopyroxenes and Coexisting Mafic Minerals from the Alkaline Dimaussaq Intrusion, South Greenland 17, 258–290.

Longpré, M.A., Felpeto, A., 2021. Historical volcanism in the Canary Islands; part 1: A review of precursory and eruptive activity, eruption parameter estimates, and implications for hazard assessment. Journal of Volcanology and Geothermal Research 419. https://doi.org/10.1016/j.jvolgeores.2021.107363

Longpré, M.A., Tramontano, S., Pankhurst, M.J., Roman, D.C., Reiss, M.C., Cortese, F., James, M.R., Spina, L., Rodríguez, F., Coldwell, B., Martín-Lorenzo, A., Barbee, O., D'Auria, L., Chamberlain, K.J., Scarrow, J.H., 2025. Shifting melt composition linked to volcanic tremor at Cumbre Vieja volcano. Nat Geosci. https://doi.org/10.1038/s41561-024-01623-x

Lundstrom, C.C., Hoernle, K., Gill, J., 2003. U-series disequilibria in volcanic rocks from the Canary Islands: Plume versus lithospheric melting. Geochim Cosmochim Acta 67, 4153–4177. https://doi.org/10.1016/S0016-7037(03)00308-9

MacDonald, A., Ubide, T., Mollo, S., Pontesilli, A., Masotta, M., 2023. The Influence of Undercooling and Sector Zoning on Clinopyroxene-Melt Equilibrium and Thermobarometry. Journal of Petrology 64, 1–18. https://doi.org/10.1093/petrology/egad074

Masotta, M., Mollo, S., Freda, C., Gaeta, M., Moore, G., 2013. Clinopyroxene-liquid thermometers and barometers specific to alkaline differentiated magmas. Contributions to Mineralogy and Petrology 166, 1545–1561. https://doi.org/10.1007/s00410-013-0927-9

McKenzie, D.A.N., O'nions, R.K., 1991. Partial melt distributions from inversion of rare earth element concentrations. Journal of petrology 32, 1021–1091.

Mollo, S., Blundy, J., Scarlato, P., De Cristofaro, S.P., Tecchiato, V., Di Stefano, F., Vetere, F., Holtz, F., Bachmann, O., 2018. An integrated P-T-H2O-lattice strain model to quantify the role of clinopyroxene fractionation on REE+Y and HFSE patterns of mafic alkaline magmas: Application to eruptions at Mt. Etna. Earth Sci Rev. https://doi.org/10.1016/j.earscirev.2018.05.014

Neave, D.A., Bali, E., Guðfinnsson, G.H., Halldórsson, S.A., Kahl, M., Schmidt, A.S., Holtz, F., 2019. Clinopyroxene-Liquid Equilibria and Geothermobarometry in Natural and Experimental Tholeiites: The 2014-2015 Holuhraun Eruption, Iceland. Journal of Petrology 60, 1653–1680. https://doi.org/10.1093/petrology/egz042

Neave, D.A., Putirka, K.D., 2017. A new clinopyroxene-liquid barometer , and implications for magma storage pressures under Icelandic rift zones. American Mineralogist 102, 777–794. https://doi.org/http://dx.doi.org/10.2138/am-2017-5968

Pankhurst, M.J., Scarrow, J.H., Barbee, O.A., Hickey, J., Coldwell, B.C., Rollinson, G.K., Rodríguez-Losada, J.A., Martín-Lorenzo, A., Rodríguez, F., Hernández, W., Calvo Fernández, D., Hernández, P.A., Pérez, N.M., Sánchez, F., 2022. Rapid response petrology for the opening eruptive phase of the 2021 Cumbre Vieja eruption, La Palma, Canary Islands. Volcanica.

Paton, C., Hellstrom, J., Paul, B., Woodhead, J., Hergt, J., 2011. Iolite: Freeware for the visualisation and processing of mass spectrometric data. J Anal At Spectrom 26, 2508–2518.

Petrelli, M., Morgavi, D., Vetere, F., Perugini, D., 2016. Elemental imaging and petro-volcanological applications of an improved Laser Ablation Inductively Coupled Quadrupole Plasma Mass Spectrometry. Periodico di Mineralogia. https://doi.org/10.2451/2015PM0465

Putirka, K.D., 2008. Thermometers and barometers for volcanic systems. Rev Mineral Geochem 69, 61–120. https://doi.org/10.2138/rmg.2008.69.3

Putirka, K.D., Mikaelian, H., Ryerson, F., Shaw, H., 2003. New clinopyroxene-liquid thermobarometers for mafic, evolved, and volatile-bearing lava compositions, with applications to lavas from Tibet and the Snake River Plain, Idaho. American Minerologist 88, 1542–1554.

Ranero, C.R., Torné, M., Banda, E., 1995. Gravity and multichannel seismic reflection constraints on the lithospheric structure of the Canary Swell. Mar Geophys Res (Dordr) 17, 519–534.

Romero Ruiz, M. del C., 1990. Las manifestaciones volcánicas históricas del Archipiélago Canario.

Scarrow, J.H., Pankhurst, M.J., Barbee, O.A., Chamberlain, K.J., Morgan, D.J., Longpré, M.A., Tramontano, S., Hickey, J., Neave, D.A., Rollinson, G.K., Stewart, A.G., Wieser, P.E., Coldwell, B.C., Hernández, W., D'Auria, L., Pérez, N.M., 2024. Decoding links between magmatic processes and eruption dynamics: whole-rock time series petrology of the 2021 Tajogaite eruption, La Palma. Volcanica 7, 953–980. https://doi.org/10.30909/vol.07.02.953980

Schnetzler, C.C., Philpotts, J.A., 1970. Partition coefficients of rare-earth elements between igneous matrix material and rock-forming mineral phenocrysts—II. Geochim Cosmochim Acta 34, 331–340.

Tenzer, R., Bagherbandi, M., Vajda, P., 2013. Global model of the upper mantle lateral density structure based on combining seismic and isostatic models. Geosciences Journal 17, 65–73. https://doi.org/10.1007/s12303-013-0009-z

Torres-González, P.A., Luengo-Oroz, N., Lamolda, H., D'Alessandro, W., Albert, H., Iribarren, I., Moure-García, D., Soler, V., 2020. Unrest signals after 46 years of quiescence at Cumbre Vieja, La Palma, Canary Islands. Journal of Volcanology and Geothermal Research 392, 106757. https://doi.org/10.1016/J.JVOLGEORES.2019.106757

Turner, S., Hoernle, K., Hauff, F., Johansen, T.S., Klügel, A., Kokfelt, T., Lundstrom, C., 2015. 238 U–230 Th–226 Ra disequilibria constraints on the magmatic evolution of the Cumbre Vieja volcanics on La Palma, Canary Islands. Journal of Petrology 56, 1999–2024.

Ubide, T., Márquez, Á., Ancochea, E., Huertas, M.J., Herrera, R., Jesús Coello-Bravo, J., Sanz-Mangas, D., Mulder, J., Macdonald, A., Galindo, I., 2023. Discrete magma injections drive the 2021 La Palma eruption. Sci Adv.

Villemant, B., Jaffrezic, H., Joron, J.-L., Treuil, M., 1981. Distribution coefficients of major and trace elements; fractional crystallization in the alkali basalt series of Chaine des Puys (Massif Central, France). Geochim Cosmochim Acta 45, 1997–2016.

Weis, F.A., Skogby, H., Troll, V.R., Deegan, F.M., Dahren, B., 2015. Magmatic water contents determined through clinopyroxene: Examples from the Western Canary Islands, Spain. Geochemistry, Geophysics, Geosystems 16, 2127–2146. https://doi.org/10.1002/2015GC005800

Wieser, P.E., Petrelli, M., Lubbers, J., Wieser, E., Özaydın, S., Kent, A.J.R., Till, C.B., 2022. Thermobar: An open-source Python3 tool for thermobarometry and hygrometry. Volcanica 5, 349–384. https://doi.org/10.30909/vol.05.02.349384

Wilson, J.T., 1973. Mantle plumes and plate motions. Tectonophysics 19, 149–164.